As-grown carbon nanotube quantum dots with superconducting contacts

Inauguraldissertation

zur
Erlangung der Würde eines Doktors der Philosophie
vorgelegt der
Philosophisch-Naturwissenschaftlichen Fakultät
der Universität Basel

von

Stefan Nau
aus Friedrichshafen (Deutschland)

Basel, 2014

Genehmigt von der Philosophisch-Naturwissenschaftlichen Fakultät
auf Antrag von
Prof. Dr. Christian Schönenberger
Prof. Dr. Gary Steele

Basel, den 25. März 2014

Prof. Dr. Jörg Schibler
Dekan

Contents

1 Introduction

The progress in fabrication technology and the miniaturization of nanostructured devices in the recent past has attracted a lot of interest in the field of electronic circuits on the nanoscale where the system's spatial dimensions allow for the investigation of quantum phenomena. Since their first identification by S. Iijima in 1991 [1], carbon nanotubes (CNTs) have been implemented in electronic junctions making use of their extraordinary electronic and mechanical properties: A CNT is a quasi one-dimensional object on a length scale where the combined observation of classical and quantum mechanical effects is possible. It can give rise to ballistic electron transport or to the formation of quantum dots where sequential transport of single electrons through the structure can be achieved. The investigation of CNT quantum dots has given insight into their intrinsic electronic properties, such as orbital degeneracy [2] or curvature-induced spin-orbit interaction [3]. Since certain intrinsic electronic features of CNTs are often masked by disorder that is introduced during the device preparation process, the need for very clean CNTs without any defects has lead to the fabrication of as-grown CNT devices, which are often also referred to as ultra-clean CNTs, by J. Cao *et al.* [4] in 2005.

Since their introduction, such as-grown CNT devices have been shown to be nearly defect-free and have lead to a considerable number of interesting results during the last years [5–9]. In addition, they can yield very high mechanical resonance frequencies in combination with large quality factors up to $Q = 100,000$ [10]. These properties make them useful for nanomechanical applications in the quantum regime, since they provide the opportunity of

reaching the quantum ground state of a macroscopic vibrational mode at cryogenic temperatures already in the mK regime. In contrast to conventionally prepared CNT devices, the basis of the fabrication scheme is the synthesis of the CNT being the very last production step. This prevents residues of post-fabrication processes from sticking to the CNT. Furthermore, the electron radiation applied to the device for imaging and localization is avoided, which usually causes severe damage to the CNT even for electron beams in the low keV regime [11]. However, this process needs the electrodes to be pre-fabricated and additionally to have a deep trench in between them to ensure the CNT to be suspended after growth and thus preventing influences of the substrate. This limits the choice of contact materials, mainly by the CNT growth process at high temperatures which will simply melt many of the contact materials established so far, such as aluminum, for example. Therefore, platinum is the main candidate for normal metal contacts at the moment.

Going a step further by using superconductors as contacts to such clean, as-grown devices is a promising goal, since the combination of CNT quantum dots with superconducting electrodes has already been shown to be a nice tool for several applications and has lead to the observation of various effects, such as gate-tunable supercurrents [12], has shown interesting results in Andreev transport [9, 13–15], and has also exhibited the possibility to do enhanced bias spectroscopy [16]. A further example is a Y-junction, consisting of a superconducting and two normal electrodes, that provides the basis of a Cooper pair splitter, a realization of a solid state source of entangled electron-pairs [17]. This has first been realized in an InAs nanowire [18] and a conventional CNT device [19]. Generally, these so-called hybrid devices that consist of several types of contact materials, such as superconductors, normal metals or even ferromagnets, are promising candidates for a large variety of experiments [20].

Theoretical work suggests further promising combined applications of clean CNTs and superconducting contacts. For example, a device that consists of a CNT in direct contact to a superconducting substrate over its whole length is supposed to allow for the formation and experimental observation of Majorana fermions [21]. Furthermore, a suspended nanostructure can be cooled by an AC Josephson current flow [22]. It is also suggested that the direction of a Josephson current can be reversed in a CNT with strong spin-orbit interaction [23], a phenomenon that is referred to as $0 - \pi$ transition and that has already been experimentally investigated on a CNT quantum dot with superconducting contacts [24–26]. In addition, already lots of experimental work has been done on the mechanical properties and vibrational effects in suspended CNTs where the interplay of electronic transport with different mechanical vibrational modes has been investigated. It is possible, for example, to extract

the resonance frequency of a CNT that is externally driven into transverse vibration, by measuring the resonant response of the electrical current through the device [8, 10, 27]. Furthermore, tunneling electrons can not only be used for the detection of vibrations, but they can also excite the longitudinal stretching mode in a suspended CNT [5, 28]. This coupling of longitudinal vibrations and tunneling electrons can then lead to a suppression of current through the CNT, an effect known as the Franck-Condon blockade [29].

Altogether, these are promising starting points for both, the fabrication of as-grown CNTs with superconducting contacts and the prospect of new effects and observations. Several interesting effects like spin-orbit interaction and vibrational excitations have already been investigated on such devices, but those experiments have been done on normal metal contacts. Theoretical suggestions of further effects on such devices like $0-\pi$ transitions, make the preparation of clean, as-grown CNTs with superconducting contacts a promising goal. This project is about the road from the fabrication of such devices to their characterization by electronic transport measurements at both, room temperature and cryogenic temperatures. In the end, despite functional superconducting contacts, clear signs of the superconducting proximity effect in as-grown CNT devices could not be observed. However, the fabrication scheme itself was established and resulted in clean devices that lead to some other interesting results in the field of inelastic cotunneling and electron-phonon coupling. This thesis is organized as follows:

Chapter 2 contains the theoretical background on the later investigated effects such as the electronic transport through CNTs quantum dots, combined with the influence of superconducting contacts and mechanical vibrations. The sample fabrication process is described in **Chapter 3** including metal sputter deposition, CNT growth, and an introduction to the measurement setup. Different properties and low temperature measurements of various superconducting contact materials and their suitability for the as-grown fabrication scheme are depicted in **Chapter 4**. In **Chapter 5**, measurements on a conventionally prepared CNT quantum dot with rhenium contacts are presented that show signatures of the superconducting proximity effect and indicate the suitability of rhenium as contact material. The subsequent experimental data is obtained on as-grown CNT devices that at first yield gate-dependent inelastic cotunneling thresholds within the Coulomb blockaded regime, as they are presented in **Chapter 6**. In the following, a quantum dot on a partly suspended CNT is investigated in **Chapter 7**. Parallel lines inside the Coulomb blockaded region of the charge stability diagram are observed that are antisymmetric with respect to zero bias. This is interpreted as a result of the formation of a parallel double quantum dot in a bundle of CNTs. Additional excited state lines

suggest the excitation of longitudinal vibrations by tunneling electrons in the second, weakly coupled quantum dot. Some preliminary results on a device prepared after a different fabrication scheme with recessed bottom-gates and conventional contacts are introduced in the last **Chapter 8** before the final summary and conclusion in **Chapter 9**.

2
Theoretical basics

Since their discovery in 1991 by S. Iijima [1], carbon nanotubes have created a huge field of research due to their extraordinary electronic and mechanical properties. This chapter provides the theoretical background to the subsequent discussion on this thesis' experiments about electronic transport through CNT quantum dots (QDs) in combination with vibrational excitations and with superconducting contacts. The electronic properties of CNTs are determined by their diameter and their chirality; they can be either metallic, semiconducting with different values for the band-gap, or metallic ones can also have a small band-gap, induced by the curvature of the CNT. The origin of these characteristics can be derived from the electronic band-structure of graphene which is presented in the first part of this chapter. Furthermore, some phenomena of single electron transport are introduced in a simple picture: If a short part of a CNT is contacted by two metallic leads, this confinement leads to the formation of a QD that can be loaded with single charge carriers that repulse each other due to the Coulomb interaction and are influenced by many different parameters. This results in various effects that are described in the second part. Other effects that are observed in the experiments in the framework of this thesis, such as negative differential conductance or the appearance of an equidistant set of excitation lines, are introduced theoretically. In addition, the explanation of the phonon blockade is given, which originates from the interplay between electronic and vibrational transitions in a vibrating CNT QD.

2.1. Electronic properties of carbon nanotubes

A carbon nanotube can be visualized as a sheet of graphene, a single atomic layer of graphite, rolled into a cylinder with a diameter of $1 - 2$ nm. This tininess makes CNTs useful for experiments in the quantum regime, yet they are able to carry very high current densities. In this section, the electronic properties of CNTs and the formation of quantum dots are introduced.

2.1.1. Electronic band-structure of graphene

To understand the electronic properties of a CNT, it is helpful to begin with the derivation of the band-structure of graphene by means of the tight-binding method. In a second step, the chiral structure of a specific CNT is taken into account by the zone-folding approximation. Graphene consists of a two-dimensional honeycomb lattice where the unit cell contains two carbon atoms. It can be characterized by the two primitive lattice vectors $\vec{a}_1$ and $\vec{a}_2$, as it is depicted in Fig. 2.1 (a). Since a single carbon atom has four valence electrons of which three are forming strong covalent sp^2 bonds in the graphene plane to the adjacent atoms, the fourth electron is in a p_z orbital perpendicular to the graphene plane. These orbitals can overlap among each other, resulting in delocalized electron states and therefore determining the conductivity of graphene. Applying the tight-binding model [30], that takes into account only hopping between the nearest neighbors, yields the energy-momentum relation

$$E(\vec{k}) = \pm\gamma\sqrt{3 + 2\cos(\vec{k}\cdot\vec{a}_1) + 2\cos(\vec{k}\cdot\vec{a}_2) + 2\cos(\vec{k}\cdot(\vec{a}_1 - \vec{a}_2))} \tag{2.1}$$

with the overlap integral γ. The resulting band-structure is depicted in Fig. 2.1 (b). It consists of two sub-bands π and π^* that join as cones at the so-called charge neutrality points, or Dirac points, located at the vertices of the hexagonal Brillouin zone. Of those six points only two are independent and are referred to as valleys K and K'. Close to the Dirac points, where the Fermi energy in the undoped state is located ($E_\mathrm{F} = 0$), the band-structure has a linear dispersion (see Fig. 2.1 (c)), that means all charge carriers in graphene move at the same velocity. This is in contrast to parabolic energy-momentum relations of conventional electron systems and can be expressed as

$$E(\vec{\kappa}) = \pm\hbar v_\mathrm{F}\,|\vec{\kappa}| \tag{2.2}$$

for $\vec{\kappa} = \vec{k} - \vec{K}$, with Planck's constant $\hbar$ and the Fermi velocity v_F [31]. The latter is given by $v_\mathrm{F} = 3/2a_0\gamma/\hbar \approx 8 \cdot 10^5$ m/s for $\gamma = 2.9$ eV [30] and the inter-atomic distance $a_0 = 1.42$ Å of the graphene lattice.

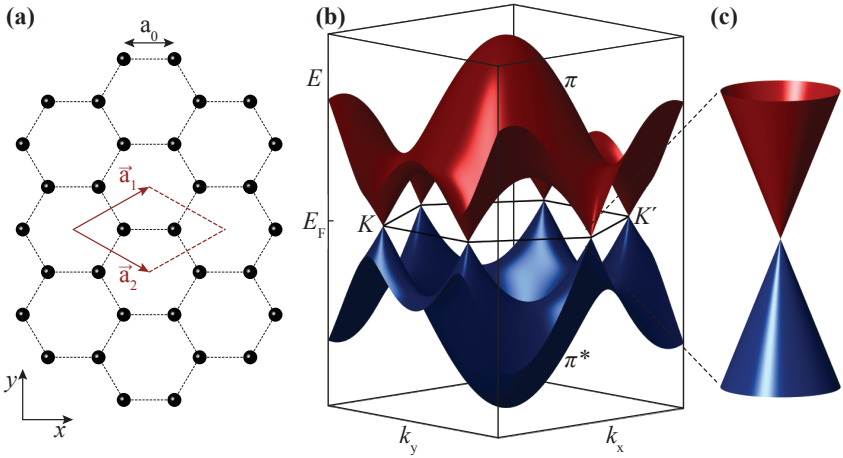

Figure 2.1.: Lattice- and band-structure of graphene. **(a)** Structure of a graphene layer with an inter-atomic distance of $a_0 = 1.42$ Å. The unit cell of the hexagonal lattice contains two atoms and is spanned by the primitive vectors $\vec{a}_1$ and $\vec{a}_2$. **(b)** The band-structure consists of two bands, π and π^*, joining at the K points of the hexagonal first Brillouin zone. **(c)** Close to the K points, the band-structure has a Dirac-like linear dispersion.

2.1.2. Electronic band-structure of a carbon nanotube

A specific CNT can be described by its circumferential, or chiral vector $\vec{C} = n\vec{a}_1 + m\vec{a}_2$ with $n, m \in \mathbb{N}$, that defines both, its symmetry and diameter. This is depicted in Fig. 2.2 (a), where a CNT is obtained by cutting a graphene sheet and rolling the extracted piece along $\vec{C}$ into a cylinder. The pair of numbers n and m are the chiral indices (n, m), which are characteristic for each CNT and determine its electrical properties. Figure 2.2 (b) shows examples of how to create the general CNT types armchair (n, n) and zig-zag $(n, 0)$. All other CNTs with arbitrary chiral indices are referred to as chiral. The electronic structure of a CNT is obtained by the zone-folding approximation that introduces periodic boundary conditions in its circumferential direction. This is valid, since CNTs are seamless objects, and results in a quantization of the wave vector component $\kappa_\perp$ perpendicular to the axial direction, while the axial component $\kappa_\parallel$ is effectively continuous, as here the electrons are free to move over much larger distances. The quantization of $\vec{k}$ along $\vec{C}$ results in a set of allowed values for $\kappa_\perp$ that are obtained by

$$\vec{C} \cdot \vec{\kappa} = \pi d \kappa_\perp = 2\pi \left(\frac{m-n}{3} + p \right) \tag{2.3}$$

with $p \in \mathbb{Z}$ [31]. This leads to one-dimensional sub-bands, or a continuum of $\kappa_{\parallel}$ states in each $\kappa_{\perp}$ mode, that are slicing the two-dimensional graphene band-structure, as it is illustrated in Fig. 2.3 (a) by blue lines. The number of the respective sub-band is denoted as p in Eq. (2.3).

The main contribution to charge transport are states in sub-bands with $E(\kappa)$ close to E_{F}, which here is equivalent to being close to K and K'. The exact alignment between the allowed κ states and the K points is defined by the chiral indices via Eq. (2.3). The chiral indices also determine the number, the spacing, and the length of the sub-bands [33, 34]. Hence, it becomes clear that the kind of wrapping of a CNT determines its electrical properties: If $\vec{C}$ changes with chiral indices that allow for a sub-band to cross the graphene cones at a K point, there is a finite density of states available for all energies

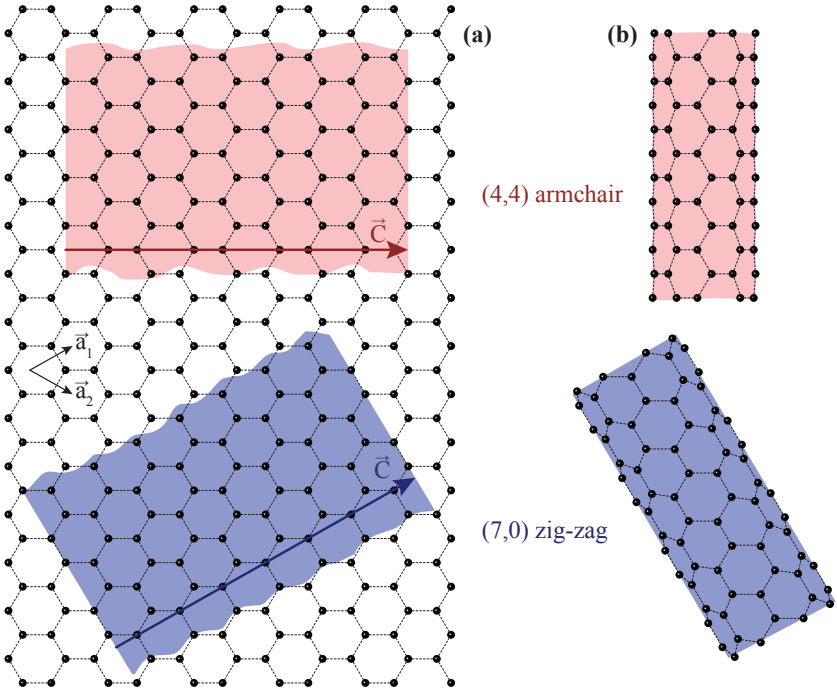

Figure 2.2.: (a) Cutting a strip in a graphene sheet and rolling it to a cylinder produces a CNT. The direction of the roll-up defines the circumferential, or chiral vector $\vec{C}$. **(b)** Creation of a $(4, 4)$ armchair and an $(7, 0)$ zig-zag CNT with chiral indices (n, m).

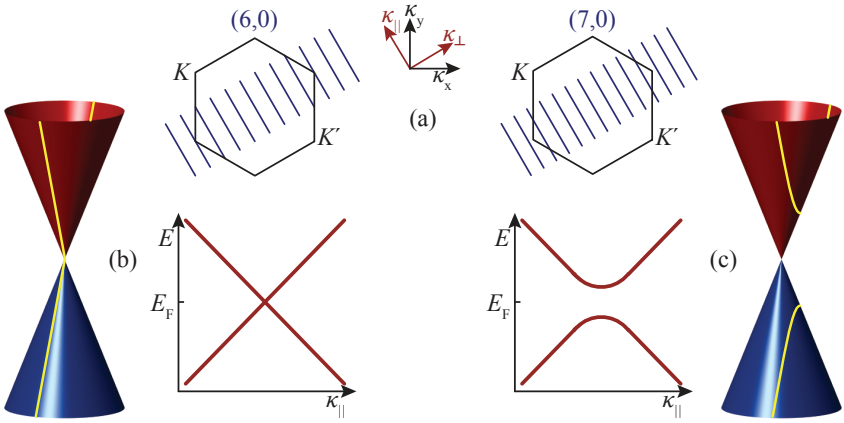

Figure 2.3.: (a) The one-dimensional sub-bands arise from the circumferential boundary conditions in a CNT that are folded with the first Brillouin zone of graphene, the so-called zone-folding approximation. Examples for a metallic and a semiconducting zig-zag CNT with chiral indices $(6,0)$ and $(7,0)$ are shown, respectively [32]. Joining with a K point results in a finite density of states at the Fermi energy and consequently in a metallic CNT **(b)**, or otherwise a finite band-gap that attests for a semiconducting CNT **(c)**.

which accounts for a metallic CNT (see Fig. 2.3 (b)). In contrary, forbidden κ states at the K points result in a finite band-gap, thus a semiconducting CNT (see Fig. 2.3 (c)), with their separation in energy determining the size of the semiconducting band-gap. Calculating the energy dispersion via Eq. (2.2) including Eq. (2.3) results in:

$$E(\kappa_\parallel) = \pm\frac{2\hbar v_\mathrm{F}}{d}\sqrt{\left(\frac{m-n}{3}+p\right)^2+\left(\frac{\kappa_\parallel d}{2}\right)^2} \tag{2.4}$$

with the CNT diameter d [31]. If $E(\kappa_\parallel = 0) = 0$ holds for a certain sub-band p, the CNT is metallic due to the non-presence of a band-gap. It turns out that this is the case for $(m-n)/3 = -p$ which leads to the following rule: for $m-n$ being a multiple of 3, the CNT is metallic otherwise it is semiconducting. Thus, armchair CNTs are always metallic. Furthermore, the different possibilities of electronic structures for CNTs with different chiral indices result in a total probability of one-third of CNTs being metallic and two-thirds being semiconducting [35]. However, since the zone-folding approximation ignores influences stemming from the bending of the graphene layer and the resulting variations in the overlap of the p_z orbitals, it is possible that a finite small

band-gap is induced in actual metallic CNTs by twist or strain [36, 37]. This should happen only for chiral and zig-zag metallic CNTs but not for armchair CNTs due to symmetry reasons [38]. They are referred to as quasi-metallic or small band-gap CNTs.

2.2. Single-electron transport in carbon nanotube quantum dots

Rolling graphene into a CNT produces a one-dimensional conductor whose electrical properties depend on its structure which is described by the chiral vector. The addition of further constraints also in the axial direction leads to a confinement of the longitudinal electron waves as well. Hence, the CNT can now be referred to as a zero-dimensional electronic island, where the quantization of the electron waves results in the formation of a quantum dot (QD) with discrete energy levels.

2.2.1. Quantum dots

Assuming the confinement along the CNT axis acting as a one-dimensional box for the electrons and making use of the band-structure linearity near the Fermi energy (see Eq. (2.2)), the energy level spacing is $\delta E = hv_\mathrm{F}/L$ [2] and yields

$$\delta E \approx \frac{3.31}{L[\mu\mathrm{m}]}\ \mathrm{meV} \tag{2.5}$$

for a metallic CNT of length L with the Fermi velocity $v_\mathrm{F} \approx 8 \cdot 10^5$ m/s. This level spacing can be observed experimentally only if it is larger than the thermal energy, i.e. $\delta E \gg E_\mathrm{th} = k_\mathrm{B}T$. Consequently, according to Eq. (2.5), a QD in a CNT of reasonable length in the sub-µm regime can already be investigated in, e.g. liquid helium at ambient pressure, for which $E_\mathrm{th}(T = 4.15\ \mathrm{K}) \approx 0.36$ meV. A typical device structure is depicted in Fig. 2.4 (a), where the QD forms on the CNT between source (S) and drain (D) contacts which are electrically isolated from the highly doped Si^{++} substrate by a thin SiO_2 layer. The substrate can be used as back-gate in order to electrostatically shift the QD levels in energy and thus change the number of electrons on the QD via S and D.

As it is depicted in Fig. 2.4 (b), the description of such a QD system can be done in a simple picture by a capacitive model, the so-called *constant interaction model* [39–41], under two assumptions: First, the Coulomb interaction between the electrons is not influenced by the number of electrons on the QD. Second, the interactions of the electrons on the QD with the environment, which here consists only of S and D contacts and the BG, are described by the system's

combined total capacitance $C_\Sigma = C_s + C_d + C_{bg}$. Furthermore, the QD couples to the BG only capacitively via C_{bg}, while its coupling to S and D via the tunnel barriers can be characterized by the tunnel coupling strengths $\Gamma_{s,d}$ and the capacitive couplings $C_{s,d}$, respectively. Hence, electrons can enter or leave the QD only via S or D. The charging energy U_C is defined as the energy required to add an electron to the dot in order to overcome the Coulomb repulsion of the other electrons already on the QD, and it is related to the total capacitance of the system via $U_C = e^2/2C_\Sigma$. As a consequence, the energy levels are not only separated by δE, but each level is split four-fold by the amount of U_C as well, according to the typical four-fold degeneracy of a CNT QD. This stems from two-fold spin degeneracy and the so-called valley degeneracy which has its origin in the possibility of electrons to move clockwise or counterclockwise at the same energy on the CNT circumference. As it is indicated in Fig. 2.3 (a), there are always two sub-bands that are closest to a charge neutrality point, i.e. symmetric at K and K', corresponding to $\kappa_\perp$ and -$\kappa_\perp$. This can be visualized

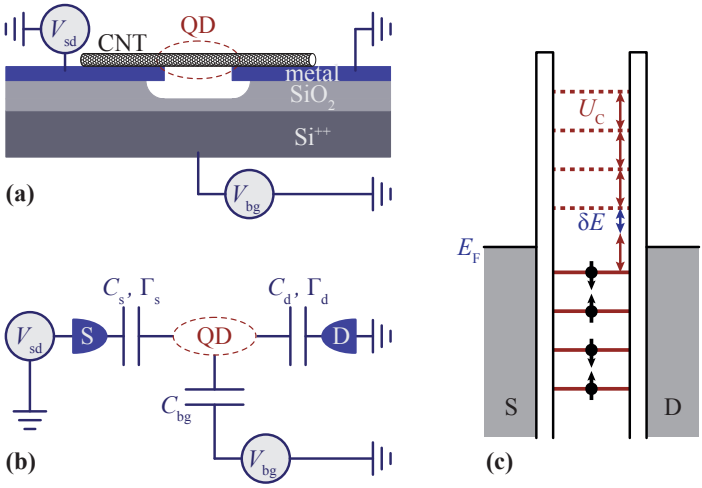

Figure 2.4.: Schematics of a CNT QD. **(a)** The CNT is contacted to source (S) and drain (D) electrodes. The back-gate voltage V_{bg} is applied to the highly doped Si^{++} substrate that is electrically isolated from the contacts by a thin SiO_2 layer. **(b)** A QD forms due to tunnel barriers at the CNT-metal interface. It is capacitively coupled to S, D, and the back-gate: C_s, C_d, C_{bg}. The coupling parameters Γ_s and Γ_d characterize the tunnel coupling to the electrodes. **(c)** Energy levels of a CNT QD. Its discrete energy states are filled up to the chemical potential of the leads and separated by the charging energy U_C for each electron and the level spacing δE for each electron shell that is four-fold degenerate.

as electrons in K and K' valleys circling the CNT with opposing handedness. Altogether, this results in an electronic shell with four electrons and thus, in order to add the first shell-electron, the required addition energy sums up to $E_{\mathrm{add}} = U_{\mathrm{C}} + \delta E$; but for the addition of the subsequent three electrons, only $E_{\mathrm{add}} = U_{\mathrm{C}}$ has to be provided. This principle is depicted in the sketch of discrete endergy levels of a QD in Fig. 2.4 (c).

Assuming metallic leads, the energy-dependent occupation of electron states is given by the Fermi-Dirac distribution

$$f_{\mathrm{FD}}(E,T) = \frac{1}{e^{\frac{E-\mu}{k_{\mathrm{B}}T}} + 1} \tag{2.6}$$

with the chemical potential μ of the leads. For low temperatures it can be approximated as a step-function at μ which can also be substituted by the Fermi energy E_{F}, since $\mu = E_{\mathrm{F}}$ for $T = 0$ (see Fig. 2.4 (c)). For $E < E_{\mathrm{F}}$, there is a continuum of occupied electronic levels while for $E > E_{\mathrm{F}}$, all of the available states are empty. This applies for the QD as well: the discrete energy states are occupied below E_{F} and empty above.

The addition of single electrons to the QD can be observed by measuring the electrical conductance through the dot which is very sensitive to the alignment

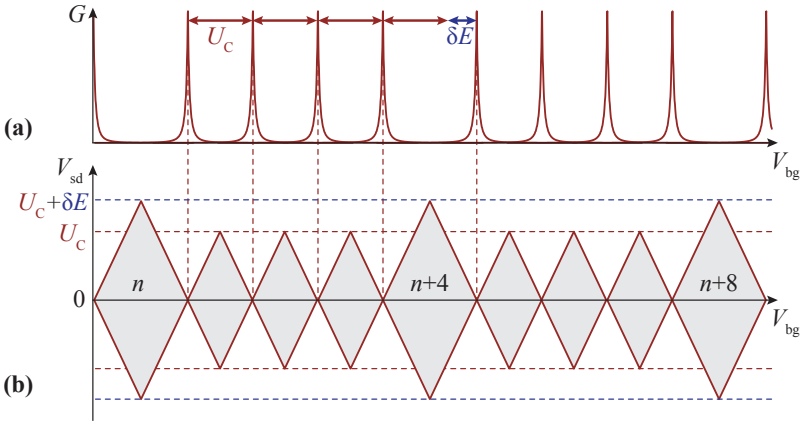

Figure 2.5.: (a) Coulomb blockade peaks in differential conductance G through a CNT QD. Shifting the energy levels by means of back-gate voltage V_{bg} results in a peak as soon as a level is aligned with E_{F} of the leads. Each electron shell contains four levels due to spin and valley degeneracies. **(b)** A Coulomb blockade diamond pattern is gained in a two-dimensional stability diagram by applying an additional bias-voltage V_{sd}. The number of electrons on the QD is given by the integer n.

of the QD's energy levels with respect to the Fermi energy in the leads. Only if E_F is in resonance with one dot level, electron transport through the QD becomes possible; otherwise it is blocked and the situation is referred to as Coulomb blockade. The level positions on the QD can be shifted in energy by means of a voltage applied to the back-gate, V_{bg}. Thus, a measurement of the differential conductance $G = dI/dU$ through the QD as a function of V_{bg} yields a set of so-called Coulomb peaks, as it is sketched in Fig. 2.5 (a). Their inter-peak distance corresponds to the respective value of E_{add} and displays the four-fold degeneracy of the QD levels. By applying an additional bias voltage V_{sd} to S and D, a two-dimensional pattern, the so-called stability diagram, is observed, as it is sketched in Fig. 2.5 (b), where the line along $V_{sd} = 0$ corresponds to the graph in Fig. 2.5 (a) and exhibits conductance peaks at the so-called charge degeneracy points. Thus, the lines are ridges of high conductance, whereas the grey-shaded regions are called Coulomb blockade diamonds. The shape of the diamonds can be explained in a simple picture: starting at a charge degeneracy point, both, V_{sd} and V_{bg} have to be increased/decreased simultaneously in order to sustain the alignment of the QD level to the chemical potential of the lead keeping electron transport through the dot available. This corresponds to the linear edge of a Coulomb diamond with positive/negative slope. The picture can be applied to all boarder lines of the diamonds. An example of an actual measurement on an as-grown suspended CNT device is shown in Fig. 2.6. Here, only a two-fold degeneracy is observed; most likely because the orbital degeneracy is lifted due to disorder in the CNT. By determining $\delta E \approx 7$ meV as depicted in Fig. 2.5 (b) and applying Eq. 2.5, the QD length

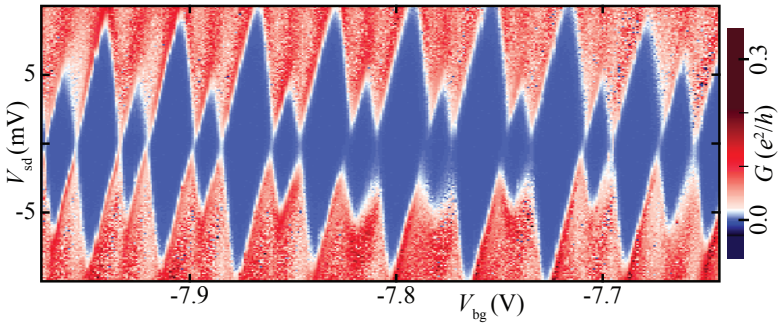

Figure 2.6.: Stability diagram measurement of a Coulomb blockade pattern on the suspended, as-grown CNT Device D1 of which an electron micrograph is shown in Fig. 3.2 (e). The clear two-fold symmetry is due to spin degeneracy while the orbital degeneracy is lifted. A possible reason would be a disordered CNT.

can be estimated to $L \approx 0.5$ µm. This is in good agreement with the length of the suspended part of the CNT between the electrodes, as it is shown in the electron micrograph of Fig. 3.2 (e). Furthermore, the Coulomb blockade pattern of this measurement appears quite regular and stable.

However, it is not as highly symmetric as the one sketched in Fig. 2.5 (b). This is because of the typical asymmetric biasing in experiments, i.e. V_{sd} is applied to S while D is set to ground, which results in a finite tilt of the diamonds, or different slopes of the positive $s_{(+)}$ and negative $s_{(-)}$ diamond edges, respectively, as it is depicted in Fig. 2.7. Since the slopes are related directly to the capacitive couplings of a QD to S, D, and BG, it is possible to determine the latter from experiment by measuring $s_{(+)}$ and $s_{(-)}$ and applying the equations given in Fig. 2.7. In order to do so, the system's lever arm has

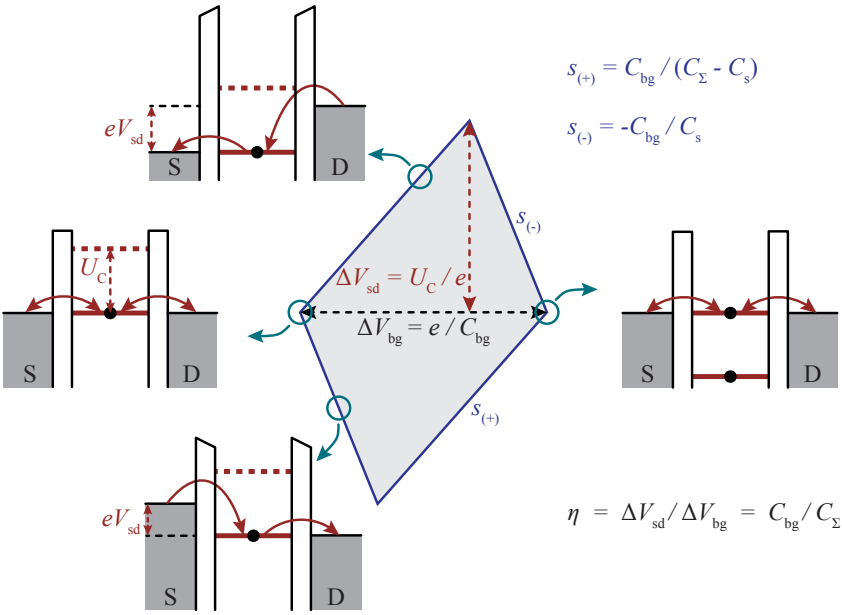

Figure 2.7.: The different situations for the energy levels at four different point of a Coulomb diamond. V_{bg} needs to be changed in order to keep the level aligned for finite V_{sd}. The various capacitances of a QD determine its coupling to the environment and thereby the two slopes of the diamond edges. Especially for asymmetric biasing, with drain contact on ground, the resulting diamond is typically tilted and not mirror-symmetric. The lever arm η determines the efficiency of the back-gate coupling with respect to bias-coupling (adapted from Ref. [41, 42]).

to be calculated via $\eta = \Delta V_{\mathrm{sd}}/\Delta V_{\mathrm{bg}} = C_{\mathrm{bg}}/C_{\Sigma}$. It accounts for the different capacitive couplings of the BG and the leads, where the former is typically much weaker due to the insulating SiO_2 layer between BG and CNT. Thus, η is a measure for the back-gate efficiency, i.e. which value for V_{bg} corresponds to V_{sd} in order to achieve the same energy shift in the system. Hence, η can be read directly from the dimensions of a Coulomb diamond. The stability diagram leads to further information on the QD system's properties: For example, U_{C} and δE are directly given by the vertical size of the diamonds and the additional size for every forth diamond, respectively. Furthermore, the tunnel coupling $\Gamma = \Gamma_{\mathrm{s}} + \Gamma_{\mathrm{d}}$ determines the full width at half maximum (FWHM) of the Coulomb peaks, as long as $\Gamma \gg k_{\mathrm{B}}T$ (see Fig 2.5 (a)).

The confinement of the electronic wave function is realized by two metallic contacts which leads to the formation of tunnel barriers at the interface to the CNT. The height of these barriers is determined by various parameters, such as the cleanliness of the interface in combination with the total contact area, the kind of contact material, especially due to its characteristic work function Φ_{m}, and the CNT itself, since for semiconducting ones, there can be an additional Schottky barrier [43]. Chapter 2.5 will focus on such influences on the contact at the CNT-metal interface.

So far, only first-order resonant tunneling processes have been considered, i.e. tunneling events that imply sequential transport of single electrons through the QD. There are also second-order processes, where the simultaneous tunneling of two electrons is involved. Those can allow for additional transport signatures, such as the so-called cotunneling thresholds, within the Coulomb blockaded regions and will be focused on in the following together with excited state lines that occur if more than one energy level is positioned within the bias window.

2.2.2. Sequential tunneling and cotunneling processes

As shown before, the Coulomb blockade of a CNT QD can be overcome by either applying V_{sd}, or by shifting the QD levels via V_{bg} in order to align one of them with the chemical potential of the leads. A further increase of the bias up to the level of an excited state of the QD leads to an additional conductance channel becoming available for transport. This is typically accompanied by a step-like increase of current for every excited state added to the bias window. Thus, the corresponding stability diagram shows ridges of high conductance running parallel to the edges of the Coulomb diamonds. The vertical separation in V_{sd} is determined by the level spacing of the QD states. This principle is shown in the schematic energy diagram and the corresponding stability diagram of Fig. 2.8, where the excited state lines occur outside the Coulomb blockaded regions. Furthermore, it is also possible to observe features of other

tunneling effects within the actual blockaded diamonds. These are second-order tunneling events that are commonly known as cotunneling events since they involve the simultaneous tunneling of two or more electrons [44]. They have been observed in both, CNT [44–46] and two-dimensional electron gas QDs [47] and are basically introduced in Fig. 2.9. Given very transparent contacts to a QD, electrons are more likely to leave the QD to one lead and being replaced by one from the other lead instantaneously.
Note the different kind of picture applied for the energy diagrams in Fig. 2.8 (a) and Fig. 2.9 (a) compared to that of Fig. 2.4 (c): The former depicts all four electrons of one shell split by the charging energy U_C, while in the latter, each shell is represented by a four-fold degenerate single level that is separated by the level splitting δE from its neighboring shells, i.e. this picture does not consider the Coulomb repulsion, since it does only play a minor role for elastic and inelastic cotunneling effects. A fact that makes cotunneling spectroscopy a nice tool to probe the level spacing of a QD. Furthermore it is possible to investigate, e.g. the magnetic field dependence of the four-fold degenerate excited state of a single electron on a CNT QD; from its different splitting the spin-orbit interaction in CNTs has been been observed [6].
In contrast to those of first-order, second-order tunneling events imply the simultaneous tunneling of two electrons via filled QD states that are positioned energetically below the chemical potential of both leads. This is only possible

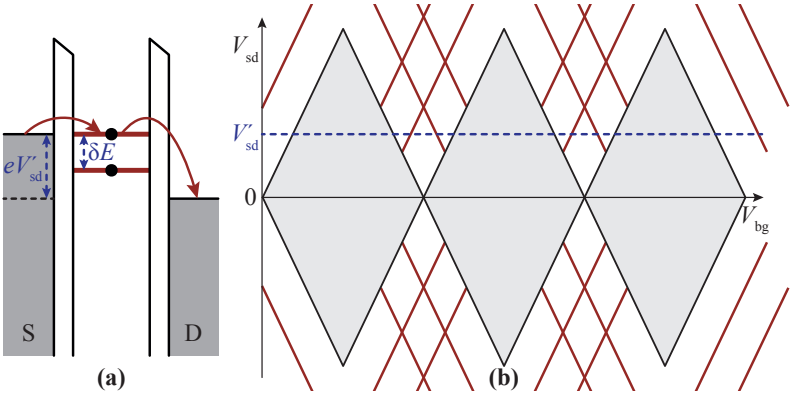

Figure 2.8.: (a) Schematic energy diagram of a QD coupled to S and D at finite V_{sd}. If an excited QD level enters the bias window, an additional channel becomes available for transport. **(b)** This yields a ridge of high conductance running parallel to the Coulomb diamond edges in the stability diagram. This model does not consider the charging energy U_C, thus each level represents a four-fold degenerate electron shell. They are separated by the level spacing δE with $\delta E < U_C$ for this specific example.

for appropriate tunneling rates, i.e. very good coupling to the leads. Elastic cotunneling events result in a finite current through the QD that depends linearly on an applied bias voltage and therefore yields a constant value of differential conductance G for all V_{bg} and for $eV_{\mathrm{sd}} < \delta E$; even within the actual blockaded regions. If eV_{sd} matches the level spacing, an additional channel becomes available due to inelastic cotunneling, i.e. a cotunneling event that leaves the QD in an excited state. This occurs if an electron leaves the QD from its ground state to D while a second electron enters the QD from S into an excited state, as shown in Fig. 2.9 (b). The inelastic cotunneling threshold yields a step in G for $eV_{\mathrm{sd}} \geq \delta E$, represented by the dark grey areas in Fig. 2.9 (c). At the boundary of the Coulomb diamonds, the inside cotunneling thresholds join the outside excited state lines.

Figure 2.10 shows the measured stability diagram of a CNT QD with rhenium/tungsten contacts. Since the cotunneling features are quite weak, G is plotted in a logarithmic scale. The previously introduced inelastic cotunneling thresholds are clearly visible and joining the excited state lines at the boundary of the diamonds. The asymmetric appearance of the excited state lines only at one edge of the diamonds is attributed to different tunnel couplings Γ_{s} and Γ_{d}, respectively. The measurements are done at a temperature of $T = 23$ mK with the standard electrical setup in the dilution refrigerator that will both be described in Ch. 3.5.

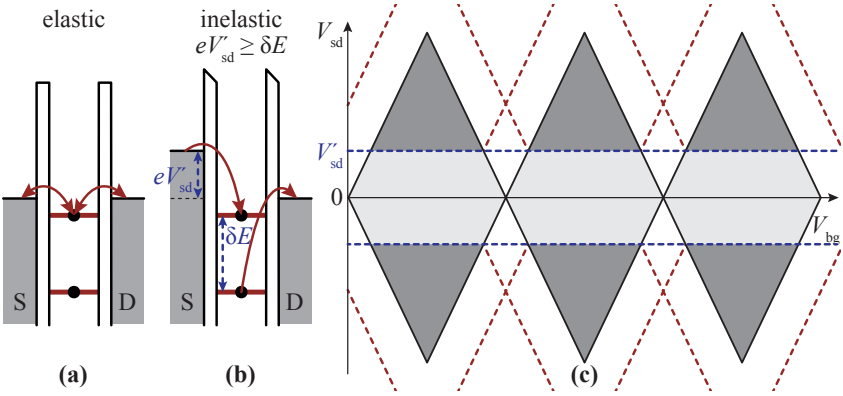

Figure 2.9.: (a) Schematic energy diagram of a QD well-coupled to S and D with $\delta E < U_{\mathrm{C}}$. Due to elastic cotunneling events there is a finite differential conductance within the blockaded region (light grey areas within the Coulomb diamond. **(b)** For $eV_{\mathrm{sd}} \geq \delta E$ the cotunneling current is increased by inelastic processes via virtual states (dark grey areas in **(c)**). **(c)**) In the corresponding stability diagram, the horizontal cotunneling lines do basically not depend on back-gate voltage but only on δE.

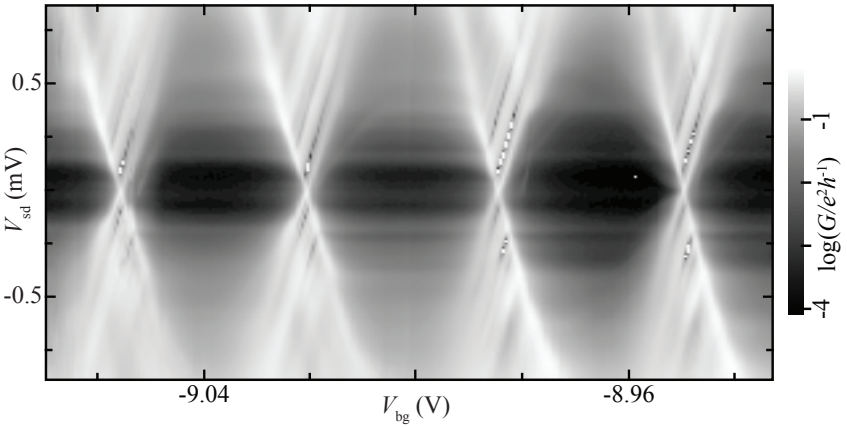

Figure 2.10.: Measured stability diagram on the CNT QD Device C1 with rhenium/tungsten contacts at $T = 23$ mK. It yields both, inelastic cotunneling thresholds within the Coulomb blockade diamonds and excited state lines running outside and parallel to their edges. Since the cotunneling signal is much weaker, the color code is given in a logarithmic scale in order to make both effect visible in the same plot.

2.2.3. Gate-dependent cotunneling thresholds

Inelastic cotunneling thresholds (ICTs) are supposed to occur as horizontal features in the stability diagram, because they reflect the level spacing, which is usually independent of the actual level position on a small gate voltage range. Thus, they should not dependent on the gate voltage, which is proportional to the level position. This is the case for the measurement of Fig. 2.10. However, applying an external magnetic field to this device results in a finite tilt of the ICTs which is symmetric with respect to $V_{\mathrm{sd}} = 0$, as can be seen in Fig. 2.11. Similar results have already been reported on CNT QDs [16, 45, 46] where this feature is explained by the large coupling strength of the QD to the leads. This can give rise to level renormalization effects that are induced by the enhanced tunneling between one of the QD orbitals and the leads and finally result in a finite gate dependence of the ICTs within the first two Coulomb diamonds of a four-electron shell on the QD.

The basic principle of this effect is explained in Fig. 2.12 by the example of a four-electron shell that is occupied by a single electron and consists of two doublets that are split in energy and, importantly, have different coupling strengths to the leads. This is indicated by the width and color of the levels: broad and red stands for strong, whereas narrow and blue represents weak coupling, respectively. A stronger coupling leads to a higher rate of cotunneling events, i.e. charge fluctuations. This results in a renormalization of the level energy or

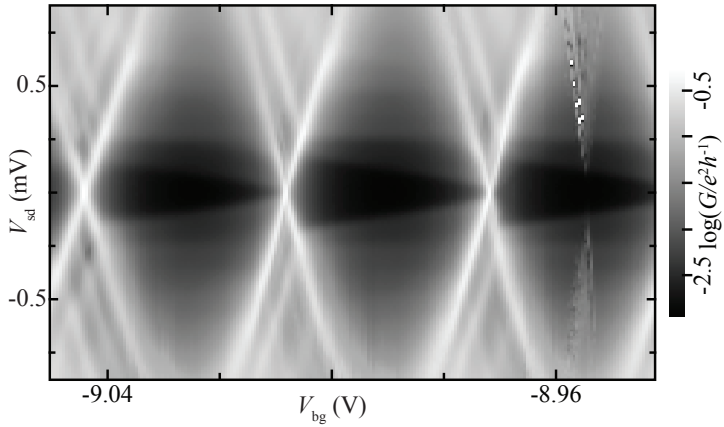

Figure 2.11.: Stability diagram measurement on the same Device C1 as in Fig. 2.10. Here, applying a finite external magnetic field of $B = 3$ T parallel to the CNT axis results in back-gate-dependent cotunneling thresholds at $T = 23$ mK

a tunneling-induced level shift towards lower energies that can be determined within second-order many-body perturbation theory [45] and yields three important effects: First, the shift in energy is determined by the coupling strength to the leads; hence, if the two doublets have different coupling strengths, their resulting level corrections will differ, which leads to a change of their energy spacing (see Fig. 2.12 (a),(c)). Second, closer to the charge degeneracy points of the two neighboring charge states, the charge fluctuations are more pronounced. And third, the fact that the charge fluctuations occur via the zero ⓪/two ② electron charge state on the left/right side of the Coulomb diamond, results in an increase/decrease of the level spacing at the respective side within the one electron charge state ①. This is equivalent to a tilted ICT as it is shown in Fig. 2.12 (b).

The fundamental principle of the different modification of the level spacing is explained in the lower parts of Fig. 2.12: In the left side of the Coulomb diamond, charge fluctuations between ① and ⓪ are dominant via the strongly coupled doublet (see Fig. 2.12 (d),(e)). That means the electron may leave and enter the QD via a cotunneling process. Since these fluctuations lead to a lowering of the respective level in energy, the stronger coupled doublet will consequently experience a larger shift towards lower energy than the weakly coupled doublet, resulting in an increase of their spacing. On the other hand, on the right side of the diamond, the two electron charge state ② is involved in the fluctuations. In this situation, there is only one highly probable possibility for tunneling via the strongly coupled doublet (see Fig. 2.12 (f)), while there

are two possibilities for efficient tunneling via the weakly coupled doublet (see Fig. 2.12 (g)). As a consequence, the latter describes the dominant fluctuations process and the doublet splitting becomes smaller. A detailed description of this phenomenon has been presented in Refs. [45] & [46]. Furthermore, it has been shown, that the difference in the tunnel coupling strength of the two doublets can be modified by applying a magnetic field parallel to the axis of the CNT [46].

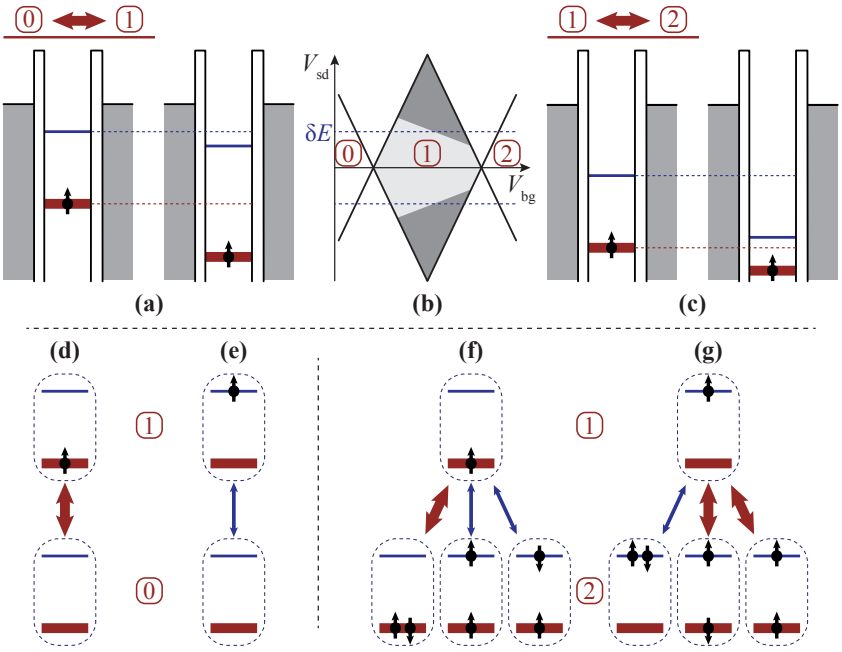

Figure 2.12.: Two doublets of an electron shell occupied with one electron have different coupling strengths to the leads, as indicated by broad/narrow levels for strong/weak coupling of the red/blue doublet, which changes their energy splitting. Charge fluctuations are most dominant close to the neighboring electron charge states. **(a)** In the left side of the Coulomb diamond, fluctuations from the one electron charge state ① via the zero electron charge state ⓪ give rise to an increase of the doublet splitting. **(b)** This results in a shift of the ICT in the left side of the diamond to larger bias voltages V_{sd}. **(c)** In the right side of the diamond, charge fluctuations from ① to the two electron charge state ② lead to a decreased doublet splitting and a shift of the ICT to smaller V_{sd}. The combination finally causes the tilted ICT in (b). **(d,e)** Charge fluctuations from ① to ⓪ are dominant via the strongly coupled doublet. **(f,g)** Charge fluctuations from ① to ② are dominant via the weakly coupled doublet. (adapted from Ref. [46]).

2.2.4. Parallel double quantum dots in carbon nanotubes

So far, the discussion was focused on the properties of the basic form of single-walled CNTs. However, they can also occur in the form of so-called multi-walled CNTs which can be visualized as multiple layers of graphene rolled to a cylinder, accordingly. Another possibility is that several single CNTs form a bundle, similar to the seams of a rope. By measuring their diameter it is possible to distinguish them, at least to some extent: Single-walled CNTs usually have diameters of less than 2 nm that can be determined, for example, by scanning tunneling microscopy or atomic force microscopy. In multiple CNT systems, it is possible that several QDs form a parallel configuration, where each of them is occupying one seam of a bundle or one shell of a multi-walled CNT, respectively. If one of those parallel QDs is in Coulomb blockade, it does not directly affect electron transport through the other dots which is in contrast to a serial configuration [7, 49–51], where one blockaded QD would block transport through the whole system. Furthermore, parallel QDs can interact with each other, which has been investigated by K. Goß *et al.* [48, 52–54] on a bundle of CNTs giving rise to the formation of four parallel QDs. Similar results have been observed in a so-called C_{60} peapod structure which consists of a single-walled CNT with a chain of encapsulated C_{60} molecules inside [54].

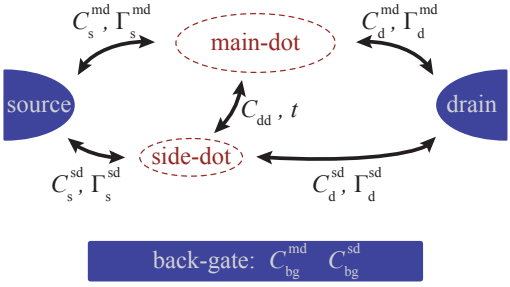

Figure 2.13.: Sketch of the transport model of two parallel quantum dots with different gate couplings and an inter-dot coupling by a hybridization with amplitude t. If the side-dot is positioned asymmetrically between the contacts, the respective coupling is also asymmetric (adapted from Ref. [48]).

To describe transport for such a special case of an interacting parallel double QD system, the model sketched in Fig. 2.13 is considered: Two QDs are contacted to source and drain and have different coupling strengths to the back-gate. This leads to a common Coulomb diamond pattern in the stability diagram for the stronger coupled dot, here referred to as the main-dot. Additionally, this pattern is superimposed with a second one, stemming from the

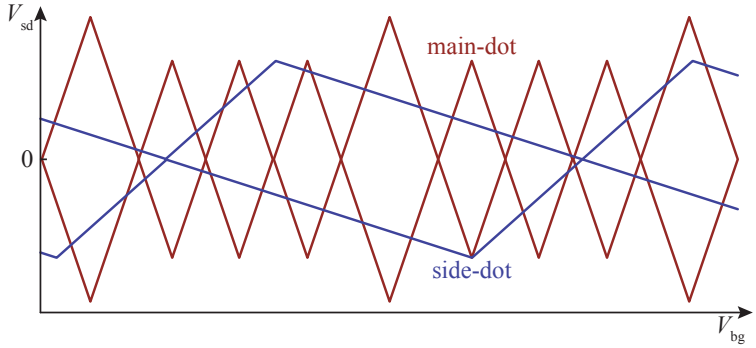

Figure 2.14.: Sketched stability diagram of parallel QDs with different gate couplings. It basically consists of two superimposed Coulomb diamond patterns where the stronger coupled one yields smaller diamonds and is referred to as the main-dot. An asymmetric coupling of the side-dot to source and drain results in strongly tilted diamonds.

so-called side-dot, which has diamond edges of much smaller slopes due to its weaker gate-coupling, as it is shown in Fig. 2.14. Furthermore, the side-dot can be very asymmetric if it is located much closer to one of the electrodes.

2.3. Carbon nanotube quantum dot with superconducting contacts

A superconductor generally exhibits two main characteristics for temperatures lower than its transition temperature, or critical temperature T_c: Its resistivity is unmeasurably small, i.e. the material is a perfect conductor, and additionally, it is a perfect diamagnet, which means that external magnetic fields H are expelled completely from its interior up to a critical field H_c. Furthermore, contacting a CNT QD to superconducting leads gives rise to many features due to the superconducting proximity effect, i.e. the penetration of superconducting charge carriers from the contacts onto the QD. For example, it is possible to measure a supercurrent through a CNT between two superconducting contacts, i.e. sending a direct current through the CNT while the voltage drop over it equals zero [12]. Additionally, measuring differential conductance through such a devices allows for the observation of the superconducting gap in a bias-voltage-dependent plot. The basic principles of those effects will be introduced in this section after a general introduction to the basics of electrical transport in superconducting materials is given according to the so-called BCS theory which can be found more detailed in, for example, the textbook of M. Tinkham [55].

2.3.1. The BCS theory of superconductivity

The BCS theory after Bardeen, Cooper, and Schrieffer [56] explains the zero electrical resistivity by a weak attractive force that pairs two electrons in the sea of conduction electrons. This force originates from the screened Coulomb field of one electron and acts via phonons through the lattice on the other electron. If this force exceeds the Coulomb repulsion, bound pairs of electrons with both, opposite momentum and spin are formed. As a result, these so-called Cooper pairs [57] have zero momentum and zero spin and, thus, no longer obey Fermi statistics for the energy distribution of half-integer spin particles, but Bose-Einstein statistics which is valid for bosons and allows the formation of a many-body ground state including all those electrons with energies around the Fermi energy E_F. As a consequence, all electrons whose difference in energy to E_F is smaller than the binding energy of a Cooper pair, are forming Cooper pairs in the so-called BCS ground state. This gives rise to an energy gap at E_F in the density of states (DOS) of the unpaired electrons, also referred to as quasi-particles, as it is shown in Fig. 2.15 (a) for $T = 0$. The gap separates occupied and empty states of quasi-particles and its total width is given by $2\Delta_0$, according to the binding energy of the paired electrons. Hence, the energy required to break up a Cooper pair determines the extent of the superconducting gap which can be expressed together with the formation of singularities at the gap edges by the superconducting BCS density of states

$$\rho_\mathrm{BCS}(E) \equiv \frac{N_\mathrm{s}(E)}{N_\mathrm{n}(E_\mathrm{F})} = \mathrm{Re}\frac{E}{\sqrt{E^2 - \Delta_0^2}} \tag{2.7}$$

where $N_\mathrm{s,n}$ is the DOS in the superconducting and the normal conducting state, respectively, and E gives the energy with respect to E_F. For finite temperatures $0 < T < T_\mathrm{c}$, the occupation of quasi-particles is given by the product of Eq. (2.7) and the Fermi-Dirac distribution (see Eq. (2.6)). Therefore, thermal excitation of electrons and holes across the gap becomes possible, as it is depicted in Fig. 2.16 (a). Increasing the temperature gives rise to a decrease of the effective gap width and finally to a transition to the normal conducting state at $T = T_\mathrm{c}$. The temperature dependence of Δ_0 follows the BCS theory and is determined by the excitation energy of fermion quasi-particles, the DOS at the Fermi energy, and the electron-phonon interaction strength [55]. For $T = 0$, the relation

$$\frac{\Delta_0(0)}{k_\mathrm{B} T_\mathrm{c}} \approx 1.76 \tag{2.8}$$

can be derived, where the Boltzmann constant $k_\mathrm{B} = 8.62 \cdot 10^{-5}$ eV/K relates temperature with thermal energy. The function $\Delta_0(T)$ decreases monotonically; near $T = 0$ its temperature dependence is very weak [55], hence the gap

is nearly constant. In order to decrease Δ_0, a significant number of Cooper pairs has to be thermally excited to the normal state. Thus, if the temperature is further increased, the closing of the gap occurs faster with T and close to T_c it follows [55]

$$\frac{\Delta_0(T)}{\Delta_0(0)} \approx 1.74\sqrt{1-\frac{T}{T_c}}. \tag{2.9}$$

while the total trend of the gap width as a function of temperature can be approximated [58] by

$$\frac{\Delta_0(T)}{\Delta_0(0)} \approx \tanh\left(1.74\sqrt{\frac{T_c}{T}-1}\right) \tag{2.10}$$

as it is is depicted in Fig. 2.15 (b).
As a consequence for experiments on superconducting contacts, it is favorable to keep their temperature well below the critical temperature in order to have an energy gap of reasonable width. Another important parameter for experiments is the spacial size of a Cooper pair which is of the order of the BCS coherence length $\xi_0 = \hbar v_F/\pi\Delta_0(0)$ [55] with the Fermi velocity v_F. It plays a role at the interface of a superconductor to another system and determines the probability of the injection of Cooper pairs via the superconducting proximity effect.
As the second main characteristic, a superconductor is a perfect diamagnet, i.e. external magnetic fields are expelled completely from its interior. Any

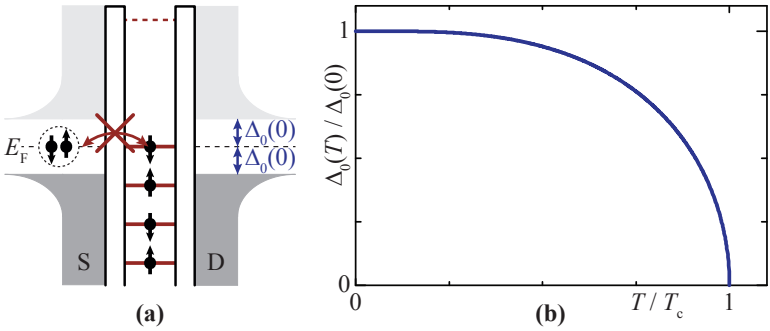

Figure 2.15.: (a) Schematic energy diagram of a CNT QD with two superconducting leads. The quasi-particle DOS $N_s(E)$ exhibits a total superconducting gap of $2\Delta_0$ near the Fermi energy which causes a suppression of quasi-particle tunneling through the QD within the gap. **(b)** Temperature dependence of the energy gap according to BCS theory and approximated by Eq. (2.10).

penetrating field induces the generation of screening currents by which it is countered instantaneously; a feature that is called the Meissner effect [59]. Since this screening is carried by Cooper pairs, it is dissipationless unless the kinetic energy of the Cooper pairs exceeds their binding energy. That means, there is a critical magnetic field that breaks the superconducting charge carriers and thus leads to a transition to the normal state. This feature can be used in experiments to investigate a superconducting system in its normal state without increasing the temperature. Generally, superconducting electrodes provide a useful tool in CNT QD experiments; e.g. they can be used as a superconducting tunnel probe to gain enhanced spectroscopic resolution due to the sharp peak in the BCS DOS [60], in addition, they lead to an enhancement of cotunneling spectroscopy with pronounced cotunneling thresholds [16].

2.3.2. Electrical transport through a quantum dot with superconducting contacts

Superconducting leads generally cause a suppression of single-electron transport through a QD in the low-bias regime that cannot be lifted by means of back-gate voltage induced level shifts (see Fig. 2.15 (a)). Even in case of a resonant situation, i.e. a QD level is aligned to the chemical potential of the leads, tunneling through the QD is not possible due to the gap in the quasi-particle DOS. Only applying bias of at least $eV_{\mathrm{sd}} = 2\Delta_0$ allows for a level alignment with available quasi-particle states in the leads (see Fig. 2.16 (a)). As a consequence, a measurement of the two-dimensional stability diagram yields an additional vertical gap of zero conductance in the V_{sd} sweep direction, amounting to $4\Delta_0$, as it is depicted as the grey area in Fig. 2.16 (b). Since single-electron tunneling via the QD is not possible within the gap, the resulting Coulomb diamonds are split and divided, respectively. In case the bias voltage equals the total gap width, the probability of direct tunnel events from electron-like states in S to hole-like states in D is strongly enhanced at finite temperatures. Hence, even in an off-resonant situation, the peaks representing a high DOS at the gap edges of both leads give rise to horizontal ridges of increased conductance for $|eV_{\mathrm{sd}}| = 2\Delta_0$; they are depicted as blue lines in Fig. 2.16 (b).

So far, only the ideal situation for zero temperature without any broadening of the QD levels or the superconducting gap edge has been considered. Yet, in most experiments [14], a small leakage current persists within the energy gap even for the lowest temperatures, which cannot be explained by a decreased gap width due to temperature effects or by thermal excitation of quasi-particles across the gap. Thus, the so-called Dynes model [61] in the superconducting

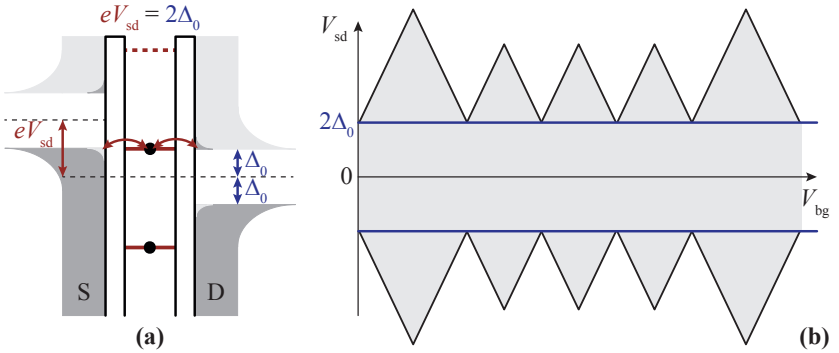

Figure 2.16.: (a) Schematic energy diagram of a CNT QD with two superconducting leads at finite bias and thermally excited quasi-particle states across the gap due to finite temperature. Charge transport is blocked within the superconducting gap and becomes only possible if its width is overcome by applying bias of at least $eV_{sd} = 2\Delta_0$, given a proper alignment of one QD level via V_{bg}. **(b)** The resulting stability diagram exhibits an additional blockaded region of a total vertical width of $4\Delta_0$ that splits and divides the original Coulomb diamonds. In addition, there are horizontal ridges of increased conductance at $eV_{sd} = \pm 2\Delta_0$ due to the peaks in the DOS of the leads.

leads is taken into account in order to characterize this finite leakage. It describes an effective smearing of the originally sharp peaks at $\pm\Delta_0$ in the quasi-particle DOS, which can be attributed to a lifetime-broadening of the states at the energy gap edges. This broadening has been determined experimentally [61–63] by measuring the electrical current through a superconducting tunnel junction, which is given by

$$I(V) = I_n \int_{-\infty}^{+\infty} \mathrm{d}E\ \rho(E)\rho(E+eV)\left[f_{FD}(E) - f_{FD}(E+eV)\right] \tag{2.11}$$

with the normal-state current I_n. This term is also approximately valid in a QD system with superconducting leads if the back-gate is tuned to the middle of a Coulomb diamond, since here, the off-resonant QD in addition to the barriers can be considered as a combined tunnel barrier. In order to fit the measured data, the BCS-like quasi-particle DOS of Eq. (2.7) has to be modified by the introduction of an imaginary term γ to the energy that represents the lifetime effects at the gap edge [61]:

$$\rho_{Dynes}(E,\gamma) = \mathrm{Re}\frac{E - \mathrm{i}\gamma}{\sqrt{(E-\mathrm{i}\gamma)^2 - \Delta^2(E)}} \tag{2.12}$$

Substituting this term for $\rho(E)$ in Eq. (2.11) then yields the measurement of $I(V)$ where the broadening is determined by the γ term. The application of this Dynes DOS allows for the direct measurement of, for example, the quasiparticle recombination time in a superconductor [61].

2.4. Phonons in suspended carbon nanotube quantum dots

Their very low density of $\rho \approx 1.3$ g/cm^3 in combination with a huge stiffness displayed by a Young's modulus of $Y \approx 1$ TPa lead to some extraordinary vibrational properties of CNT devices, which therefore can not only carry an electrical current, but it is also possible to excite various vibrational modes, provided that they are, at least partially, suspended. The involved energy scales of these distinct modes are rather different and strongly depend on the mechanical properties of the CNT. Additionally, a coupling between the electronic and vibrational system is possible, not only in single C_{60} molecules [64], but also in CNTs and can lead to a number of interesting effects, such as the so-called Franck-Condon blockade, which is based on the Franck-Condon principle and will be explained in the following. Yet first, a short introduction to the various vibrational modes of a suspended CNT is given.

2.4.1. Vibrating carbon nanotubes

There are three basic vibrational modes in a suspended CNT that are generally distinguished: First, the transverse acoustic (TA), or bending mode, is comparable to the motion of a guitar string and its oscillator zero-point motion is larger than 1 pm [27], as a consequence of the CNT's very low mass. In driven resonator experiments the TA mode is excited by applying an AC driving voltage to either a nearby antenna [8, 10, 65] or a gate close to the CNT [66]. If this driving frequency is nearly matching a mechanical eigenmode, the resulting increase of the displacement yields a larger variation of the gate-capacitance to the CNT. As a consequence, charge is induced on the CNT leading to a change of conductance. Frequency mixing techniques, where an additional AC bias voltage is applied with a small frequency offset, allow to detect the transverse vibrations even at room temperature [67]. Second, the longitudinal acoustic (LA), or longitudinal stretching mode, can be excited by electronic transport through the CNT and is observed at cryogenic temperatures [5, 28]. And third, there is the radial breathing mode (RBM), where the vibration arises in a periodic variation of the CNT diameter. It is widely used for experimental determination of the diameter and the chirality [68] of indi-

vidual CNTs by means of Raman spectroscopy. Scanning tunneling microscopy experiments have shown that tunneling electrons in a suspended CNT can emit and absorb phonons [69]. The energies of the different vibrational modes are plotted in Fig. 2.17. Whereas the vibration energy $E_{\mathrm{vib}} = \hbar\omega$ of the RBM is independent of the CNT length L and equals $E_{\mathrm{vib,RBM}} \approx 28$ meV/d[nm] [5] with the CNT diameter d, the TA mode energy shows a length dependence of L^{-2} [70] and is rather small [71] with $E_{\mathrm{vib,TA}} \approx 10^{-4}$ meV for a CNT of length $L = 1$ µm. The LA mode is inversely proportional to L [72] and exhibits

$$E_{\mathrm{vib,LA}} = \frac{\nu h}{L}\sqrt{\frac{Y}{\rho}} \tag{2.13}$$

with the vibrational quantum number ν and Planck's constant h. The fundamental mode $\nu = 1$ can be calculated to

$$E_{\mathrm{vib,LA}} = \frac{110\ \mu\mathrm{eV}}{L\ [\mu\mathrm{m}]} \tag{2.14}$$

Here it becomes clear that Eq. (2.13) yields, as a result of the huge Young's modulus and the low density of a CNT, a large energy spacing of the vibrational modes that can be observed for thermal energies $E_{\mathrm{th}} = k_{\mathrm{B}}T < E_{\mathrm{vib}}$, with the Boltzmann constant k_{B}. This is already valid for temperatures in the low Kelvin regime. Together with the fact that it can be excited by an electrical

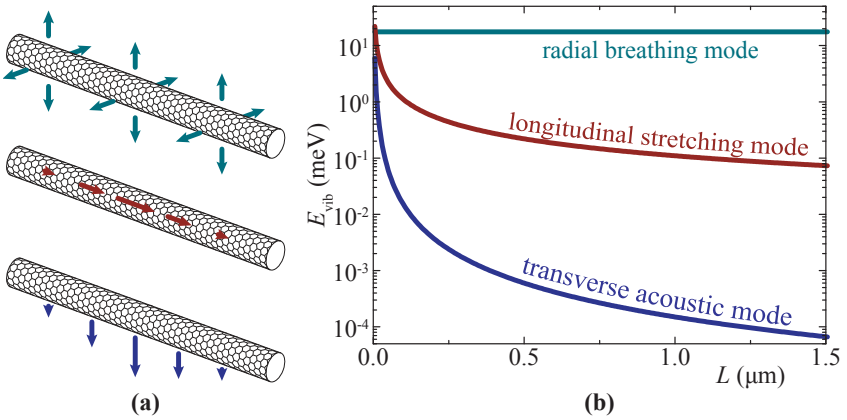

Figure 2.17.: (a) Different vibrational modes of a suspended CNT and **(b)** the according oscillator energy scales. While the RBM only depends on the inverse CNT diameter d but not on its length L, the longitudinal stretching mode and the bending mode exhibit a length dependence of L^{-1} and L^{-2}, respectively (adapted from Ref. [5]).

current, this keeps the experimental effort quite low for the investigation of the longitudinal stretching mode. The vibrational modes are coupled to the electronic levels of a CNT quantum dot, which will be explained in the following according to the Franck Condon principle.

2.4.2. The Franck-Condon principle

An electromechanical system enables transitions that simultaneously change both, the electronic and the vibrational quantum number in a molecule. They require the coupling of two subsystems in the molecule of very different properties; especially the mass of the involved charge carriers m_{e^-} is much smaller than that of the vibrating nuclei m_n, which allows for a much faster movement of the electrons. Thus, according to the Born-Oppenheimer approximation, the electronic and the nuclear motion become decoupled and consequently, the latter is independent on the exact coordinates of the electrons. Therefore, changes in the wave function of the electrons are essentially instantaneous for the nuclei. The intensity of possible simultaneous transitions can be explained by the Franck-Condon principle (FCP) [73, 74], a spectroscopic rule that is based on these characteristics: during electronic transitions the distance of the nuclei R does not change. Figure 2.18 depicts the basic principle of possible transitions in, for instance, a diatomic molecule that is in its electronic and vibrational ground state in a Morse potential: $n = 0$ and $\nu = 0$, respectively, where n is the electronic and ν the vibrational quantum number. An electronic transition changes the electron density and therefore causes the nuclei to respond, i.e. excites a vibration. The electronic excited state $n = 1$ typically exhibits a larger internuclear separation R than the ground state. According to the FCP, vibrational transitions have to occur vertically in this energy-diagram. Therefore, an electronic excitation favors the vibrational transition from ν to ν'. Hence, the final vibrational level is the one that has the same R as the initial vibrational state.

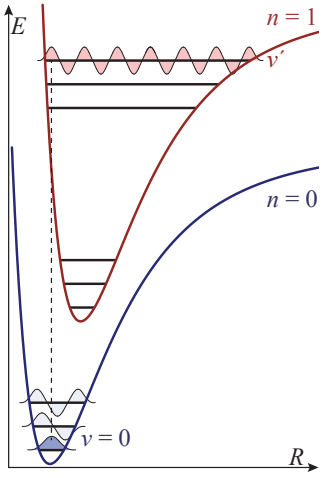

Fig. 2.18.: Franck-Condon principle. The much smaller mass of the electronic system allows only for vertical transitions and results in the excitation of phonons.

For a quantum mechanical explanation of the FCP, an electronic dipole transition is considered: from Ψ_{e^-} and Ψ_n to Ψ'_{e^-} and Ψ'_n, i.e. from its electronic ground and vibrational initial state to an electronic excited and vibrational final state, respectively. The operator of the dipole is written as

$$\vec{\mu} = \vec{\mu}_{e^-} + \vec{\mu}_n = -e \sum_i \vec{r}_i + e \sum_j Z_j \vec{R}_j \tag{2.15}$$

with the charge $-e$ $(+eZ)$ and positions $\vec{r}$ $(\vec{R})$ of the electrons (nuclei). If electronic transitions in this molecule are regarded as perturbation, their rates can be calculated by means of *Fermi's golden rule*

$$T_{i\to f} = 2\pi \left|\langle f \left| \vec{\mu} \right| i\rangle\right|^2 \delta\left(E_f - E_i\right), \tag{2.16}$$

a general expression for a transition rate $T_{i\to f}$ from an initial state $|i\rangle$ to a different final state $|f\rangle$, with the transition matrix $\vec{\mu}$. In perturbation theory, these states are coupled due to some weak perturbation that accounts for a finite overlap of the wave functions (see for example [75] for a more extensive derivation). Applying this to the transitions T of the dipole, in combination with the Born-Oppenheimer approximation, results in [76]:

$$\begin{aligned} T &= \left\langle \Psi'_n \Psi'_{e^-} \middle| \vec{\mu} \middle| \Psi_n \Psi_{e^-} \right\rangle \\ &= \left\langle \Psi'_n \Psi'_{e^-} \middle| \vec{\mu}_{e^-} \middle| \Psi_n \Psi_{e^-} \right\rangle + \left\langle \Psi'_n \Psi'_{e^-} \middle| \vec{\mu}_n \middle| \Psi_n \Psi_{e^-} \right\rangle \\ &\approx \underbrace{\left\langle \Psi'_n \middle| \Psi_n \right\rangle}_{\substack{Franck\ Condon \\ factor}} \cdot \underbrace{\left\langle \Psi'_{e^-} \middle| \vec{\mu}_{e^-} \middle| \Psi_{e^-} \right\rangle}_{\text{selection rule}} + \underbrace{\left\langle \Psi'_{e^-} \middle| \Psi_{e^-} \right\rangle}_{=0} \cdot \left\langle \Psi'_n \middle| \vec{\mu}_n \middle| \Psi_n \right\rangle \end{aligned} \tag{2.17}$$

Thus, the Franck Condon factor is defined as the overlap integral of the involved nuclear wave functions. It yields a larger change of ν for a larger change of R during the transition. The second term is equal to zero because electronic wave functions of different states are orthogonal for electronic dipole transitions.
For a constant R during the transition, the quantum number of the vibration is the same before (ν) and afterwards (ν'), as it is illustrated by the diagonal line of possible transitions in Fig. 2.19 (a). If R changes, the possible transitions are located on a parabola (see Fig. 2.19 (b)). The FCP not only explains the excitation of vibrations by an electronic transition, but it can also describe electron-phonon interaction in QDs where it can lead to a significant current suppression in transport through QD in the low-bias regime for a strong coupling between the vibrational and the electronic degrees of freedom. This effect was theoretically predicted [77, 78] and experimentally demonstrated [29] and is called phonon blockade or Franck-Condon blockade.

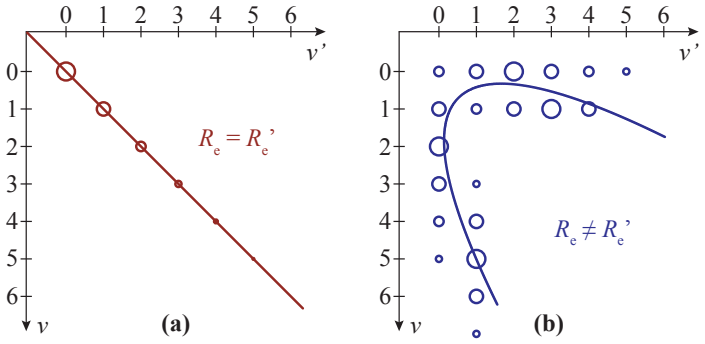

Figure 2.19.: Possible vibrational transitions from ν to ν' in a diatomic molecule, **(a)** for a constant distance of the nuclei, and **(b)** for a changing inter-nuclei distance (adapted from Ref. [76]).

2.4.3. Franck-Condon blockade

In a suspended QD tunneling electrons are able to excite phonons [5, 79, 80] that can be observed in transport measurements as equidistant excited state lines running parallel to electronic states of high conductance [28, 29, 64, 79, 81] since transport is enhanced at multiples of the phonon's energy $\hbar\omega$. The FCP describes the interplay between the vibrational and electronic degrees of freedom in a molecule and can be transferred to a vibrating QD: If additional charge carriers enter the QD, they affect the vibrational system by deforming the embedding medium and thereby shifting the equilibrium coordinate of the oscillator by an amount proportional to the electron-phonon coupling [29]. A theory on intrinsic electron-phonon coupling in CNT QDs has been introduced by E. Mariani and F. von Oppen [80]. Consistent with experiments, it shows that the largest electron-phonon coupling constant is obtained for the longitudinal stretching mode, where it is given by $g = 1/2(L/L_0)^2$ [5], with the quantum mechanical oscillator length $L_0 = \sqrt{\hbar/m\omega}$, mass m, and the CNT length L.

A schematic description of the Franck-Condon blockade is shown in Fig. 2.20. The vibrational potential for N electrons on the QD is given by the blue curve with a phonon in its ground state. Adding an electron to the dot shifts the potential by a value proportional to g. This leads to a small displacement for a weak coupling $g \ll 1$ (see Fig. 2.20 (a)) and accordingly to a large displacement for strong coupling $g \gg 1$ (see Fig. 2.20 (b)), respectively. For a small shift only transitions to the ground state are possible, since the initial ground state is essentially orthogonal to all excited states after the transition. In contrast, for a large shift, the overlap of initial and final state with $\Delta\nu \simeq 0$ (small

vibrational energy difference) is very small. This allows only for transitions to excited states in the high-bias regime and at the same time causes a suppression of electronic transitions in the low-bias regime. This resulting suppression of current flow is called Franck-Condon blockade (FCB) and typically cannot be lifted by means of a gate voltage.
The FCB can be modeled by a molecule weakly coupled to metallic contacts. Transport through such a system is theoretically assumed to be caused by tunneling via one spin-degenerate electronic level in the presence of one vibrational mode. This results in a strongly g-dependent suppression of conductance in the low-bias regime [77, 78, 82]. For a large g, the Franck-Condon factors yield transition rates that are exponentially small. Therefore, a large bias voltage of $eV \sim g^2\hbar\omega$ is necessary in order to overcome the blockaded regime and make transitions to highly excited phonon states possible. Furthermore, the Franck-Condon model predicts equidistant excited lines where the progression of the peak heights is given by [5, 29]:

$$G_\nu^{\max} \propto |T_{0-\nu}|^2 \propto \frac{g^\nu e^{-g}}{\nu!} \tag{2.18}$$

In several experiments on vibrating QDs in the Franck-Condon regime, excitations of phonons are accompanied by negative differential conductance (NDC) [5, 29, 83, 84] that cannot be explained by the constant interaction model. Thus, there is a lot of effort in theoretical models [85–88] to explain this fea-

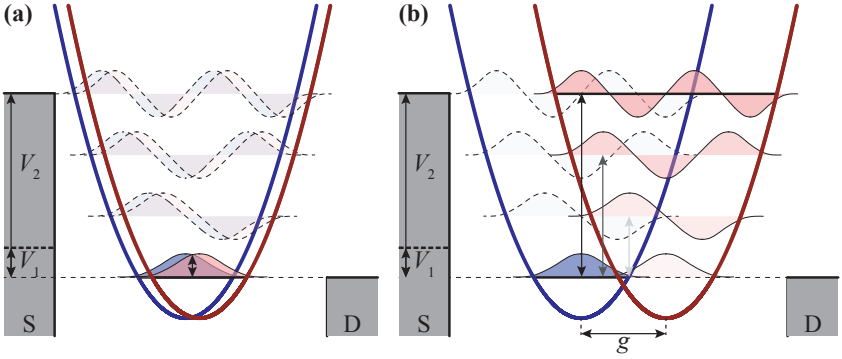

Figure 2.20.: Schematic principle of Franck-Condon blockade. The phonon potential for N electrons on the quantum dot contains a ground state (blue curves), whereas the red curves represents the shifted potentials for an additional electron $(N + 1)$. **(a)** A weak electron-phonon coupling g leads to a small displacement and enables transitions between the ground states. **(b)** For a strong coupling only transitions to excited states are possible which require an increased bias voltage $V_2 > V_1$.

ture. They include multiple electronic levels or an asymmetric coupling of the junction [89, 90] as proposal to explain NDC. It is also attributed to spatially dependent Franck-Condon factors that become asymmetric as the phonon and electronic states have different locations and sizes on the QD [83, 91] or to an asymmetric device in combination with weak relaxation of the phonon excitation [77]. The respective lengths can be determined from experiment, where the size of the Coulomb diamonds yields the size of the QD (see Eq. (2.5)), while the energy separation of the vibrational sub-bands yields the length of the vibrating part (see Eq. (2.13)). Another possibility is screening effects being responsible for NDC [92]. Concluding, there a several different models and possible explanations for NDC in the FCB regime. On the other hand, NDC also appears in experiments on a non-vibrating QD [93], but since it implies spin-polarized contacts, the only known origin of NDC in single QDs with normal metal leads is the presence of vibrations.

2.5. The physics of carbon nanotube-metal contacts

The electrical contacts between the leads and the CNT play a crucial role in QD devices, since they have a large influence on the tunnel-coupling and hence the transparency of the device. In addition to the cleanliness of the interface, the formation of barriers and the overlap of the electronic states of CNT and metal are important factors concerning electronic coupling. This section gives an introduction to the formation of Schottky barriers at the metal interface to semiconducting CNTs. It is based on the focused review article of J. Svensson and E. E. B. Campbell [94]. Furthermore, electrostatic and density functional theory models are considered in order to describe the formation of tunnel barriers at metal contacts to metallic CNTs, which cannot be explained by means of the Schottky barrier model. They are used to calculate the barrier height for bulk systems on the mesoscopic and for molecule systems on the atomic length scale, respectively.

2.5.1. Formation of Schottky barriers at semiconductor-metal contacts

The simplest model to describe the barrier height between metal and semiconductor is the alignment of the Fermi levels of the metal and the semiconductor. Due to Fermi energy mismatch in the two bulks, charge carriers move across the interface and leave a space charge or depletion region background in their initial material. The mismatch of the initial Fermi levels of the metal $E_{\mathrm{F,m}}$ and the semiconductor $E_{\mathrm{F,s}}$ (see Fig. 2.21 (a)) then corresponds to the height of the

so-called Schottky barrier that consequently forms at the interface. According to the first theoretical description by Schottky and Mott [95, 96], the height of the Schottky barrier for electrons and holes can be given by

$$\Phi_{\mathrm{SB,e}} = \phi_{\mathrm{m}} - \chi \tag{2.19}$$

$$\Phi_{\mathrm{SB,h}} = \chi + E_{\mathrm{g}} - \phi_{\mathrm{m}} \tag{2.20}$$

respectively. The energy needed to remove an electron from $E_{\mathrm{F,m}}$ ($E_{\mathrm{F,s}}$) to the vacuum is given by the work function of the metal ϕ_{m} (semiconductor ϕ_{s}), while the energy needed to remove an electron from the bottom of the conduction band of the semiconductor with band-gap E_{g} is given by the electron affinity χ. Since semiconducting CNTs are typically of p-type, i.e. $\phi_{\mathrm{m}} > \phi_{\mathrm{s}}$, an example of a Schottky barrier with a p-type semiconductor is sketched in Fig. 2.21 (b). The sign of $\Phi_{\mathrm{SB,h}}$ gives the type of contact: a positive value indicates the existence of a Schottky barrier that results in an asymmetric $I(V)$-curve, a so-called Schottky diode. For a negative value no barrier is present and the junction is referred to as an Ohmic contact with constant $\mathrm{d}I/\mathrm{d}V$ behavior. Consequently, a low contact resistance between metal and semiconductor is gained by choosing materials of similar work functions.
However, this simple model fails to describe an experimentally observed non-linearity in the barrier height as a function of the metal work function [97]. Hence, another effect that is able to explain this reduced dependence of the Schottky barrier height (SBH) on ϕ_{m} has to be taken into account. This is

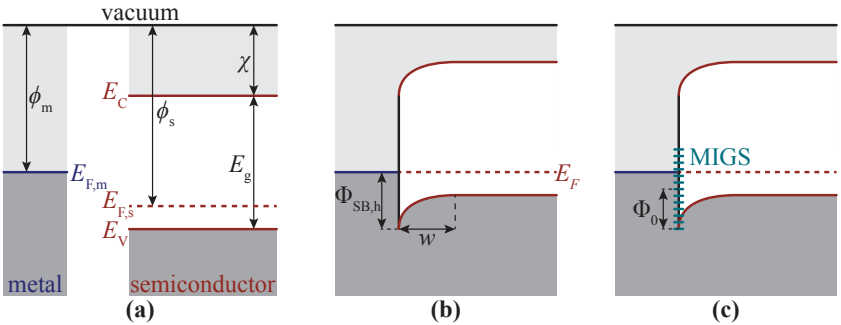

Figure 2.21.: (a) Energy band diagrams of separated metal and p-type semiconductor with different work functions ϕ_{m} and ϕ_{s}, respectively. **(b)** If they are brought into contact, the realignment of the Fermi levels $E_{\mathrm{F,m}}$ and $E_{\mathrm{F,s}}$ leads to the formation of a Schottky barrier for hole transport at the interface of height $\Phi_{\mathrm{SB,h}}$ and width w. **(c)** Energy band diagram including metal-induced gap states (MIGS) at the interface. In combination with their image charge in the metal they form a dipole that affects the SBH: the difference between their charge neutrality level Φ_0 and E_{F} adds to $\Phi_{\mathrm{SB,h}}$ (adapted from Ref. [94]).

done by using the concept of Fermi-level pinning as it is shown in Fig. 2.21 (c). At the metal-semiconductor interface, the electron wave functions in the metal extend into the semiconductor and give rise to so-called metal-induced gap states (MIGS) within the band-gap of the semiconductor. A charge neutrality level Φ_0 can be defined [94] with respect to the top of the valence band in such a way that it separates donor type from acceptor type MIGS. As a consequence the Fermi energy level positioned below/above Φ_0 determines whether the surface of the semiconductor has a positive/negative charge. On the other hand, E_F coinciding with Φ_0 yields no trapped charges at the interface. In combination with their image charge in the metal, the resulting MIGS then form a dipole at the surface of the semiconductor which finally leads to a modification of the Schottky barrier by a potential drop over this dipole and therefore the SBH can be described by

$$\Phi^*_{\mathrm{SB,e}} = \beta\,\Phi_{\mathrm{SB,e}} + (1-\beta)\,(E_\mathrm{g} - \Phi_0) \tag{2.21}$$

$$\Phi^*_{\mathrm{SB,h}} = \beta\,\Phi_{\mathrm{SB,h}} + (1-\beta)\,\Phi_0 \tag{2.22}$$

where $\beta = (1 + qD\delta/\epsilon)^{-1}$ with the MIGS density D, the dipole dimension δ, and the permittivity of the interface ϵ [94]. Hence, the SBH is mostly defined by the interface states for larger D. For $D = 0$, Eqs. (2.21) & (2.22) reduce to the description from Schottky and Mott of Eqs. (2.19) & (2.20).

Experimental investigations of the SBH as a function of ϕ_m have been done for different contact materials to CNTs. Most of them have come to similar results: Metals with high ϕ_m make good p-type contacts to CNTs, whereas low ϕ_m metals yield good n-type contacts [43, 98–100]. As discussed before, equal work functions of metal and the CNT are preferable, where the latter is given by $\phi_\mathrm{CNT} = 4.9 \pm 0.1$ eV [94]. The best contacts, i.e. the junctions that yield the highest currents, are obtained with palladium (Pd) and show a minimum resistivity of $R_\mathrm{min} = 6.5$ kΩ [98] with $\phi_\mathrm{Pd} = 5.1$ eV [100].

Z. Chen *et al.* [101] have used a large set of devices to demonstrate the dependence of the maximum current through the CNTs on the respective work function of three different metals: Pd, titanium (Ti), and aluminum (Al). Furthermore they have investigated the influence of different CNT diameters d. They have concluded that the SBH is inversely proportional to d and in addition, that it is reduced with an increase of ϕ_m for three different contact metals with: $\phi_\mathrm{Pd} = 5.1$ eV, $\phi_\mathrm{Ti} = 4.3$ eV, and $\phi_\mathrm{Al} = 4.1$ eV.

However, the effect of Fermi level pinning by means of MIGS makes it difficult to predict SBH simply from the characteristic material properties ϕ_m and ϕ_s. Additionally, other properties of the contacts have to be taken into account, like wetting of the tendency to form covalent bonds at the interface, which also affects the contact resistivity. This can be done by means of theoretical models that will be discussed in the following.

2.5.2. Electrostatic modeling of carbon nanotube-metal contacts

In order to investigate the SBH for different metals, theoretical studies have been done by F. Léonard *et al.* [102, 103] who use an electrostatic model to calculate the potential distribution for bulk objects where the CNT is considered an ideal cylinder with a diameter of $d = 1.4$ nm. This method calculates the energy of the bands and allows the modeling of real device dimensions. Since the band-gap of a semiconducting CNT is inversely proportional to its diameter (see Eq. (2.4)), it is expected that the SBH shows the same diameter dependence, given that the work function of the CNT is independent of its diameter. Their studies also predict that the SBH of a CNT-metal contact should be fully controlled by the metal work function while Fermi level pinning does not play a role [94], which is in contrast to bulk junctions.
However, the concepts of bulk semiconductor/metal contacts do not simply apply for nanoscale devices [103], where the diameter of a CNT is too small to allow for a full realignment of the semiconductor bands. Additionally, the effect of Fermi level pinning is much less dominant in such quasi one-dimensional structures.

2.5.3. Density functional theory modeling of carbon nanotube-metal contacts

Theoretical studies on the atomic length scale usually consider two different ideal contact geometries: either strong covalent bonds between the metal surface and dangling bonds at the end of an open, uncapped CNT; or the side-contact configuration of a CNT lying on the metal and linked by weak van der Waals bonds [94]. Since almost every experimental study has been performed on metals bonded to the side of CNTs, only calculations on this configuration will be considered here. The density functional theory (DFT) is applied in order to calculate the spatially dependent electron density in a many-body system, which allows the consideration of the atomic configuration of small diameter CNTs in combination with metal contacts. This is in contrast to bulk systems in electrostatic models introduced before, but due to the requirement of the large computational resources, with DFT only calculations of contacts including a few hundred atoms are possible. However, DFT modeling has led to various interesting results:
V. Vitale *et al.* [104] have done DFT computations in order to study the influence of different contact materials and to gain information on the formation of barriers and the electrical behavior due to the bonds that form at the interface. They have observed that using Pd contacts leads to the formation of more bonds compared to Al, and therefore a reduced SBH. This is depicted

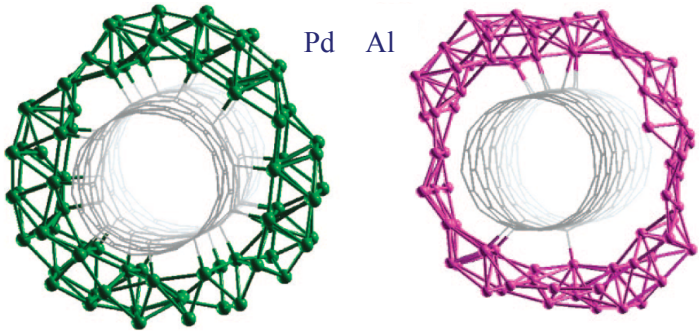

Figure 2.22.: Structure of the calculated side contacts to a (10,0) CNT for Pd and Al metals. Pd forms more bonds and therefore shows a better wetting of the CNT compared to Al (Image taken from Ref. [104]).

in Fig. 2.22 and can be explained by the π-electron system of the CNT that is almost exclusively involved in the chemical bonding to the Pd atoms. As a result, the Pd atoms arrange in such way that the number of bonds is maximized, i.e. Pd tends to wet the CNT, which is in strong contrast to the bad wetting of Al. They have concluded that in addition to ϕ_{m} also the character of the chemical bonds at the contact determines the SBH.

The presented computational results suggest the conclusion that strong chemical bonds between CNT and metal contact correspond to a good electrical coupling. A combination with metals of similar work function with respect to the CNT is supposed to yield an optimum contact with lowest tunnel barriers [104, 105]. However, some experimental and theoretical studies have presented a large discrepancy in the results for the SBH with contradicting conclusions [94].
Although the origin is not quite clear yet, experimental investigations show a tendency that the choice of material has strong influence on the transparency of the contact. For example, Y. Matsuda [106] has shown that Ti yields the lowest contact resistance to a CNT, followed by Pd, platinum (Pt), copper (Cu), and gold (Au). Y. Zhang *et al.* [107] have deposited different metals directly on a suspended CNT in order to observe their tendency to stick to it. Their experiments have shown similar results and confirm that Pd has better wetting properties regarding the CNT and therefore is able to form more bonds. The metal on top of the suspended CNT has been either continuous (for Ti, nickel (Ni), and Pd) or deposited as isolated particles (for Au, Al, and iron (Fe)). This has been explained by different interactions of the respective metal with the sidewall of CNTs which are likely to be related to strong covalent

bonds resulting in a better wetting; whereas weaker van der Waals forces lead to less bonds and the formation of isolated particles. The authors conclude that stronger bonds correspond to a better electrical coupling.
Since most of the studies have been done on non-superconductors, different materials have been checked in the framework of this thesis in order to find a candidate that produces a low barrier and thus a higher chance for Cooper pair injections onto the CNT QDs. Concluding from the Schottky barrier model of this section, the high work function metal Re is a promising superconducting material. On the other hand, Pt has the highest work function but tends to make bad contact to CNTs. That is why besides the Schottky barrier also theoretical studies on microscopic length scale have to be considered, in order to take into account the chemical bonds and wetting properties of different materials at the metal-CNT interface.

3

Fabrication methods for as-grown carbon nanotube devices

Experimental results of the last years have shown that as-grown CNTs are remarkably free of defects and yield effects not seen before in conventional devices. They ask for a new preparation scheme, with the synthesis of the CNT being the last step, to allow for their cleanliness. This chapter focuses on the general preparation schemes of conventional and suspended as-grown CNT devices. Furthermore, the CNT growth process, chemical vapor deposition, and the fabrication method of superconducting thin films, magnetron sputter evaporation, are described in more detail. Afterwards, devices are pre-selected according to their electrical behavior at room temperature. Finally, the electrical measurement setup is introduced together with the basic principle of the different types of the cryogenic systems used in the framework of this thesis.

3.1. The conventional way of preparing carbon nanotube devices

Until now, most of the electronic CNT devices are prepared by evaporating contact materials onto pre-localized CNTs that have been grown randomly onto a substrate. In this thesis, this method is referred to as the *conventional* fabrication scheme; it is sketched in Fig. 3.1 and its single steps are described in the following:

Figure 3.1. ***(facing page)*:** The conventional way of fabricating CNT devices. See text for detailed descriptions of the single production steps and Appx. A for detailed process parameters.

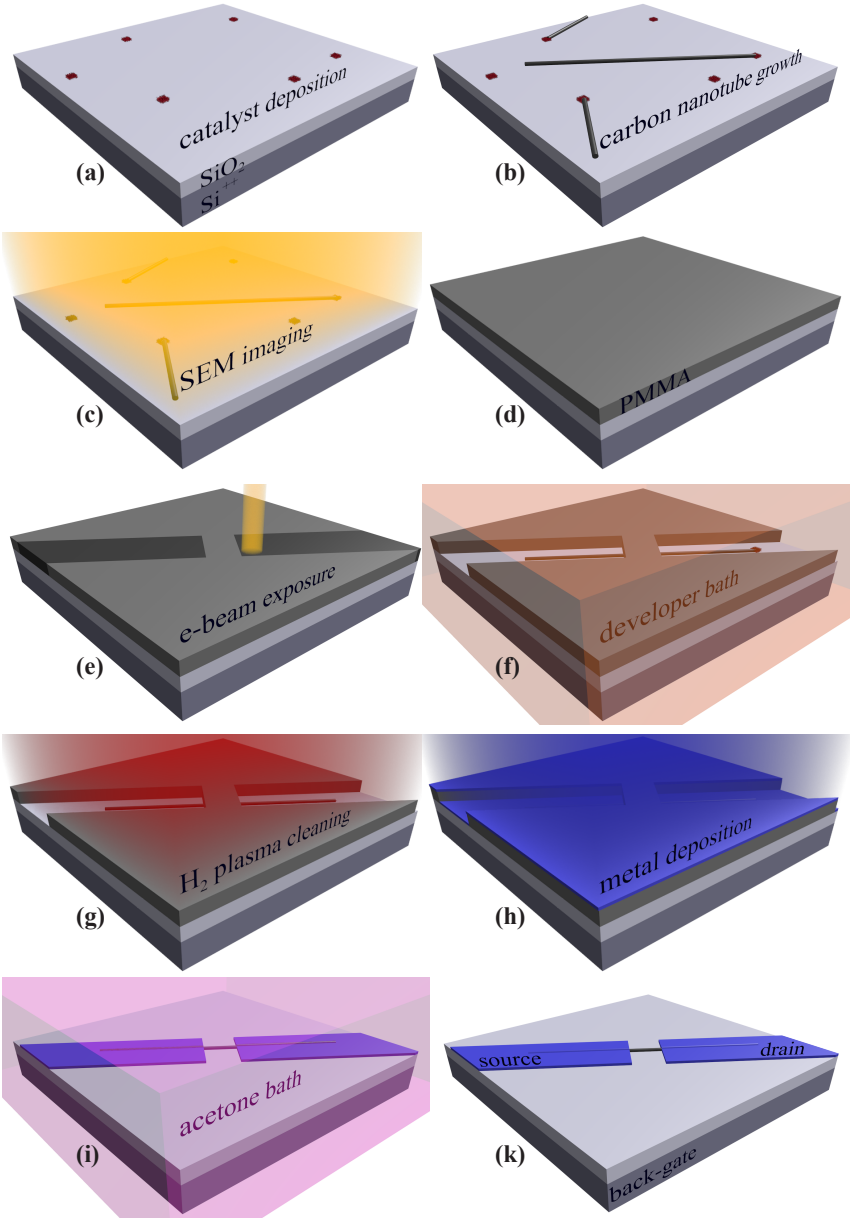
catalyst deposition
SiO_2
Si^{++}
(a)
carbon nanotube growth
(b)
SEM imaging
(c)
PMMA
(d)
e-beam exposure
(e)
developer bath
(f)
H_2 plasma cleaning
(g)
metal deposition
(h)
acetone bath
(i)
source
drain
back-gate
(k)

(a) The substrate is formed by a highly boron-doped Si^{++} wafer piece covered with an insulating, thermally grown SiO_2 layer of $\sim$ 400 nm thickness. It is cleaned by sonication in an acetone bath, followed by a treatment in UV ozone. Then, catalyst particles are dissolved and highly diluted in IPA to be deposited onto the substrate by **spin-coating**.

(b) CNTs are grown by **chemical vapor deposition** (CVD) (see Ch. 3.3).

(c) Individual **CNTs are localized** with respect to pre-defined marker grids and selected by imaging in a scanning electron microscope (SEM).

(d) Polymethyl methacrylat (PMMA) **spin-coating** deposits the electron beam (e-beam) resist onto the sample. The thickness of the resulting thin layer can be controlled by the amount of the diluent chlorobenzene.

(e) The **contact structures are patterned** and exposed by an e-beam in the SEM in order to break the resist's polymer chains.

(f) A treatment in a **developer bath** removes only those parts of the PMMA that have been exposed. The structuring described in **(d)**−**(f)** is commonly referred to as e-beam lithography (EBL).

(g) The developed areas are cleaned by **hydrogen** (H_2) **plasma** in order to get rid of possible PMMA residues sticking to the CNT.

(h) The contacts are prepared by **thin film deposition** (see Ch. 3.4) directly onto the substrate where the PMMA has been removed.

(i) The remaining PMMA is dissolved and removed in an acetone bath together with the metal on top of it in the so-called **lift-off** process, so that only the contact structures remain.

(k) The **device is ready** to be glued into a standard chip carrier and connected to it by Al wire bonding.

This conventional device fabrication method is well established, but it is apparent that the pre-grown CNTs have to suffer several production steps. First of all, they are located by SEM imaging where the high-energy e-beam can cause severe damage to the CNT, even in the low keV regime [11]. Furthermore, PMMA residues that cannot be completely dissolved during the developing process might keep sticking to the CNT. Therefore, an H_2 plasma cleaning step is applied to remove those residues, which in turn could again cause defects to the CNT. In order to prevent these various sources of contamination, a novel fabrication scheme is applied in the framework of this thesis that allows the CNT to be unaffected by growing it only as the last production step. This method has been introduced by Cao *et al.* [4] and is described in the following.

3.2. Fabrication scheme of as-grown carbon nanotube devices

As their main characteristics, *as-grown* CNTs are prepared as the last production step onto pre-fabricated electrodes. This is done by first following the steps **(d)**−**(i)** (skipping H_2 plasma cleaning **(g)**) of the conventional production scheme of Fig. 3.1 to design a pattern of electrode pairs by EBL and reactive magnetron sputter deposition. The subsequent steps are depicted in Fig. 3.2 and described in the following:

(a) The contacts are pre-fabricated onto a standard SiO_2 substrate by **EBL** and **thin film deposition** as introduced in Ch. 3.1.

(b) In order to grow fully suspended CNTs over the electrode gap, **trenches are opened by wet-etching** in buffered hydrofluoric (HF) acid. The electrode structures are used as etching mask.

(c) Small spots are defined on one electrode of each pair by a further **EBL** step to locally deposit catalyst particles by **spin-coating**. Since they tend to stick better to the edges of the PMMA, their effective lengths are increased by defining crosses with arm-length and arm-width of 1 µm each. This prevents them from being flushed away during lift-off.

(d) CNTs are grown as the last step by **CVD**. Since this a random process and CNT number, length, and growth direction can not be controlled, many samples have to be fabricated at the same time in order to gain a reasonable yield of devices with single CNTs connecting the electrodes.

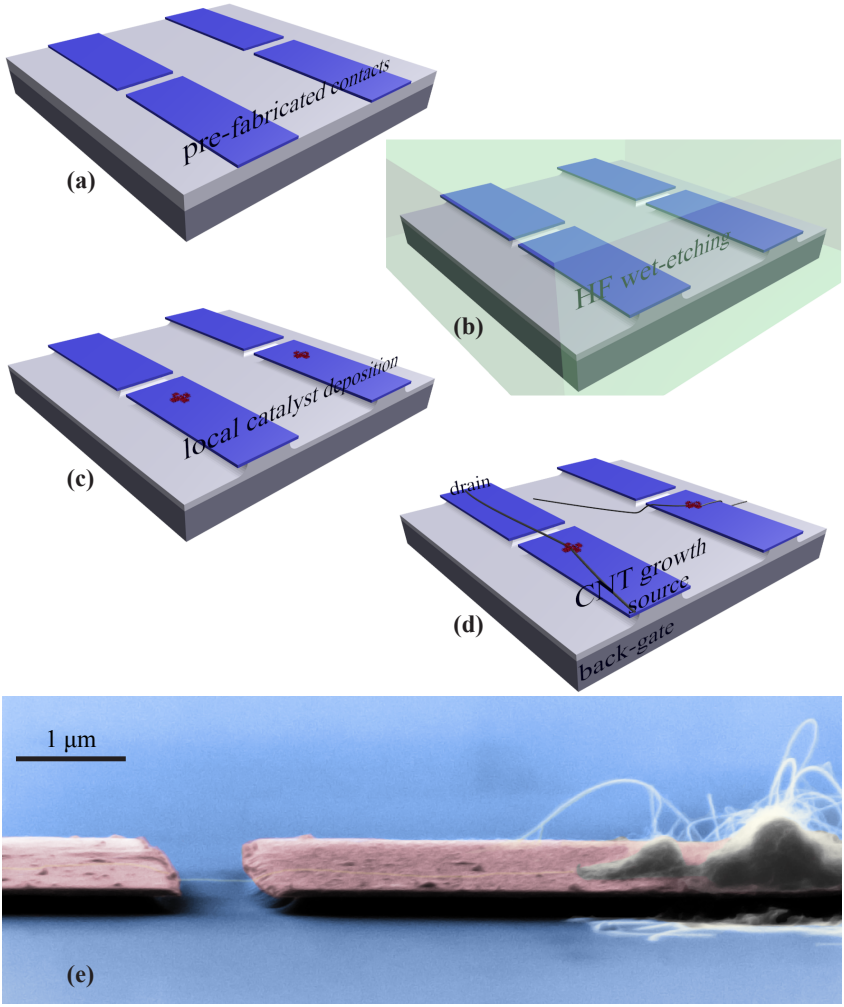

Figure 3.2.: Fabrication scheme of as-grown CNT devices. **(a)**−**(d)** See text for descriptions of the single production steps and Appx. A for detailed process parameters. Finally, the electrodes are connected to source and drain while the substrate is used as global back-gate. **(e)** Electron micrograph of the suspended, as-grown CNT Device D1. The accumulation of catalyst particles on the right electrode activates the growth of many CNTs during the CVD process. A QD forms in the suspended segment between the two contacts consisting of superconducting Re.

Finally, the sample is glued into a standard chip carrier and the contacts are connected correspondingly by Al wire bonding. Since the chip carriers and the wiring of the cyrostats is designed for 20 lines, a maximum number of 9 devices, i.e. electrode pairs, plus the global back-gate can be contacted in each chip. SEM imaging is only done after the measurements to avoid damaging by the high energy electron beam. Therefore after bonding, each device has to be checked electrically for CNTs contacting the two electrodes. The electron micrograph in Fig. 3.2 (e) demonstrates how an ideal as-grown, suspended CNT device should look like. In general, four different kinds of samples are prepared in the framework of this thesis and are labeled accordingly:

A: conventionally prepared devices as introduced in Ch. 3.1 with SEM located CNTs and post-deposited contacts

B: same as **A** with additional recessed bottom-gates

C: devices with as-grown CNT on top of pre-fabricated electrodes as introduced in Ch. 3.2

D: same as **C** with additional trenches between the electrodes opened by HF etching

3.3. Chemical vapor deposition of carbon nanotubes and device characterization

The growth process of CNTs is activated when a metal catalyst thermally decomposes some hydrocarbon vapor. This process is called chemical vapor deposition and is done in a special, in-house built reactor setup, where both, the flow-rates of the involved reaction and protection gases and the temperature can be well controlled. The catalyst solution (see the exact composition in Appx. A) is sonicated for at least three hours in order to break up clusters of particles [108]. This is crucial, since the diameter of the resulting CNTs is closely determined by the diameter of the catalytic particles [109]. After placing the catalyst onto the sample it is put into the CVD reactor where the heating to the final growth temperature of $850 - 950$ °C takes place under a protective and reducing Ar/H_2 atmosphere. Replacing Ar by methane (CH_4) feeding gas for $10 - 15$ min then activates the CNT-growth. Reversing these steps yields a stop of the growth process and ensures chemical protection during

the cool-down. If contacts have been pre-fabricated and additionally tend to form oxides, such as rhenium, the cool-down takes place in Ar/H_2 atmosphere to $T < 200$ °C before venting the reactor.

After the synthesis of the CNTs in the CVD reactor, the sample is tested at room temperature for electrical contact between each of the electrode pairs. This is done at the needle probing station where both bonding pads of a respective electrode pair and the back-gate can be contacted by sharp conducting needles. It is not only possible to check for the general device functionality, but also for several electronic properties of the devices, that means to determine if the respective CNT is metallic, semiconducting, or if it shows a small band-gap. While typical examples of the two latter cases are depicted in Fig. 3.3, a metallic CNT does not show any dependence $G(V_{bg})$. Sometimes it is possible to tell if the device consists of a single CNT or rather a bundle or several CNTs in parallel. For example, a positive offset in G within the band-gap regime of an actual semiconducting CNT, is sign of a parallel array of metallic and semiconducting CNTs. The high temperatures and the H_2-rich atmosphere make the CVD the most critical step in the whole fabrication scheme for the pre-fabricated superconducting contacts and limits the choice of materials drastically. Chapter 4 will discuss the challenge of finding and preparing materials that are suitable for this process.

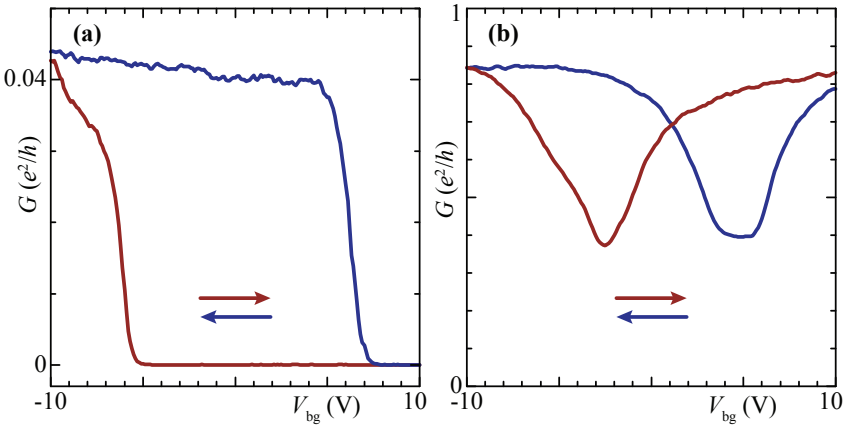

Figure 3.3.: Measured differential conductance G as a function of back-gate voltage V_{bg} at room temperature at the needle probing station. **(a)** Example of a semiconducting CNT. **(b)** Example of a small band-gap CNT (see Ch. 2.2).

3.4. Magnetron sputter deposition of superconducting contacts

The preparation of the contacts is done by magnetron sputter deposition in two different systems: the in-house built *ESCA3* machine and the commercial *AJA* system. They differ in their handling and some of the process parameters (see Appx. A for details), but the fundamental concept is the same: Ar gas is ionized to form a plasma near a target of the desired material which leads to the ablation of single atoms and thereby the formation of thin layers of controllable thickness on a substrate. This principle is basically sketched in Fig. 3.4.
The sputtering is done in an ultra-high vacuum (UHV) chamber with a base-pressure in the 10^{-9} mbar regime. Ar gas is introduced into the chamber to form a glow discharge plasma which can be defined as a region of relatively low-temperature gas containing positively charged Ar^+ ions and electrons. By applying bias to the target, the Ar^+ is accelerated towards it and thereby both, electrons and target atoms are released. Since the latter are neutral they are not influenced by electric and magnetic fields and can be deposited on the substrate. On the other hand, the electrons are ionizing further Ar and sustaining the plasma [110]. The two characteristic parameters of a plasma can be well controlled: first, the Ar pressure determines the degree of ionization $\alpha = N_{e^-}/(N_{Ar^+} + N_{Ar})$, with the respective densities N_i of electrons, Ar^+ ions, and Ar gas. Second, the electron energy distribution, approximated by the electron temperature T_{e^-} can be tuned by the strength of the electric field which has an additional effect on α.
The magnetron is positioned right beneath the sputter target in order to confine the charged plasma particles nearby its surface. It consists of a ring-shaped magnet with out-of-plane magnetization and a counterpart with opposite magnetization direction in the center of the ring. This configuration gives rise to magnetic field lines above the target that make electrons move helically along them near the surface. Thus, the number of ionizing collisions is increased locally. This results in more Ar^+ ions which allow for a higher ablation rate at a relatively low plasma pressure. This is important, since it keeps the mean free path of the sputtered atoms large and consequently the deposition rate as well. The magnetic trap does not affect the neutral sputtered atoms.
There are basically two ways to operate the plasma which are referred to as DC and RF sputtering, respectively, according to the applied bias voltage. For the DC mode the required setup is more simple, but it only works with conducting sputter materials. On the other hand, RF sputtering is typically used to avoid charge build-up on insulating targets. For this the sign of the bias is varied at rates of radio frequency ($\sim$ 10 MHz). For the sample fabrication in the framework of this thesis, DC sputtering was applied in a pulsed mode, that means the power is applied in short pulses with a frequency of typically

250 kHz and a pulse width of 1600 ns. This yields an additional possibility to control the deposition rate and to allow the usage of higher power without causing the target to overheat.
Another advantage of magnetron sputter deposition is the possibility to prepare compound materials. By adding nitrogen (N_2) gas to the Ar into the chamber, a so-called reactive sputter deposition process can be used to prepare compounds. For example, sputtered Nb atoms chemically react with the N_2 and are finally deposited as niobium nitride (NbN). For this, the relative pressures of inert and reactive gases determine the composition and thus the properties of the NbN and have to be adjusted respectively. However, since this offers more options to control the process, sputtering is the most suitable technique for NbN deposition, compared to CVD or thermal diffusion [111], for example.
Altogether, magnetron sputter deposition is a very valuable tool for the preparation of thin films consisting of various materials. An important advantage is the high kinetic energy of the deposited target atoms [112] which yields a

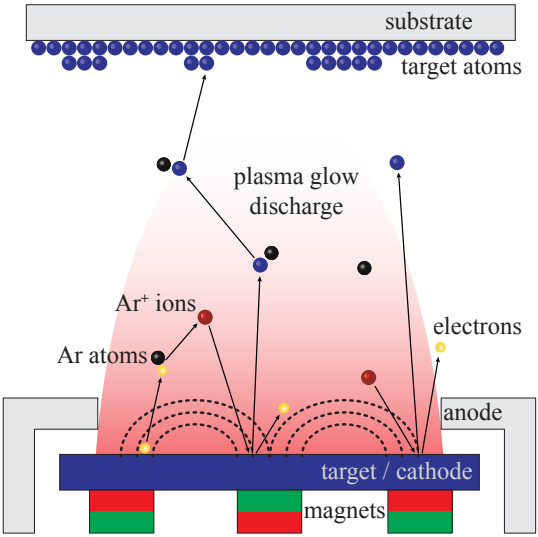

Figure 3.4.: Basic principle of magnetron sputter deposition. The target is bombarded by ionized Ar^+ causing the release of atoms which form thin layers on the substrate. Ar^+ ions and electrons form a plasma near the target that is driven by an electric field between cathode and anode and that is trapped by a magnetic field to increase the efficiency. Keeping the plasma pressure low increases the mean free path of the sputtered atoms and thus the deposition rate.

better adhesion to the substrate compared to thermal evaporation deposition methods, for example. Furthermore, sputtering is a 'cold' deposition technique generating small heat loads onto the sample. This is important for the deposition of materials with high melting/evaporation points. All samples presented in this thesis with superconducting contacts are prepared by sputter deposition (Re, NbN) or co-sputtering (ReW) operating two magnetrons in parallel.

3.5. Electrical measurement setup

After the first tests for electrical functionality at room temperature at the needle probing station (see Ch. 3.3), the samples are finally cooled down and investigated at cryogenic temperatures in the sub-Kelvin regime. This is crucial, because the investigation of QDs requires the thermal energy $E_{\mathrm{th}} = k_{\mathrm{B}}T = 8.6 \cdot 10^{-5}$ eV/K to be smaller than the involved energy scales introduced in Ch. 2.2 which are of the order of $0.1 - 1.0$ meV.
Three different systems are available to reach temperatures from 1.5 K down to 23 mK, which all make use of the effective cooling of liquid helium (LHe) that is pumped on and evaporated. The systems differ mainly in the type of LHe they use. By pumping on ^{4}He down to a gas pressure in the mbar regime it is possible to reach $T \approx 1.5$ K in the ^{4}He-cryostat. Heating and regulation allows for tuning and stabilization of T up to room temperature by using a so-called variable temperature insert (VTI). This is useful for T-dependent measurements. The ^{3}He-cryostat is based on the evaporation of ^{3}He in a closed reservoir which consists of a piece of charcoal, or the sorb, and the 1K-pot. A ^{4}He-cryostat system is used together with the 1K pot to cool and liquefy the ^{3}He which is subsequently pumped on and evaporated by the sorb. Since ^{3}He has a lower boiling point than ^{4}He, temperatures of $T = 230$ mK can be reached for as long as three days. After all ^{3}He is evaporated, it has to be re-condensed by heating the sorb to release the gas, and a new cooling cycle can be started. Even lower temperatures can be reached in the ^{4}He/^{3}He dilution refrigerator by taking advantage of the component's characteristic phase separation at low temperatures into a concentrated ^{3}He-rich and a mixed phase. Pumping on the latter leads to evaporation of only ^{3}He, due to its lower boiling point, and to a transfer of ^{3}He from the concentrated to the mixed phase, since the ratio of the ^{4}He/^{3}He has to be constant. This transport needs a significant amount of latent heat, similar to that of an evaporation process. This is provided by the system which can be cooled down to $T = 23$ mK. However, for $T < 1$ K the phonon temperature T_{ph} and the effective electron temperature T_{el} of a system start to decouple. This typically results in a much higher T_{el} compared to the actual base temperature since the electronic system can be heated through

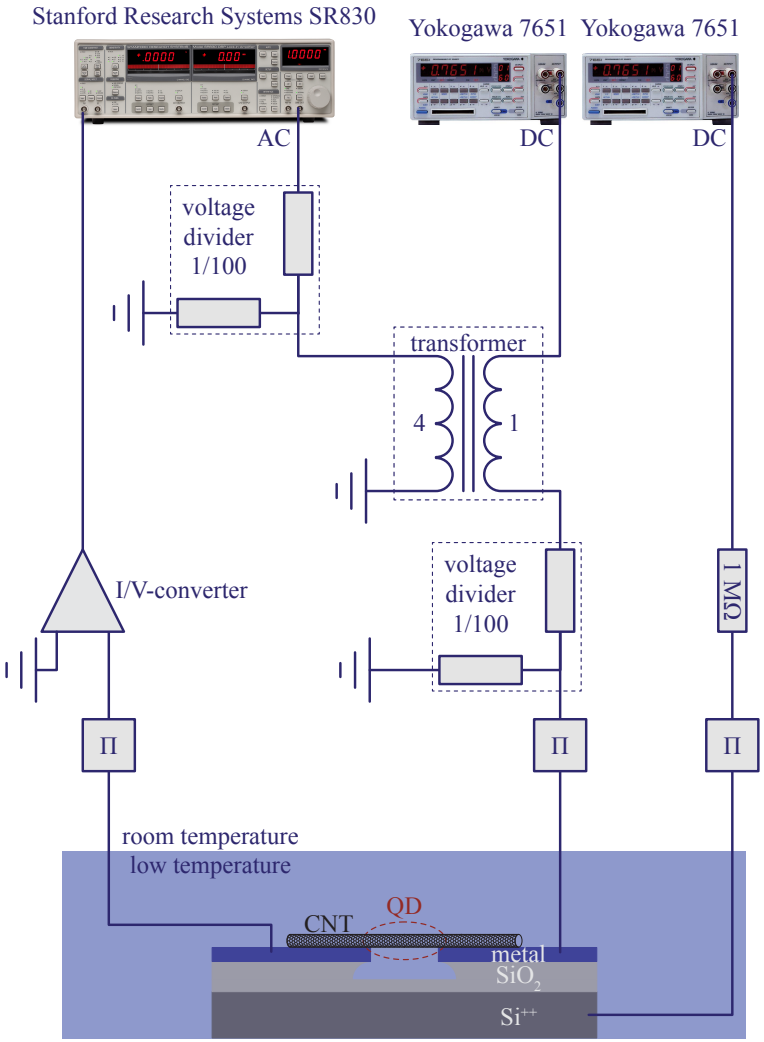

Figure 3.5.: Electrical measurement setup used to apply the superimposition of V_{ac} from the lock-in amplifier *SR830* and of V_{dc} from a *Yokogawa 7651* to the source contact of the sample. The voltage drop over the device yields a current that is converted to a voltage signal and amplified by an in-house built IV-converter with gains in the range of $10^6 - 10^9$ V/A. The *SR830* detects the resulting signal by the lock-in technique. While the sample is cooled to cryogenic temperatures, the setup is at room temperature.

the connecting cables from the environment. This requires good filtering and shielding of electromagnetic radiation to prevent them from penetrating down to the sample and heating the system.
At cryogenic temperatures, a QD can form on the CNT between the two contacts. Its characterization is typically done with the setup that is shown in Fig. 3.5 by means of the lock-in technique using the lock-in amplifier model *SR830* of *Stanford Research Systems* to apply an AC-excitation voltage Vac to the source contact. The resulting voltage drop over the sample leads to a current through the device that is amplified and converted by an in-house built IV-converter to a voltage signal that can be detected again by the *SR830*. As introduced in chapter 2.2, there are basically two possibilities to tune the investigated QD: a global DC back-gate voltage V_{bg} and a DC source-drain bias V_{sd}. The former is applied to the Si^{++} substrate while a safety resistor of at least 1 MΩ prevents a high voltage drop over the device in case there is a small electric leak from the substrate to one of the contacts. In order to add a finite bias voltage to source, it has to be superimposed with the AC excitation which is done by a transformer. Voltage dividers are used to reduce the applied voltages. The DC voltages are supplied by two *Yokogawa 7651* sources. In order to prevent RF-noise from penetrating through the measurement lines to the sample and causing noise and heating, a filtering system is installed consisting of high-frequency filters at low temperature and Π-filters at room temperature. Finally, computer based *Labview* software is used to control and read-out the measured data via a GPIB bus.

4

Superconducting materials suitable for as-grown carbon nanotube devices

The CVD process includes high temperatures in combination with a H_2-rich atmosphere. This limits the choice of contact materials for the as-grown fabrication scheme enormously, since they have to survive this CVD process unaltered and that is why first results on such devices have been achieved only on Pt electrodes which is a very noble metal with a high melting point. A typical superconductor used as contact for conventionally fabricated CNTs is Ti/Al since it yields a robust proximity effect. However, it cannot be used for as-grown devices, since it would simply melt during CVD. Therefore, alternative superconductors have to be considered as contacts to as-grown CNTs.

The periodic table in Fig. 4.1 gives an overview of almost all known elemental superconductors and their respective critical temperatures T_c [113]. All of them are of type I, except the type II superconductors vanadium (V), niobium (Nb), and technetium (Tc). Most of them can be excluded for obvious reasons: first, their melting point is lower than the reactor temperature and second, their T_c is too small and experimentally not within reach. Some of them drop out because they are radioactive. Others, such as tantalum (Ta) and Nb, both form insulating hydrides during CVD. This leaves only rhenium (Re) as possible elemental superconductor. Alternatively, there are potential compound superconductors like niobium nitride (NbN) that exhibits both, a very high melting point and a high T_c. In the following, an introduction is given to the material properties of elemental Re, its alloy with tungsten (W), and NbN. They are characterized and their suitability for the as-grown fabrication scheme is discussed.

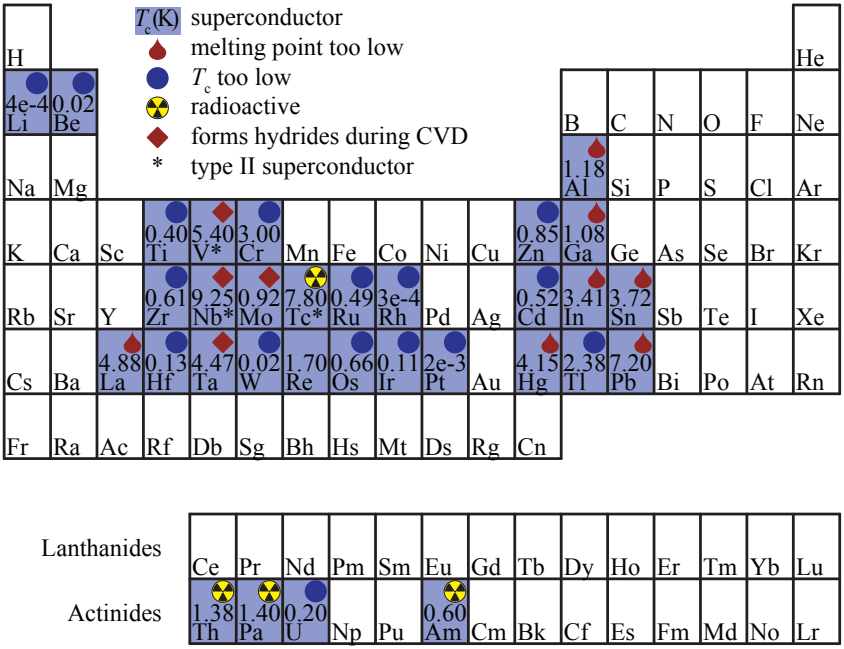

Figure 4.1.: Periodic table combined with an overview of almost all the elemental superconductors, their respective critical temperature T_c, and the material properties that exclude them from suitability for the CVD process and thus, from the preparation of as-grown CNT devices (adapted from Ref. [113]).

4.1. Rhenium

Rhenium has a very high melting point at $T_{m,Re} = 3453$ °C [114] and can be prepared as single-crystal thin films by sputtering onto a heated sapphire substrate [115]. These films exhibit a superconducting transition temperature in the range of $T_{c,Re} = 1.70 - 2.42$ K [116, 117]. The work function is important for the properties of the interface to a CNT and has been determined to $\phi_{Re} = 5.1$ eV [118] and is in the range of the CNT work function $\phi_{CNT} = 4.9 \pm 0.1$ eV [94] (see Ch. 2.5.1). Tunneling measurements on single-crystal Re show a superconducting gap of $2\Delta_{0,Re} = 0.5$ meV [119, 120]. Furthermore, Re has important properties for the fabrication process, as it is resistant to hydrofluoric acid [114]; hence it can be used as an etching mask for the preparation of trenches in the SiO_2 layer between the electrodes, as described in Ch. 3.

The Re thin films prepared in the framework of this thesis are tested in the form of narrow strips of 6 µm width and 50 nm thickness by measuring their resistance R in a four-terminal setup as a function of temperature T and external magnetic field B (see Fig. 4.2). For $T < T_c$ the material is in its superconducting state, thus the resistance drops to a non-measurable small value. Since this measurement is done after CVD, Re is shown to preserve its superconducting properties and yields $T_{c,Re} \approx 2.1$ K, determined at 50 % of the normal state resistivity. Thus, it can be used as contact material for as-grown CNT devices. The superconducting properties of all materials prepared in this thesis are characterized that way. To determine $H_{c,Re}$, a magnetic field is applied in both, parallel and perpendicular orientation to the plane of the test-strip, in order to drive the structure to the normal state. The resulting values $\mu_0 H_{c,Re,||} \approx 0.67$ T and $\mu_0 H_{c,Re,\perp} \approx 0.25$ T, where μ_0 is the vacuum permeability, make it possible to suppress the superconductivity in the leads already at low B. This can be used to tune the leads between the superconducting and the normal state without increasing the temperature of the sample.
Altogether, Re is a promising candidate as superconducting contact material for as-grown CNT devices. It can be prepared as thin film by magnetron sputter deposition (see Appx. A for detailed process parameters) and survives the CVD

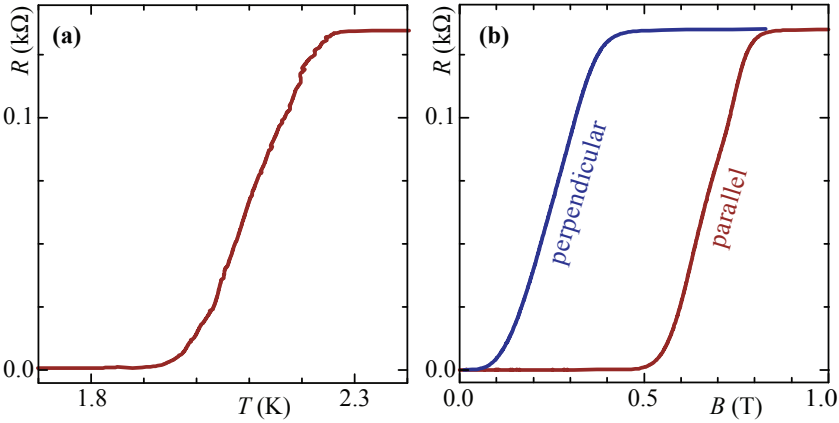

Figure 4.2.: Measured superconducting transitions of a Re test-strip of 6 µm width and 50 nm thickness. The resistance as a function of temperature **(a)** and external magnetic field **(b)** first yield the critical value $T_{c,Re} \approx 2.1$ K, determined at 50 % of the normal state resistivity. B is applied both, parallel and perpendicular with respect to the plane of the Re film and results in transitions at $\mu_0 H_{c,Re,||} \approx 0.67$ T and $\mu_0 H_{c,Re,\perp} \approx 0.25$ T, respectively.

process unaltered in its superconducting properties. Recently, experimental results were published that show signatures of the superconducting gap in as-grown CNT devices with Re [121, 122] and Re/Molybdenum contacts [123].

4.2. Rhenium in combination with tungsten

As presented in Ch. 2.5.3, a good chemical contact between CNT and metal is supposed to yield a good electrical coupling as well. This suggests to look for materials that form strong chemical bonds to CNTs, which has been done in the work of M. S. Wang *et al.* [124] who have experimentally investigated the mechanical robustness and reliability in combination with electrical conductance on contacts between multi-walled CNTs and carbide/tungsten wires. All shells of the CNT have been soldered directly to the surface of a W wire which resulted in junctions of extremely high tensile strength and very low resistances at the same time.
This effect can be made use of by adding a thin W contact layer on top of the basic Re electrodes described in the last section (Ch. 4.1), in order to achieve better contact to the CNT. The superconducting properties are rather improved, in the sense that Re/W double layer systems show a larger critical temperature of $T_{c,Re/W} \approx 2.5$ K compared to bare Re, as it is depicted in the measurement of Fig. 4.3 (a). Furthermore, W offers the possibility to

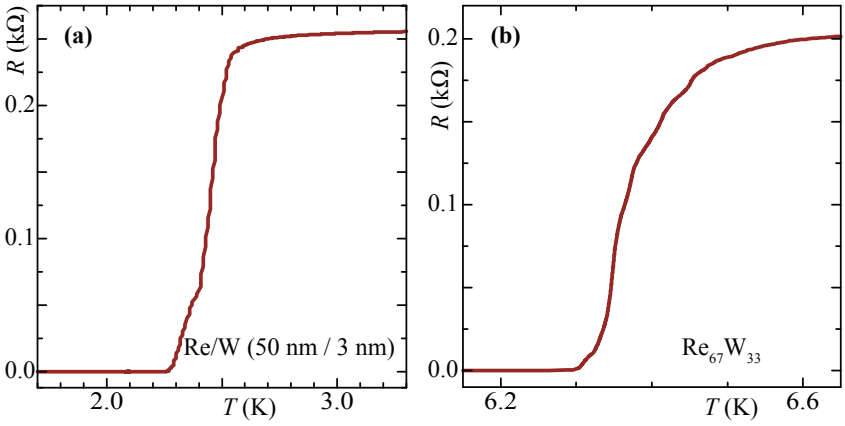

Figure 4.3.: Superconducting transitions of a **(a)** Re/W (50 nm / 3 nm) double layer system and a **(b)** $Re_{67}W_{33}$ alloy test-strip of 6 µm width and 50 nm thickness. The resistances as a function of temperature yields the critical values $T_{c,Re/W} \approx 2.5$ K and $T_{c,Re_{67}/W_{33}} \approx 6.4$ K, respectively, determined at 50 % of the normal state resistance.

create superconductors of even larger transition temperatures, if it is alloyed to Re. This has been shown by D. S. Easton *et al.* who have used different compositions of $3.5-95$ at.% of Re and have grown an alloy single crystal with the largest superconducting transition temperature of 11.4 K [125]. As a big advantage, such an alloy can be fabricated by simply co-evaporating the two materials which makes it also easy to change its composition. Interestingly, these alloys have different superconducting properties depending on their composition. That means it is possible to tune T_c by changing the amount of W in the fabrication process. Finally, the resulting polycrystalline Re/W alloys have an increased critical temperature compared to pure Re that can be tuned between $T_\mathrm{c} = 3.2$ K for $\mathrm{Re_{50}W_{50}}$ and $T_\mathrm{c} = 6.8$ K for $\mathrm{Re_{70}W_{30}}$ [126].
A $\mathrm{Re_{67}W_{33}}$ alloy that was prepared by magnetron co-sputtering yields a transition at $T_{\mathrm{c,Re_{67}/W_{33}}} \approx 6.35$ K, as it is shown in Fig. 4.3 (b), which makes this material system a promising candidate as superconducting contact material to CNTs. Furthermore, it has already shown superconducting proximity effect in graphene junctions connected to ReW [127].

4.3. Niobium nitride

Niobium has a melting point temperature of $T_\mathrm{m,Nb} = 2468$ °C and a critical temperature of $T_\mathrm{c,Nb} = 9.13$ K [114] which makes it an additional promising candidate as contact material for as-grown CNT devices. It turns out however, that the CVD process leads to the formation of insulating Nb hydrides. On the other hand, Nb can be used as basis for the compound niobium nitride (NbN) which is not altered by the CVD process and has an even higher $T_\mathrm{c,NbN} = 9.5 - 15.7$ K [111, 112, 114, 128]. Experiments on reactive magnetron sputter deposited NbN films have shown that their crystal structure depends on the kind of substrate and its temperature during film growth, but even polycrystalline films grown at room temperature can have a high critical temperature of $T_\mathrm{c,NbN} = 15.7$ K [112].
The superconducting gap of NbN has already been measured at $T = 4.2$ K on a NbN/AlN/Nb tunnel junction to $\Delta_\mathrm{0,NbN} \approx 2.6$ meV [111] for a device with a critical temperature of $T_\mathrm{c,NbN} = 14.5$ K. As a consequence, the superconducting zero temperature coherence length of NbN is $\xi \approx 7$ nm [129]. It has been calculated from the measured temperature dependence of the upper critical magnetic field H_c2 using the Ginzburg-Landau relationship

$$-\frac{\mathrm{d}H_\mathrm{c2}}{\mathrm{d}T}\bigg|_{\mathrm{T_c}} = \beta_{\mathrm{H_{c2}}}(T_\mathrm{c})\,\frac{\hbar c}{2e}\frac{1}{\xi_0^2(0)}\frac{1}{T_\mathrm{c}} \tag{4.1}$$

with the measured gradient $\mathrm{d}H_\mathrm{c2}/\mathrm{d}T = -0.49$ T/K and a strong-coupling correction for H_c2 that is given by $\beta_{\mathrm{H_{c2}}}(T_\mathrm{c}) = 1.14$ and can be estimated from T_c and Δ_0 data [129].

Since NbN is a type II superconductor, it will allow some external magnetic field to penetrate into its bulk forming magnetic vortices above the lower critical magnetic field H_{c1}. Therefore, the material is still superconducting, showing a mixed state behavior until the upper critical magnetic field H_{c2} is reached. Typically, H_{c2} is much larger than the critical field H_c of type I materials. The value H_{c2} for NbN exceeds the maximum fields of the available superconducting magnets for this thesis by far, which is in the range of $3 - 9$ T, depending on the cryostat system. Hence, the superconducting transition in an external magnetic field is measured for various temperatures slightly below T_c, as shown in Fig. 4.4 (a). The temperature dependence of H_{c2} can be approximated by the parabolic law

$$H_c(T) = H_c(0)\left(1 - \left(\frac{T}{T_c}\right)^2\right) \tag{4.2}$$

and a corresponding fit of the measured data points yields an estimate for the upper critical field of $\mu_0 H_{c2,NbN}(0) \approx 30$ T. The work function of NbN has been reported as $\phi_{NbN} = 4.01$ eV [114]. Experiments on a NbN/NbN tunnel junctions with an amorphous magnesium oxide tunnel barrier have revealed a large superconducting gap of $\Delta_{0,NbN} = 5.1$ meV [130]. Altogether, the superconducting properties and the fact that NbN survives the CVD process make it

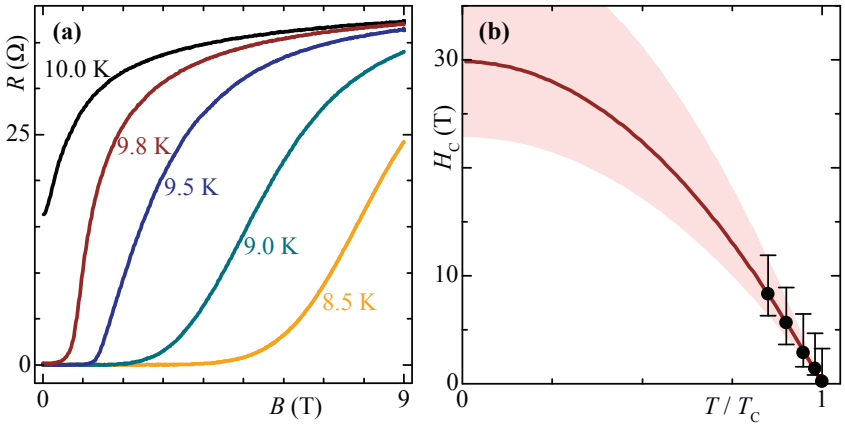

Figure 4.4.: (a) Measured superconducting transitions of a thin NbN test-strip as a function of a external magnetic field applied parallel to the film plane at various temperatures close to $T_{c,NbN} \approx 10.0$ K. **(b)** The upper critical magnetic field H_{c2} can be estimated by fitting the data points, determined at 50 % of the normal state resistivity, to the parabolic law of Eq. (4.2). The sketched error region is estimated via the error bars which are estimated from the different transition widths in (a).

a promising candidate for contact material to as-grown CNT devices, affirmed by the fact that superconducting proximity effect has already been observed in a network of CNTs between NbN electrodes [131].

Summary

Table 4.1 gives an overview on the measured material properties of the different superconducting metals that are used in this thesis to contact as-grown CNTs. Their critical temperatures T_c and critical magnetic fields $\mu_0 H_{c2}$ parallel to the electrode surface are determined after the CVD process by resistance measurements on a test-strip of ≈ 50 nm thickness and 6 µm width, respectively.
All mentioned materials have been used as contacts to as-grown CNT devices except rhenium/molybdenum (Re/Mo) alloys. While bare Nb forms hydrides during the CVD and becomes insulating, NbN survives this process unaltered in its superconducting properties. However, at cryogenic temperatures, large barriers are arising and yield an exponentially increased resistance of the device. It is supposed to be caused by the mismatch of the work functions of NbN (4.0 eV) and CNTs (4.9 eV), respectively and therefore, a thin Pt contact layer is added on top of the NbN. Its much larger work function $\phi_{\mathrm{Pt}} = 6.13$ eV [132] is supposed to balance the initial mismatch. Finally, this leads to very low-Ohmic devices even at cryogenic temperatures. The results on the measurements of QD systems are presented in Chs. 5-8.

Table 4.1.: Superconducting properties of the different metals used as contact material to as-grown CNTs.

metal	T_c (K)	$\mu_0 H_{c2}$ (T)	comments
Re	2.1	0.67	-
Re+W	2.5	0.5	W contact layer (3 nm)
Re/W	6.3	-	alloy - T_c tunable
Nb	-	-	forms hydrides - insulating
NbN+Pt	10.0	≈ 30	Pt contact layer (3 nm)
Re/Mo	5.2	3.2	alloy

5

Superconducting proximity effect in a conventional carbon nanotube device

In this chapter, QD measurements on the conventionally fabricated, non-suspended CNT **Device A1** with superconducting Re contacts are presented. The sample preparation is described in Ch. 3.1 and before the cool-down, the device was checked at room temperature for functionality. The measurements of the conductance G as a function of back-gate voltage V_{bg} through the CNT yield a metallic CNT that is very well coupled to the leads, as it is indicated by the high maximum conductance of $G_{\mathrm{RT}} = 0.84e^2/h$, which is equivalent to a resistivity of $R_{\mathrm{RT}} = 31.7\ \mathrm{k}\Omega$. This makes it a promising candidate for measuring some superconducting proximity effect. The low-temperature investigations were done in the ^{3}He-cryostat at $T = 230$ mK, where the resulting stability diagram yields a Coulomb blockade pattern with an additional gap of suppressed conductance around zero-bias due to the superconducting density of states in the leads. This gap is analyzed by fitting the measurements to a model based on a lifetime broadened density of states.

5.1. Characterization at cryogenic temperature

The measurement of $G(V_{\mathrm{bg}})$ at $T = 230$ mK is shown in Fig. 5.1 and yields a series of Coulomb peaks where each of them represents the addition of a single charge carrier, as it is discussed in Ch. 2.2.1. The maximum conductance at the peak positions drops to $G_{\mathrm{max}} \approx 0.60e^2/h$ compared it the measurement at room temperature. This can be attributed to the presence of a superconducting density of states in the leads, which suppresses G at equilibrium, i.e. $V_{\mathrm{sd}} = 0$. Applying an additional bias voltage leads to a strong increase of G since the superconducting gap is overcome, as it is shown in the stability diagram of

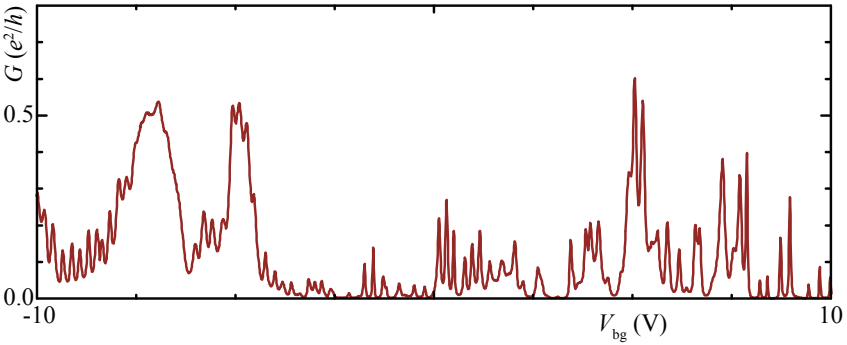

Figure 5.1.: Back-gate sweep of Device A1 measured at $T = 230$ mK. The peak values in conductance of $G \approx 0.60e^2/h$ suggest a good coupling of the leads to the CNT while the irregular positions of the peaks most likely account for the formation of multiple QDs in a bundle or a multi-walled CNT.

Fig. 5.2 (a) which exhibits a transparent device with $G_{\max} \approx 2e^2/h$ at finite bias. The leverarm of the system is determined at the Coulomb diamond that is fully visible around $V_{\rm bg} = -7.62$ V and calculates to $\eta = \Delta V_{\rm sd}/\Delta V_{\rm bg} = 0.008$. Both, the peak positions in Fig. 5.1 and the charge states in Fig. 5.2 (a) occur irregularly and show no sign of the four-fold periodicity expected for a clean CNT QD. This suggests that the device rather consists of a CNT bundle or a multi-walled CNT which would allow for the formation of several QDs in parallel and result in an irregular Coulomb blockade pattern, comparable to the present measurement. Importantly, the transport measurements yield a clear gap structure around zero-bias for essentially all gate-voltages. This is interpreted as being induced by the superconducting density of states in the leads and will be discussed in the following.

5.2. Nonlinear transport

In order to confirm the superconducting origin of this gap, an external magnetic field B is applied parallel to the CNT axis while $V_{\rm bg}$ is tuned to the middle of a charge state; then $V_{\rm sd}$ is swept to determine the influence on the gap feature. The result is depicted in Fig. 5.2 (b) and shows that increasing B reduces the depth of the gap by 50 % at $B \approx 0.7$ T and finally leads to a complete suppression for $B \approx 0.8$ T (see Fig. 5.2 (c)). These values are in good agreement with the critical magnetic field $H_{\rm c,Re,||}$ of Re test-strips in parallel magnetic field configuration (see Fig. 4.2 (b)). The detailed structure of the gap is depicted in the $G(V_{\rm sd})$ plot of Fig. 5.3. It becomes clear that this gap does not

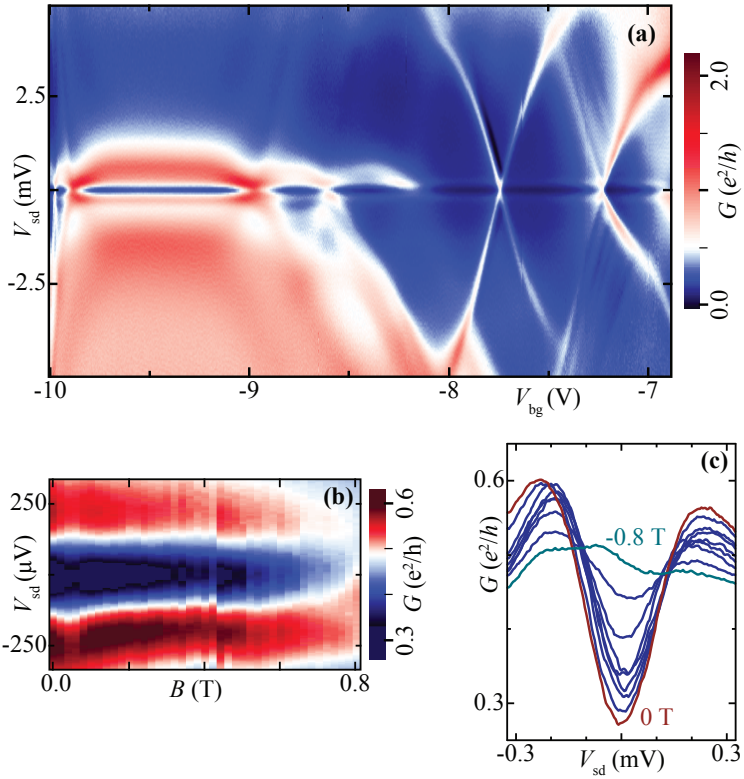

Figure 5.2.: **(a)** Stability diagram of Device A1. A superconducting gap arises around zero-bias. **(b)** Tuning the back-gate to the middle of a state and applying a magnetic field parallel to the CNT axis suppresses the superconducting gap to ≈ 50 % at $B \approx 0.7$ T and to 100 % at $B \approx 0.8$ T which is in good agreement with the critical magnetic field $H_{c,\mathrm{Re},||}$ of the Re contacts. **(c)** Line plots of (b) in steps of 0.1 T.

reach zero conductance and additionally its edges are smeared, which is not the case for Re contacts to graphene [133], for example. This effect is interpreted as being due to a finite lifetime broadening, as it is introduced in Ch. 2.3.2. The corresponding parameters can be extracted by fitting the measured gap structure by means of Eqs. (2.11) & (2.12). It yields the superconducting gap width to $\Delta = 100$ μeV and the lifetime broadening term to $\gamma = 60$ μeV.

In conclusion, using the conventional method to post-fabricate the contacts on top of the CNT makes it possible to observe the superconducting proximity effect in a CNT QD with Re contacts. A smeared superconducting gap is

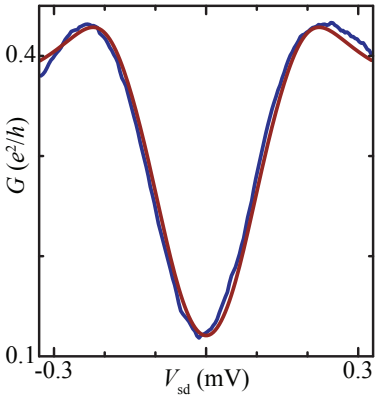

Figure 5.3: The conductance as a function of bias voltage (blue curve) measured at $B_{\text{ext}} = 0$ exhibits the superconducting gap in combination with a finite lifetime broadening. The fit to the tunnel current (red curve) of Eq. (2.11), using Dynes of Eq. (2.12) as model for the density of states in the contacts, results in the fit parameters for the superconducting gap width $\Delta_{0,\text{Re}} = 100$ μeV and the lifetime broadening term $\gamma = 60$ μeV. The measured data from Fig. 5.2 (c) was prepared by adjusting an offset in G and compensating a linear background.

observed due to lifetime broadening effects, but the size of the gap can still be obtained by a fit according to the Dynes density of states. The result $\Delta_{0,\text{Re}} = 100$ μeV is about 150 % smaller compared to the gap width determined on a Re tunnel junction (see Ch. 4.1) and since the broadening of the gap is more distinct than in other superconductors, like for example Al [14], it is more difficult to do spectroscopy measurements on CNT devices with Re contacts. Reasons for the broadened gap could be disorder at the Re-CNT contacts or a dirty interface, possibly caused by PMMA residues after EBL, for example. In order to minimize contamination, the contact areas of the CNTs are cleaned by a H_2 plasma right before depositing the contacts. The optimization of this cleaning process is quite delicate, in order to get rid of all PMMA residues without damaging the CNT itself. Finite temperature can be excluded as source of the broadened gap, because the measurement was done at $T = 230$ mK, well below $T_{\text{c,Re}}$ and a regime where, according to Fig. 2.16 (b), the gap width should hardly be affected by temperature. Polycrystalline Re is another possible reason reason, since different crystallites with different T_{c} and/or coupling to the CNT could cause a smearing of the superconducting gap. Nevertheless, it should be possible to measure some supercurrent through CNT devices with Re contacts.

6

Back-gate and magnetic field dependent inelastic cotunneling thresholds

In this chapter, conductance measurements on the as-grown CNT **Device C1** with Re/W (50 nm / 3 nm) double layer contacts are presented that are prepared by successive deposition in the *ESCA3* sputter machine and measured at $T = 23$ mK in the dilution refrigerator. The stability diagram of the resulting QD shows, in addition to Coulomb blockade, sequential tunneling lines that appear parallel to the diamond edges. They are characterized in the first section. Furthermore, inelastic cotunneling thresholds occur within the Coulomb diamonds and are presented in the second section. Remarkably, they show the unusual effect of a back-gate dependence that also varies for applied external magnetic fields of different strength.

6.1. Stability diagram and quantum dot characterization

The resistance at room temperature indicates a strong electrical coupling of the CNT to the contacts and is listed in Tab. 6.1 together with further characteristic attributes of Device C1. It is identified via the $G_{\mathrm{RT}}(V_{\mathrm{bg}})$ measurement as a non-semiconducting CNT, since it does not show any back-gate dependence. Consequently, the device probably consists of a single metallic CNT, but it is also possible that several CNTs in parallel are connecting the electrodes. The same kind of $G(V_{\mathrm{bg}})$ measurement at cryogenic temperature results in a pattern of sharp Coulomb peaks and is shown in Fig. 6.1. Again, the large conductance value at the peak positions indicates a good coupling of the CNT to the leads. The stability diagram is shown in in Fig. 6.2 (a) (and in Fig. 2.10) and yields a clear Coulomb blockade pattern including both, sequential tunneling lines and

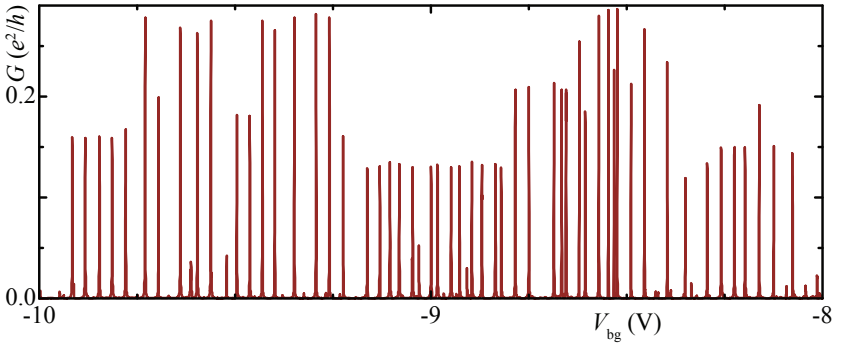

Figure 6.1.: Back-gate sweep on Device C1 measured at $T = 23$ mK. The peak values in conductance of $G \approx 0.27e^2/h$ suggest a good coupling of the leads to the CNT while the irregular peak positions account for a disordered device.

Table 6.1.: Characteristic properties of Device C1

G_{RT}	$0.83e^2/h$
R_{RT}	31 kΩ
η	0.42
L_{QD}	9.5 µm
C_{s}	57.0 aF
C_{d}	57.0 aF
C_{bg}	4.5 aF
C_{Σ}	118.5 aF
E_{add}	1.4 meV
δE	0.35 meV
U_{C}	1.05 meV

inelastic cotunneling thresholds. The greyscale plot is given in a logarithmic scale of $G/(e^2/h)$ in order to visualize both features in the same plot. According to the introduction of Ch. 2.2, the system's capacitances are determined and listed together with some further characteristic properties in Tab. 6.1. The length of the QD is calculated via Eq. (2.5) to $L_{\mathrm{QD}} = 9.5$ µm and is much larger than the electrode gap of the structure, which has a width of ~ 700 nm. Therefore, it is suggested that the CNT that carries the QD is not grown straight over the trench but rather on an indirect way, which was confirmed by SEM imaging after the electrical measurements. Furthermore, it revealed that several CNTs were connecting the electrodes and that some of them grew around the electrode gap. Hence, they were not suspended but lying over large lengths on the substrate.

6.2. Gate-dependent inelastic cotunneling thresholds

The stability diagram of Fig. 6.2 (a) depicts some inelastic cotunneling thresholds that run parallel to the gate-axis and basically represent the expected result according to their introduction in Ch. 2.2.2. However, applying an external magnetic field B in-plane of the electrode structures has a large influence

on the gate-dependence of these ICTs and leads to a tilt within each single Coulomb diamond. This is shown in the measurement of Fig. 6.2 (b) where $B = 3$ T results in negative slopes of the ICTs. If the field is increased further to $B = 4$ T, the slope of the thresholds changes sign and becomes positive, as it is shown in Fig. 6.2 (c). Accoding to the descriptions in Ch. 2.2.3, the gate-dependence of the ICTs can be explained by renormalization effects that are induced by different tunnel couplings of two QD orbitals to the leads. K. Grove-Rasmussen *et al.* [46] have reported this feature and concluded that these tunnel couplings are affected by magnetic fields. Thus, the effect of tilted ICTs can vanish for finite fields. However, this is in contrast to the present measurements, where this feature does not occur unless magnetic fields are applied.
According to the work of J. V. Holm *et al.* [45], the tilted threshold should only appear within the first two Coulomb diamonds of a four-electron shell on the QD. Only then it would be possible for the different tunnel couplings of two doublets to affect the level spacing and thus cause a tilt of the ICTs. This is not the case here, since it is not possible to identify any electron shell. Reasons for this are first, that no clear four-fold degenerate shell structure is observable in the stability diagram, and second, that the orientations of the tilts are the same for every Coulomb diamond, which is in contrast to the measurements of Ref. [45]. However, the mechanism discussed in Ch. 2.2.3 can still basically explain the presence of the observed tilts: but if more than two doublets are considered with different couplings to the leads and with different energy spacings, the situation becomes much more complicated and can not be modeled any more. In this device it is most likely the case, that the gate-dependence of the ICTs can be attributed to the different coupling of several distinct energy levels to the leads. The fact that the tilt of the thresholds changes with magnetic fields accounts for a dependence of these couplings on magnetic field.
Unfortunately, this device was electrically quite unstable and many gate-jumps occurred during the measurements randomly in time. Therefore, it was not possible to measure the magnetic field dependence on a single V_{sd} sweep that cuts one specific ICT and thus would allow to investigate its behavior as a function of magnetic fields. The reason for this can most probably be found in the fact that this device had several CNTs connecting the two elec-

Figure 6.2. ***(facing page)*:** Stability diagrams of Device C1 measured at $T = 23$ mK for different external magnetic fields. **(a)** At zero field, a Coulomb blockade diamond pattern is observable that exhibits both, excited state lines of increased conductance running parallel to the diamond edges and inelastic cotunneling thresholds within the diamonds. **(b)** Applying a magnetic field of $B = 3$ T leads to a finite tilt, i.e. a back-gate dependence of the cotunneling thresholds appearing in all diamonds. **(c)** The slope of the tilt changes if the magnetic field is increased to $B = 4$ T.

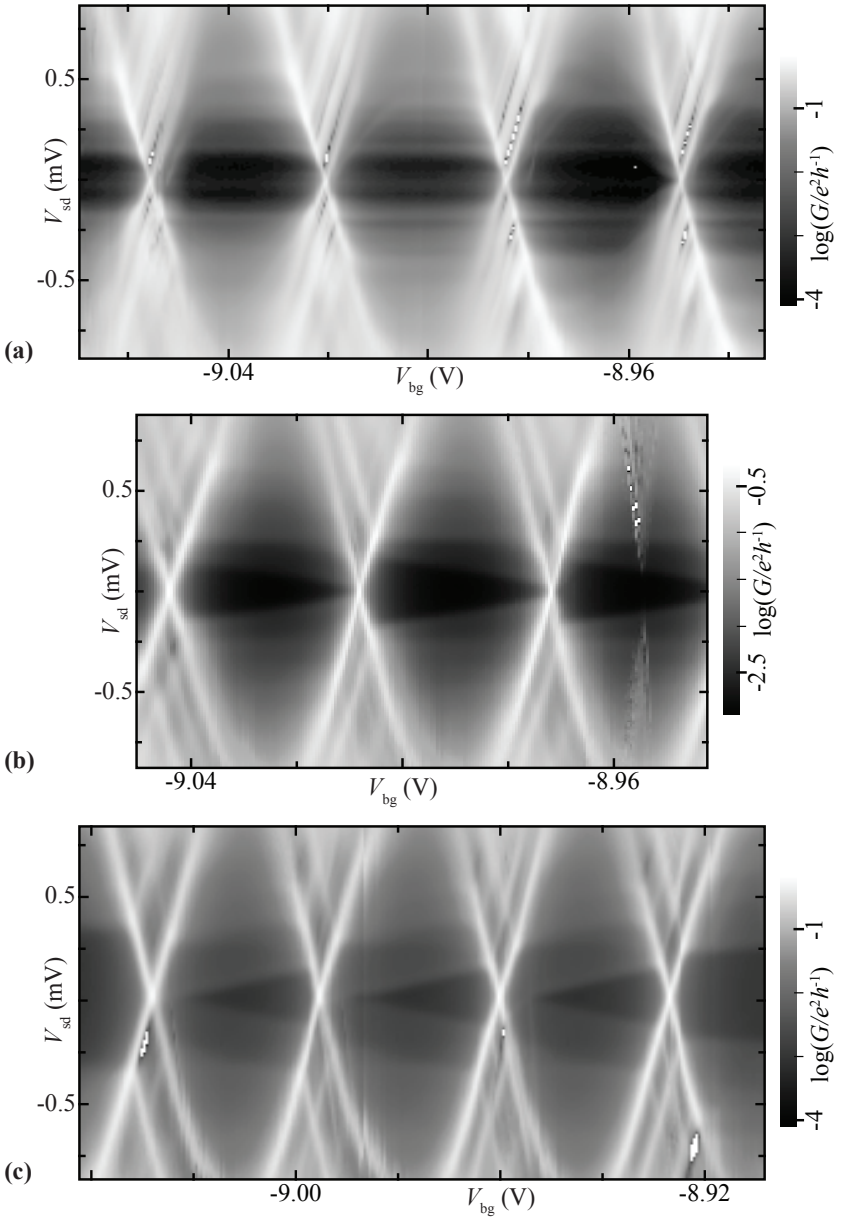
(a)
0.5
-0.5
V_{sd} (mV)
-9.04
V_{bg} (V)
-8.96
-1
-4
$\log(G/e^2h^{-1})$
(b)
0.5
-0.5
V_{sd} (mV)
-9.04
V_{bg} (V)
-8.96
-0.5
-2.5
$\log(G/e^2h^{-1})$
(c)
0.5
-0.5
V_{sd} (mV)
-9.00
V_{bg} (V)
-8.92
-1
-4
$\log(G/e^2h^{-1})$

trodes, as it was revealed by SEM imaging after the cryogenic measurements. One of these CNTs had a length roughly consistent with the estimate of $L_{\mathrm{CNT}} = 9.5$ µm from the previous section. Furthermore, the present device did not show any superconducting proximity effect. Even the deposition of an additional thin W contact layer, that was supposed to form strong covalent bonds to CNTs at the high temperature CVD process (see Ch. 4.2)), did not lead to any improvements. One reason might be that it turned out to be extremely difficult to wire-bond onto the Re-W bonding pads of the devices. The high ultrasonic power and force that was needed destroyed a lot of devices, especially the low-ohmic ones. The exact source of this problem is still unclear, in particular if it has something to do with the Re itself. Therefore, alternative superconductors have to be taken into account and the following results were obtained on NbN contacts.

7

Vibrational excitations in a carbon nanotube quantum dot

In this chapter nonlinear conductance measurements on two as-grown CNT devices with NbN/Pt contacts are presented. They were prepared in the *ESCA3* sputter machine (see Appx. A for detailed parameters) and investigated in the ^{3}He-cryostat at $T = 230$ mK. The clean transport characteristics of the samples allow for the observation of very stable Coulomb blockade patterns over a large range of back-gate voltage. Additionally, one device exhibits a parallel double quantum dot system that is formed in a bundle of CNTs with the two involved QDs electrostatically coupled to each other. Furthermore, tunneling electrons are exciting longitudinal vibrations on a suspended part of the CNT that result in a series of excited state lines with some of them accompanied by negative differential conductance.

7.1. As-grown carbon nanotube devices with NbN electrodes

The electron micrograph of Fig. 7.1 shows **Device C2**: a single, as-grown CNT that is grown over the electrode gap; not in a straight and direct way, but rather bent. Electrical characterization at room temperature yields a well-coupled small band-gap CNT of quite high conductance. Cooling it to cryogenic temperatures leads to the formation of a QD whose characteristic parameters are determined and listed in Tab. 7.1. The corresponding charge stability diagram exhibits a clear and stable Coulomb blockade pattern, as shown in Fig. 7.2 (a), where each diamond corresponds to an additional charge carrier on the QD. The diamonds are not mirror symmetric with respect to zero bias but exhibit a tilt due to asymmetric electrostatic coupling of the QD to the leads. Furthermore,

there are excited state lines running parallel to the diamond edges that have an equidistant spacing and some of them are accompanied by lines of NDC, especially in the negative bias regime. From the zoomed image in Fig. 7.2 (b) various specific properties of this system are determined: the leverarm η, the capacitive couplings C_{i}, the electronic coupling parameter Γ that is extracted via the FWHM of the Coulomb resonances, or the energy spacing of the excited state lines that is determined via the average peak distance at the charge degeneracy points to $\delta E = 0.78 \pm 0.13$ meV, as it is shown in the exemplary measurement of $G(V_{\mathrm{sd}})$ in Fig 7.2 (c). Equation (2.5), which relates δE to the length of a QD, yields $L_{\mathrm{QD}} = 4.5$ µm for this device. This is much longer than the CNT length of $L_{\mathrm{CNT}} \approx 1.3$ µm between the electrodes determined by SEM imaging. Thus, it is likely that the excited state lines have a different than electronic origin. One possibility is the excitation of phonons by tunneling electrons through the QD, as it is discussed in Ch. 2.4. This would imply a suspended CNT which is obviously not the case here, because the CNT is lying directly on the substrate between the electrodes. However, there are short suspended parts right at the transitions to the electrodes, as it can be seen in Fig. 7.1. For an estimation, the length of the suspended parts is related to the height of the electrode structure, which is given by ~ 60 nm and consequently has to be exceeded. Taking into account the length-dependent energies of the different vibrational modes of a CNT (see Fig. 2.17) and comparing them to the

Table 7.1.: Characteristic properties of Device C2

G_{RT}	$0.26e^2/h$
R_{RT}	100 kΩ
L_{CNT}	1.3 µm
η	0.42
C_{s}	15.2 aF
C_{d}	22.8 aF
C_{bg}	19.4 aF
C_{Σ}	57.4 aF
E_{add}	3.5 meV
Γ	0.3 meV
δE	0.78 meV

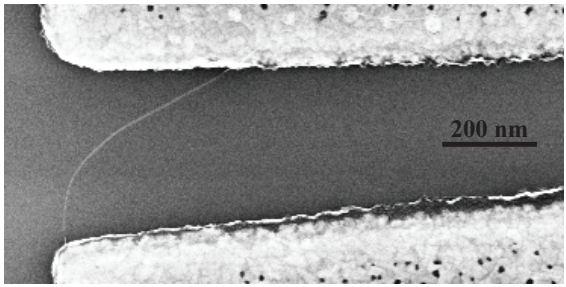

Figure 7.1.: SEM micrograph of the as-grown CNT Device C2 contacted to NbN/Pt (50 nm / 5 nm) electrodes. The total length of the CNT is $L_{\mathrm{CNT}} \approx 1.3$ µm between the contacts where it is not suspended but lying directly on the substrate.

measured values of δE and the length of the suspended parts, one can roughly suggest the excitation of the longitudinal stretching mode for this device. This is affirmed by this vibrational mode exhibiting the largest electron-phonon coupling [5], as introduced in Ch. 2.4. Inserting the level spacing into Eq. (2.14) yields an oscillator length of $L_0 = 140$ nm which is approximately in the range of the suspended parts. Furthermore, lines of NDC parallel to the excited states have already been observed in devices that show tunneling induced excitation of vibrations [29] and suggests that the excited state lines originate not in electronic but rather in vibrational excitations. Besides a good agreement

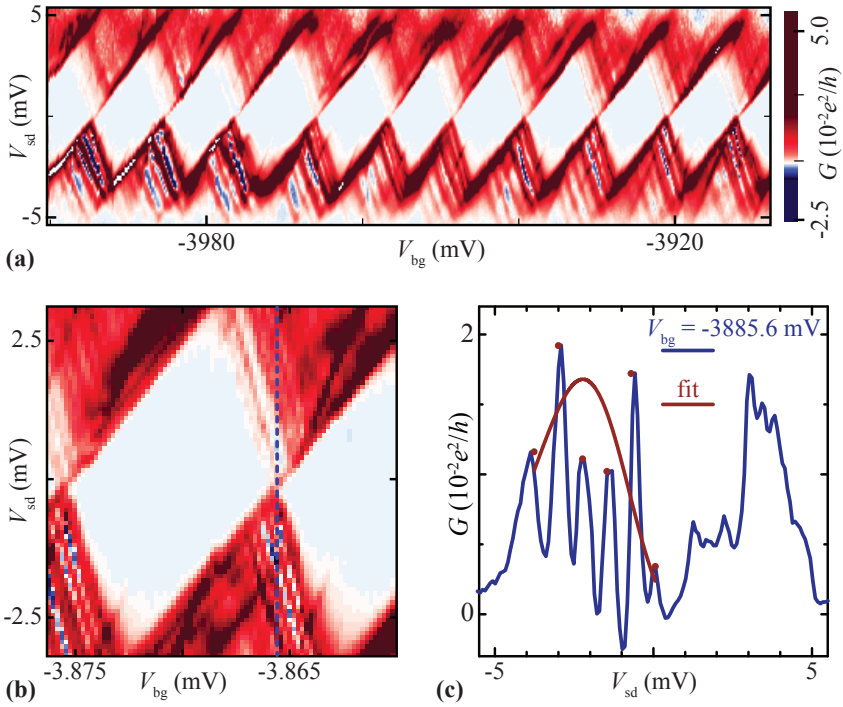

Figure 7.2.: (a) Stability diagram measured at $T = 230$ mK of Device C2 showing stable Coulomb blockade, additional excited state lines, and indications of negative differential conductance (blue regions). **(b)** Zoom and exemplary cut position through a charge degeneracy point. **(c)** The $G(V_{sd})$ sweep at $V_{bg} = -3885.6$ mV exhibits the average level spacing of the excited state lines to $\delta E = 0.78 \pm 0.13$ meV. The suppression of conductance in the low-bias regime is due to Franck-Condon blockade. Fitting the peak positions identified as vibrational quantum number ν to Eq. 2.18 results in the electron-phonon coupling constant $g = 3.5 \pm 0.6$.

of the energy terms, a further indication for vibrational excitations is given by the suppressed conductance in the low-bias regime at the charge degeneracy points, which can be seen in the exemplary V_{sd} sweep of Fig 7.2 (c), where the resonance at zero bias is much weaker than the equidistant ones that occur at increased V_{sd}. This effect is known as Franck-Condon blockade and has already been observed on vibrating CNT QDs [29]. It accounts for a large electron-phonon coupling constant g and is described in Ch. 2.4.3. Assigning the peak positions to vibrational quantum number ν and fitting their heights $G_{\nu}^{\max}$ to Eq. 2.18, results in $g = 3.5 \pm 0.6$ (see Fig. 7.2 (b)). Since $g > 1$, it accounts for strong electron-phonon coupling and is consistent with the presence of Franck-Condon blockade. Concluding, the observed features give strong hints for the tunneling induced excitation of phonons in a suspended part of a CNT QD. Considering the energy separation of the resonances and the suspended length, the vibrations are most probably of the longitudinal stretching mode.

7.2. Excitation of phonons in a parallel double quantum dot system

The second **Device C3** of this batch was prepared and measured under the same conditions as Device C2. The characterization at room temperature again yields a small band-gap CNT that is well coupled to the leads. The characteristic parameters of this device are listed in Tab. 7.2 including the CNT diameter d determined by atomic force microscopy. The stability diagram measurement at $T = 230$ mK is shown in Fig. 7.3 and exhibits a stable Coulomb blockade pattern with tilted diamonds. In contrast to the previous one, Device C3 shows some additional features that are not present in Fig. 7.2. First, there is a series of parallel lines of conductance running through the blockaded regions of the Coulomb diamonds. Considering the results of Ch. 6, it is tempting to interpret these features as inelastic cotunneling thresholds, but according to the theory of Ch. 2.2.2, the onset of inelastic cotunneling is supposed to occur as step in the measurement of $G(V_{\mathrm{sd}})$. The reason is that an additional channel available for conductance yields an increased linear $I(V_{\mathrm{sd}})$ behavior and thus, a step in differential conductance. Furthermore, the observed thresholds depend on V_{bg}, similar to the ICTs of Ch. 6, but as an important difference, here they are not symmetric with respect to zero-bias. Thus, the tilt cannot be explained by renormalization effects that are induced by different tunnel couplings of the involved QD

Table 7.2.: Characteristic properties of Device C3

G_{RT}	$0.49e^2/h$
R_{RT}	53 kΩ
d	3-4 nm
η	0.30
C_{s}	6.25 aF
C_{d}	6.23 aF
C_{bg}	5.31 aF
C_{Σ}	17.79 aF

orbitals to the leads, as it is introduced in Ch. 2.2.3. In combination with the fact that some of the observed lines are accompanied by NDC, their origin in cotunneling events can essentially be excluded, since they can not explain any of the observed features. Hence, these lines must have a different source and in the following it will be argued that they are based on a parallel double QD forming in a bundle of CNTs. In addition, it is suggested that the observed excited state lines are due to vibrational excitations of the side-dot of this system.

7.2.1. Parallel quantum dot system on an as-grown carbon nanotube

Since cotunneling induced resonances within the Coulomb blockaded regions of Fig. 7.3 are excluded, these features are interpreted as the superimposed Coulomb blockade pattern of a second, parallel QD that forms in a parallel CNT of a bundle. This feature has already been observed experimentally [48, 52, 53] and is introduced in Ch. 2.2.4. The QD that shows the clearly visible and narrow Coulomb diamonds is referred to as the main-dot, while the tilted lines are interpreted as the parallel diamond edges with negative slope of the side-dot. The respective edges with positive slope are not visible because this side-dot is coupled very asymmetrically to the electrodes. This is possible if it is

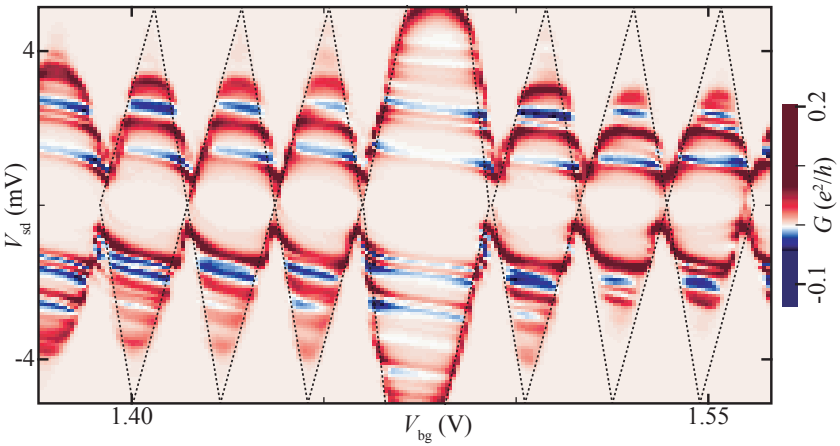

Figure 7.3.: Charge stability diagram of Device C3 measured at $T = 230$ mK. It exhibits stable Coulomb blockade with additional ridges of increased conductance within the diamonds and strong features of NDC. The ridges occur anti-symmetrically with respect to the zero-bias line.

located very close to one of the electrodes. If this picture is compared with the electron micrograph of Fig. 7.5 (b), it can be argued, that one of the suspended parts of the CNT holds the side-dot at the edge of the respective electrode. The resulting strong asymmetric capacitive coupling to source and drain would yield a very strong tilt of the diamonds, as it is introduced in Ch. 2.2. In the case of the stability diagram in Fig. 7.3, the tilt is even so strong, that the diamond edges with positive slope of the side-dot diamonds are not visible within the observed back-gate regime. Additionally, the much smaller size of the side-dot could explain its larger level spacing, according to Eq. (2.5), and its weaker coupling to the back-gate, and thus its much larger size. For comparison, the side-dot yields the relation of back-gate to source capacitance to $C_{\mathrm{bg}}/C_{\mathrm{s}} = -0.017$ which can be determined from the negative slope of the diamonds. This value is much smaller that the one for the main-dot that is given by $C_{\mathrm{bg}}/C_{\mathrm{s}} = -0.85$. Furthermore, additional electrons on the main-dot affect the side-dot such, that by the modified Coulomb repulsion, there is a discontinuity in the diamond features of the side-dot. That means, by proceeding to an adjacent Coulomb diamond, the position of the resonances of the side-dot experience a voltage offset[1] as it is sketched in Fig. 7.4 (b). The interpretation as the superimposed diamond patterns of two parallel QDs is the most probable way to explain the asymmetric features within the Coulomb blockaded region.

7.2.2. Coupling of phonons to tunneling electrons via the longitudinal stretching mode of the CNT

Considering the present system as a parallel double QD, it becomes apparent that the diamond pattern of the weakly coupled side-dot is combined with a series of excited state lines which occur roughly equidistant and are accompanied by NDC. Furthermore, the conductance at the charge degeneracy in the low bias regime is strongly suppressed. As introduced in Ch. 2.4, tunneling electrons are able to excite vibrational modes in suspended CNTs which gives rise to excited state lines at the diamond edges. In the present exotic case of a parallel QD system, only the diamond pattern of the side-dot shows vibrational excitations, which is basically sketched in Fig. 7.4 (a) on the example of a vibrating side-dot which results in the superimposed stability diagram of Fig. 7.4 (b). Here, also the effect of additional inter-QD coupling by a cross capacitance plays a role and is depicted: Adding an electron to the main-dot leads to a gating effect on the side-dot. Therefore, jumps are occurring in

[1] Compared to Ch. 3.5, these measurements were done on a modified setup where V_{bg} was applied from a non-floating voltage source. Therefore an additional isolation transformer was installed before the signal input of the lock-in amplifier in order to prevent ground-loops. Unfortunately, this transformer saturated at large currents, so that the discontinuities in the resonances of the side-dot could not be resolved.

the stability diagram of the side-dot at the positions of the charge degeneracy points of the main-dot. This gives also rise to the fact that in a small window of back-gate voltage only one slope of the secondary diamonds could be observed.

By applying this model to the experimental data of Fig. 7.3, the energy of the vibrational mode can be read directly from the distance of the excited state lines. This is done in the center of the Coulomb diamond of Fig. 7.5 (a) at $V_{\mathrm{bg}} = 1.477$ V, where a cut along V_{sd} yields several peak positions. Their separation is averaged to $\Delta E_{\mathrm{vib}} = 0.74 \pm 0.15$ meV. By comparing ΔE_{vib} to the energies of the different vibrational modes possible in a CNT, as depicted in Fig. 2.17, it becomes clear that the longitudinal stretching mode is the most probable alternative. Via Eq. (2.14), its energy can be correlated to the oscillator length of the CNT resulting in $L_0 = 150$ nm which is much shorter than the electrode gap of the structure. However, it roughly matches the suspended parts at the electrode edges, as it is shown in the electron micrograph of Fig. 7.5 (b). The lengths of these parts can be estimated to $L_{0,\mathrm{i}} \approx 112$ nm and $L_{0,\mathrm{ii}} \approx 176$ nm for the upper and the lower electrode in Fig. 7.5 (b), respectively. On the other hand, if the excited state lines were of electronic origin, their spacing would denote a QD of length $L_{\mathrm{QD}} \approx 2.2$ µm according to Eq. (2.5), which is not realistic considering the SEM image of the device. The vibrational excitations themselves are a signature of strong electron-phonon coupling, i.e. a large value of g, which means that phonons can easily be excited by tunneling

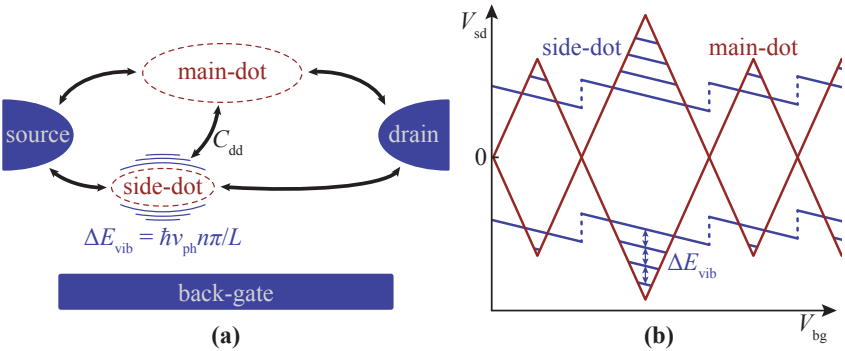

Figure 7.4.: (a) Transport model of a parallel double QD consisting of a main-dot (red) and a vibrating side-dot (blue). If the side-dot is located at the vibrating part of the CNT, tunneling electrons are able to excite the longitudinal stretching modes. **(b)** Sketched stability diagram of a double QD system with a vibrating side-dot. The excitation of vibrations leads to equidistant lines running parallel to the side-dot's Coulomb diamonds with a separation of ΔE_{vib}. For every electron that is added to the main-dot, the corresponding gating effect on the side-dot leads to a jump in its Coulomb diamond edges.

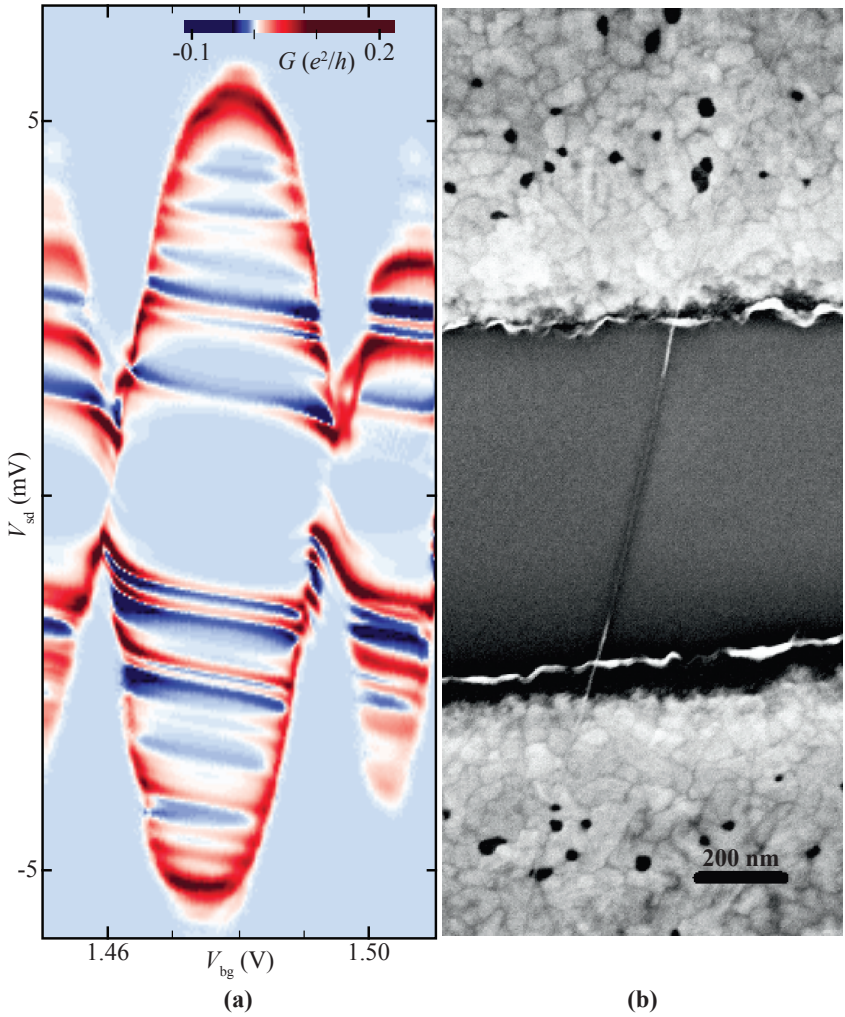

Figure 7.5.: (a) High-resolution stability diagram of the largest main-dot Coulomb diamond of Device C3 from Fig. 7.3. The side-dot shows a series of vibrational excited states. The averaged energy spacing $\Delta E_{\mathrm{vib}} = 0.74 \pm 0.15$ meV is compatible with the longitudinal stretching mode for a CNT of length $L = 150$ nm. **(b)** Electron micrograph of the corresponding CNT. At the edges of the upper and lower electrode of ≈ 60 nm thickness, the CNT is partially suspended over lengths of $L_{0,\mathrm{i}} \approx 112$ nm and $L_{0,\mathrm{ii}} \approx 176$ nm, respectively. These match quite well the value estimated from the energy spacing.

electrons. Another indication is given by the suppression of conductance in the low-bias regime. This Franck-Condon blockade is described in Ch. 2.4.3 to be a consequence of strong electron-phonon coupling.
Another feature observed on the two devices of Ch. 7.2 is the excited state lines being accompanied by lines of negative differential conductance. This has been observed in various experiments, for example in CNT peapod systems [54] or in fully suspended CNT QDs [5, 29]. In addition there have been several theoretical investigations of NDC in combination with Franck-Condon blockade [92] or electron-phonon coupling in double QDs [134]. It is also suggested that different locations of the QD and vibrating part lead to asymmetric Franck-Condon factors which finally results in NDC [83]. Still, the underlying reasons are not fully understood, but the only mechanism in a single QD with normal metal leads that has been shown to yield NDC is electron-phonon coupling.

8

Recessed bottom-gate structures for conventional carbon nanotube devices

Another possibility to fabricate clean CNT QDs with superconducting contacts is the so-called bottom-gate approach. This production scheme is based on a combination of conventional CNT devices and pre-fabricated trenches that are etched into the SiO_2 substrate and subsequently filled with metal. Since the latter is exposed to the CVD process, Re is the natural choice. Very recently, this concept with two bottom-gates has first been applied by M. Jung [51] and has lead to the formation of a highly tunable QD system with either single, double, or triple QDs that can be operated in different transport regimes. Additionally, the QDs can be fully emptied and sequentially charged. At the same time, this system has shown very clean transport properties, despite post-processing, since it allows the electrostatic definition of very small QDs where the characteristic energies of the QD are much larger than typical disorder potentials.
A similar device with a single bottom-gate structure is fabricated as sketched in Fig. 8.1. After defining several arrays of bottom-gates by EBL, they are opened by successive inductively coupled plasma (ICP) etching and HF wet-etching (see Appx. A for detailed parameters). While the former is an anisotropic process and yields a trench of $\sim$ 100 nm depth, the isotropic wet-etch step is used to create an undercut in the trenches in order to prevent flags on the bottom-gate during metal deposition. Subsequently, Re of 40 nm thickness is filled into these trenches by magnetron sputter deposition, followed by conventional CNT growth. Promising CNTs that preferably have grown perpendicular to and over

a specific bottom-gate are then localized and contacted by the standard process described in Ch. 3.1. Here, the contacts consist of a Ti/Au (5 nm / 70 nm) layer system that is prepared by e-beam evaporation (see Appx.A for detailed parameters). The device consists of a semiconducting CNT with a minimum resistance of $R_{\mathrm{RT}} = 50\ \mathrm{k}\Omega$ at room temperature.
Further investigation of the device is done at $T = 4.15$ K in a liquid He transport dewar. The result of a conductance measurement as a function of both, bottom-gate voltage V_{bog} and back-gate voltage V_{bg} is shown in Fig. 8.2. Unfortunately, there was a leak from the CNT to the bottom-gate for $|V_{\mathrm{bog}}| \gtrsim 0.8$ V which explains the presence of regions of strong noise in the measurement also in the low V_{bog} regime. However, the possibility of additional tuning by the global back-gate voltage gives rise to a QD system that can be operated in different regimes. First, the ridges of increased conductance in the top left and top right corner account for a Coulomb blockade pattern of a single QD. Second, the squared pattern in the bottom right corner is a sign of a serial double QD with small inter-QD coupling [135].
These are preliminary results and suggest the bottom-gate approach for the fabrication of clean CNT QD devices with the big advantage of not being limited in the choice of contact materials by the CVD process. Hence, this scheme exhibits a promising alternative to the as-grown fabrication process and would make the whole sample fabrication process much easier. However, it turned out

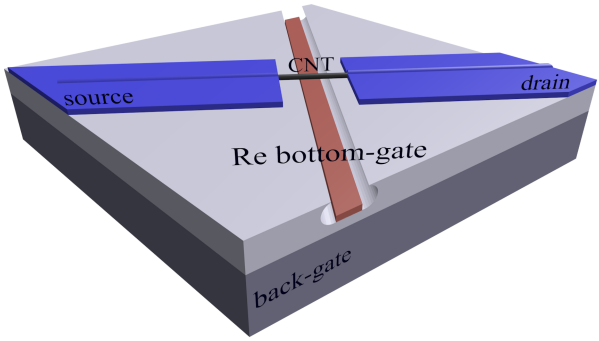

Figure 8.1.: Sketch of a conventional CNT device (see Fig. 3.1) with an additional recessed Re bottom-gate structure that is pre-fabricated by first, the definition of narrow lines by conventional EBL. Second, a directional ICP etching step opens a deep and narrow trench into the SiO_2 layer. However, sputter deposition is a process of very low directionality and thus will coat the PMMA/SiO_2 sidewalls to some extent, which will later cause electrical shorts from the bottom-gate to the CNT. Therefore, isotropic HF wet-etching is applied as third step in order to create an undercut in the SiO_2 layer. Finally, Re is sputter deposited into the trenches. The Si^{++} substrate is again used as global back-gate.

that the sputtered Re for the gate structures is not only deposited on the bottom of the trenches but also on its side walls, which finally leads to an electrical connection to the CNT. The additional wet-etching step is supposed to circumvent this problem by creating an undercut in the SiO_2 layer, thus Re should only be deposited on the bottom of the trench. The challenge here is to find the best combinations of PMMA thickness and the different parameters of the two etching processes, which is still an ongoing process. At the moment, the yield of working devices is limited by the continuing appearance of electrical shorts from the CNT to the bottom-gate which currently makes this method only work in combination with the preparation of large sample batches, comparable to those for the as-grown approach. Hence, some further optimization needs to be done, before this method could be applied to the fabrication of clean CNTs with superconducting contacts. The challenges in fabrication for this type of devices lie mainly in the design and preparation of the bottom-gates.

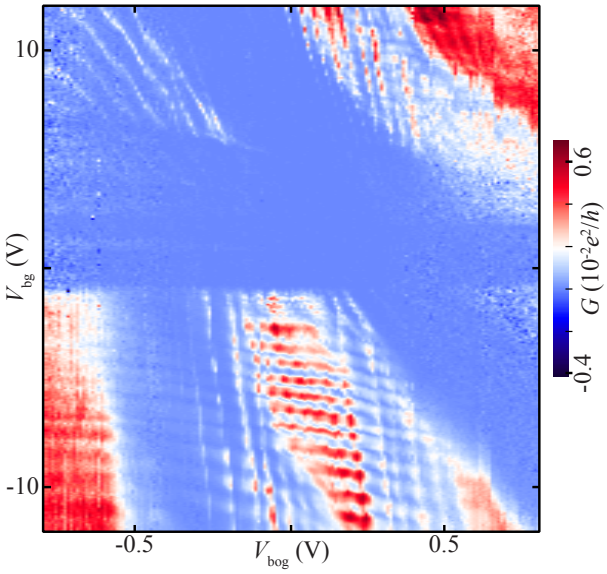

Figure 8.2.: Preliminary measurement at $T = 4.15$ K on the conventional CNT Device B1 with a single pre-fabricated bottom-gate. The conductance G as a function of both, back-gate voltage V_{bg} and bottom-gate voltage V_{bog} show indications of QD behavior. There are basically two regimes where either a single QD (in the top left and top right corners) or a serial double QD (in the bottom-right corner) is observed.

9 Summary and Outlook

In conclusion, the main goal of this thesis was to prepare as-grown carbon nanotube devices in combination with superconducting contacts in order to combine the typical clean electronic transport characteristics of such devices with the variety of features that are generally provided by Cooper pair injection onto a quantum dot. For example, it has already been possible to observe spin-orbit interaction in an as-grown carbon nanotube [6] on normal metal contacts that is usually masked by disorder. In combination with superconducting contacts that would allow for several new interesting effects, as they have been suggested by theory: the reversal of the Josephson current [23] for instance. Hence, the initial steps towards this goal were first, to select superconducting materials suitable for this special fabrication scheme and second, to check them for the superconducting proximity effect on CNT QDs. In the beginning, test with rhenium contacts on a conventionally prepared CNT device worked quite well, meaning it was possible to observe the superconducting gap in the density of states of the leads in transport measurements. The superconducting density of states exhibited a finite lifetime broadening, but its superconducting origin was proven by applying an external magnetic field to drive the electrodes into their normal state, suppressing the gap. Therefore, in the next step rhenium was applied as contact material for as-grown CNT devices, since it provides the important feature of surviving the CNT growth process unaltered in its superconducting properties, which is a major requirement. It was possible to measure devices of good cleanliness, indicated by nice and stable Coulomb blockade patterns in their stability diagrams. Unfortunately, in the end it was not possible to observe any superconducting proximity effect on as-grown CNT devices. Therefore, much effort was put into finding alternative superconducting materials and the improvement of the nanotube-superconductor interface.

The first concept was to add a thin contact layer of tungsten on top of the rhenium contacts where the idea was that tungsten is supposed to form much stronger bonds to CNTs. This results in a better electrical coupling [124] and should increase the chance for Cooper pair injection. Investigations on the contact resistance were done in order to optimize the thickness of the tungsten layer. Although devices of very low resistance could be realized, no superconducting proximity effect was observed. Therefore, additional investigations were done on rhenium/tungsten alloy systems that allow for tuning of the critical temperature by their composition. Finally, niobium and niobium nitride were applied as alternative contact materials. While the former turned out to form hydrides during chemical vapor deposition, the CNT growth method, and finally became insulating, the latter also made good contact to the CNT at room temperature. However, it turned out that using bare NbN contacts lead to the formation of large barriers at cryogenic temperatures and an exponentially increased resistance. Since this effect was supposed to be due to a mismatch of the work functions of NbN and CNT, respectively, a thin platinum contact layer of ~ 3 nm was added on top of the NbN contacts in order to adjust them. In the end this lead to devices showing very low-Ohmic contacts but unfortunately, no Cooper pair injection was observed. Hence, it is suggested that some effects at the interface cause a dephasing and a breaking of the Cooper pairs. Nevertheless, on the road to the actual goal of this thesis, some interesting results were observed:

First, an as-grown CNT in contact to a rhenium/tungsten double layer system exhibited a clean Coulomb blockade pattern. Both, inelastic cotunneling thresholds and sequential tunneling features were observed in the same stability diagram; features that usually require different coupling strengths to the leads. Remarkably, the inelastic cotunneling thresholds were tilted with respect to zero-bias. Typically, the onset of inelastic cotunneling is gate-independent, but due to different couplings of two involved degenerate dot levels to the leads, their energy separation can be tuned by the back-gate voltage. Furthermore, these couplings, and thus the energy separation of the states, could be changed by applying an external magnetic field, which resulted in a change of the sign of the tilts, accordingly.

Second, as-grown CNTs were contacted to a niobium nitride/platinum double layer system and showed clean and stable quantum dots, as well. On one of them, again tilted resonances within the Coulomb blockaded region were observed and initially considered as renormalized inelastic cotunneling thresholds. This first assumption was disproved by several features that could not be explained by means of cotunneling events: e.g. their occurrence as peaks in conductance, since ICTs usually appear as steps. Furthermore, the features

were again tilted, but in contrast to the above-mentioned measurements, the tilt was asymmetric with respect to zero-bias with the lines in the positive and negative bias regime being parallel. Therefore, the interpretation as cotunneling events was discarded and the picture of a parallel double quantum dot system was taken into account. This offered a stability diagram consisting of two superimposed Coulomb diamond patterns. In addition, one of them was assumed to be accompanied by a series of excited state lines. Due to their equidistance and combined appearance with negative differential conductance, they were interpreted as originating from tunneling induced vibrational excitations of a suspended part of the CNT. This is affirmed by the fact that the energy separation matches the excitation energy of the longitudinal stretching mode for the length of a suspended part of the CNT.

Finally it seems that the as-grown approach is quite delicate for the observation of superconducting proximity on a CNT. Since it worked on conventionally prepared samples with Re contacts, the lack of Cooper pair injection is most likely due to some interface effects, like contamination during chemical vapor deposition, where a leak in the reactor could lead to Re oxidation at high temperature, for example. Another possibility would be a dirty contact surface or a bad wetting of the CNT; in as-grown devices the contact area is smaller than in conventional devices, where the CNT is completely coated by contact metal during the deposition process.

Therefore, the bottom-gate approach was applied, that is supposed to yield very clean CNT quantum dots despite conventional post-processing steps [51]. It lead to some preliminary results on a serial double quantum dot, but it turned out as well, that the yield of this production scheme is quite low, i.e. about the same order compared to the as-grown fabrication process. Therefore, some further optimization needs to be done on this method, before it could be applied to the fabrication of clean CNTs with superconducting contacts.

As an outlook, an alternative way to fabricate clean CNT devices would be the so-called stamping technique. It allows a separate preparation of suspended CNTs and the actual device. Afterwards the two parts are brought together by stamping the CNT onto the contacts, a process which leaves the suspended part between the electrodes unaffected [136, 137]. On the other hand, this method results in relatively large contact resistances which are disadvantageous for Cooper pair injection. Thus, it has not been applied in the framework of this thesis, but nevertheless, the stamping technique has lead to interesting results on very clean CNT quantum dots with normal metal contacts [138].

A

Fabrication recipes

Wafer properties and cleaning procedure

- highly boron p-doped Si wafer with 400 nm of thermal oxide
- sonicate in acetone for 10 min
- rinse in IPA and blow-dry with N_2
- UV ozone treatment for 10 min

Electron beam lithography

- PMMA resist: *AR-P 671.09 950K*, Allresist, diluted in chlorobenzene
  - spin-coat with 4000 rpm for 40 s with ramp of 4 s
  - bake on hot-plate at 180 °C for 10 min
- exposure parameters for electron microscope *Zeiss Supra 40*:
  - 20 kV acceleration voltage
  - 16.9 mm working distance
  - 2000 µm large writefield
  - 120 µm large aperture
  - 200 µm small writefield
  - 10 µm small aperture
- develop in 1 part methyl isobutyl ketone and 3 parts IPA for 90 s
- rinse in IPA and blow-dry with N_2

Magnetron sputter evaporation in the *ESCA3*

- $5 \cdot 10^{-8}$ mbar base pressure
- 40 sccm Ar flow
- 10^{-2} mbar sputter pressure
- sputter parameters NbN
  - 4 sccm N_2 flow
  - 100 W pulsed DC power
  - 250 kHz pulse frequency
  - 1600 ns pulse width
  - 1.0 Å/s deposition rate
- sputter parameters Pt
  - 50 W DC power
  - 0.5 Å/s deposition rate
- sputter parameters Re
  - 50 W DC power
  - 1.3 Å/s deposition rate
- lift-off in acetone plus sonicate for 1 s
- rinse in IPA and blow-dry with N_2

Magnetron sputter evaporation in the *AJA*

- $5 \cdot 10^{-9}$ mTorr base pressure
- 40 sccm Ar flow
- 4 mTorr sputter pressure
- sputter parameters Re
  - 50 W DC power
  - 1.1 Å/s deposition rate
- sputter parameters W
  - 50 W DC power
  - 0.5 Å/s deposition rate
- lift-off in acetone plus sonicate for 1 s
- rinse in IPA and blow-dry with N_2

Buffered HF-etching

- 2 % buffered hydrofluoric acid
- etch 250 nm of SiO_2 at a rate of 42 nm/min
- rinse in IPA and blow-dry with N_2

Catalyst

- prepare stock solutions
  - dissolve 30 mg of Al_2O_3 nanoparticles (4 nm) in 20 ml of IPA
  - dissolve 93 mg of $Fe(NO_3)_3$-$9H_2O$ in 20 ml of IPA
  - dissolve 27 mg of MoO_2Cl_2 in 20 ml of IPA
- sonicate each stock solution for 12 h
- mix equal parts of the stock solutions
- sonicate the final catalyst for 12 h

Chemical vapor deposition

- sonicate catalyst for 3 h
- catalyst deposition for conventional CNT devices
  - dilute 1 ml of catalyst in 25 ml of IPA
  - spin-coat diluted catalyst with 4000 rpm for 10 s
- catalyst deposition for as-grown CNT devices
  - define catalyst spots by standard electron beam lithography
  - spin-coat undiluted catalyst with 4000 rpm for 40 s
  - repeat spin-coating 5 times
  - flush sample carefully with acetone
    This is crucial in order to remove the unwanted catalyst on top of the PMMA; during lift-off the acetone has to be as clean as possible to prevent the sample from being covered with catalyst particles.
  - lift-off in acetone
- heat-up in Ar (104 l/h) / H_2 (8 l/h) atmosphere to $T = 950$ °C
- 15 min CNT growth in CH_4 (44 l/h) / H_2 (8 l/h) atmosphere
- cool-down in Ar (104 l/h) / H_2 (8 l/h) atmosphere to $T < 200$ °C

Inductively coupled plasma etching

- $5{\cdot}10^{-6}$ Pa base pressure
- 30 sccm CF_4 flow
- 0.4 Pa CF_4 pressure
- 50 W ICP power
- 45 W HF power
- 1 nm/s etching rate of SiO_2

Hydrogen plasma cleaning

- 20 sccm H_2 flow
- 1.2 mbar H_2 pressure
- 110 °C reactor temperature
- 25 W RF power
- 40 nm/min etching rate of PMMA resist

Electron beam evaporation in the *Balzers PLS 500*

- $2 \cdot 10^{-7}$ mbar base pressure
- -5 °C sample temperature
- 10 kV gun voltage
- gun parameters Ti
  - 45 mA gun current
  - 0.8 Å/s deposition rate
- gun parameters Au
  - 300 mA gun current
  - 1.4 Å/s deposition rate
- lift-off in acetone
- rinse in IPA and blow-dry with N_2

Bibliography

[1] S. Iijima, Nature **354**, 56 (1991).

[2] C. Schönenberger, Semiconductor Science and Technology **21**, S1 (2006).

[3] T. S. Jespersen, K. Grove-Rasmussen, J. Paaske, K. Muraki, T. Fujisawa, J. Nygård, and K. Flensberg, Nat Phys **7**, 348 (2011).

[4] J. Cao, Q. Wang, and H. Dai, Nat Mater **4**, 745 (2005).

[5] S. Sapmaz, P. Jarillo-Herrero, Y. M. Blanter, C. Dekker, and H. S. J. van der Zant, Phys. Rev. Lett. **96**, 026801 (2006).

[6] F. Kuemmeth, S. Ilani, D. C. Ralph, and P. L. McEuen, Nature **452**, 448 (2008).

[7] G. A. Steele, G. Gotz, and L. P. Kouwenhoven, Nat Nano **4**, 363 (2009).

[8] G. A. Steele, A. K. Hüttel, B. Witkamp, M. Poot, H. B. Meerwaldt, L. P. Kouwenhoven, and H. S. J. van der Zant, Science **325**, 1103 (2009).

[9] J.-D. Pillet, C. H. L. Quay, P. Morfin, C. Bena, A. L. Yeyati, and P. Joyez, Nat Phys **6**, 965 (2010).

[10] A. K. Hüttel, G. A. Steele, B. Witkamp, M. Poot, L. P. Kouwenhoven, and H. S. J. van der Zant, Nano Lett. **9**, 2547 (2009).

[11] S. Suzuki, K. Kanzaki, Y. Homma, and S. ya Fukuba, Jpn. J. Appl. Phys. **43**, L1118 (2004).

[12] P. Jarillo-Herrero, J. A. van Dam, and L. P. Kouwenhoven, Nature **439**, 953 (2006).

[13] M. R. Buitelaar, W. Belzig, T. Nussbaumer, B. Babic, C. Bruder, and C. Schönenberger, Phys. Rev. Lett. **91**, 057005 (2003).

[14] A. Eichler, M. Weiss, S. Oberholzer, C. Schönenberger, A. Levy Yeyati, J. C. Cuevas, and A. Martín-Rodero, Phys. Rev. Lett. **99**, 126602 (2007).

[15] A. Martín-Rodero and A. Levy Yeyati, Advances in Physics **60**, 899 (2011).

[16] K. Grove-Rasmussen, H. I. Jørgensen, B. M. Andersen, J. Paaske, T. S. Jespersen, J. Nygård, K. Flensberg, and P. E. Lindelof, Phys. Rev. B **79**, 134518 (2009).

[17] J. Schindele, A. Baumgartner, and C. Schönenberger, Phys. Rev. Lett. **109**, 157002 (2012).

[18] L. Hofstetter, S. Csonka, J. Nygård, and C. Schönenberger, Nature **461**, 960 (2009).

[19] L. G. Herrmann, F. Portier, P. Roche, A. L. Yeyati, T. Kontos, and C. Strunk, Phys. Rev. Lett. **104**, 026801 (2010).

[20] S. De Franceschi, L. Kouwenhoven, C. Schonenberger, and W. Wernsdorfer, Nat Nano **5**, 703 (2010).

[21] J. Klinovaja, S. Gangadharaiah, and D. Loss, Phys. Rev. Lett. **108**, 196804 (2012).

[22] G. Sonne, M. E. Peña-Aza, L. Y. Gorelik, R. I. Shekhter, and M. Jonson, Phys. Rev. Lett. **104**, 226802 (2010).

[23] J. S. Lim, R. López, and R. Aguado, Phys. Rev. Lett. **107**, 196801 (2011).

[24] J.-P. Cleuziou, W. Wernsdorfer, V. Bouchiat, T. Ondarcuhu, and M. Monthioux, Nat Nano **1**, 53 (2006).

[25] A. Eichler, R. Deblock, M. Weiss, C. Karrasch, V. Meden, C. Schönenberger, and H. Bouchiat, Phys. Rev. B **79**, 161407 (2009).

[26] R. Maurand, T. Meng, E. Bonet, S. Florens, L. Marty, and W. Wernsdorfer, Phys. Rev. X **2**, 011009 (2012).

[27] A. K. Hüttel, M. Poot, B. Witkamp, and H. S. J. van der Zant, New Journal of Physics **10**, 095003 (2008).

[28] A. K. Hüttel, B. Witkamp, M. Leijnse, M. R. Wegewijs, and H. S. J. van der Zant, Phys. Rev. Lett. **102**, 225501 (2009).

[29] R. Leturcq, C. Stampfer, K. Inderbitzin, L. Durrer, C. Hierold, E. Mariani, M. G. Schultz, F. von Oppen, and K. Ensslin, Nat Phys **5**, 327 (2009).

[30] J.-C. Charlier, X. Blase, and S. Roche, Rev. Mod. Phys. **79**, 677 (2007).

[31] C. Schönenberger, *Bandstructure of Graphene and Carbon Nanotubes* (Solid State Physics Lecture, 2000).

[32] J. Alfonsi, *Brillouin Zone of a Single-Walled Carbon Nanotube* (Wolfram Demonstrations Project, 2008).

[33] G. G. Samsonidze, R. Saito, A. Jorio, M. Pimenta, A. Souza Filho, A. Grüneis, G. Dresselhaus, and M. Dresselhaus, Journal of Nanoscience and Nanotechnology **3**, 431 (2003).

[34] J. Alfonsi, *Small Crystal Models for the Electronic Properties of Carbon Nanotubes*, Ph.D. thesis, Università Degli Studi di Padova (2008).

[35] S. Ilani and P. L. McEuen, *Annual Review of Condensed Matter Physics*, Annu. Rev. Condens. Matter Phys. **1**, 1 (2010).

[36] L. Yang and J. Han, Phys. Rev. Lett. **85**, 154 (2000).

[37] C. L. Kane and E. J. Mele, Phys. Rev. Lett. **78**, 1932 (1997).

[38] M. Ouyang, J.-L. Huang, C. L. Cheung, and C. M. Lieber, Science **292**, 702 (2001).

[39] L. P. Kouwenhoven, C. M. Marcus, P. L. McEuen, S. Tarucha, R. M. Westervelt, and N. Wingreen, *Proceedings of the NATO Advanced Study Institute on Mesoscopic Electron Transport*, edited by L. L. Sohn, L. P. Kouwenhoven, and G. Schön (Kluwer Academic Publishers, 1997) pp. 105–214.

[40] L. P. Kouwenhoven, D. G. Austing, and S. Tarucha, Reports on Progress in Physics **64**, 701 (2001).

[41] T. Heinzel, *Mesoscopic Electronics in Solid State Nanostructures* (Wiley-VCH, Weinheim, 2003).

[42] A. Eichler, *Quantum Dot Josephson Junctions in the Kondo Regime*, Ph.D. thesis, Universität Basel (2010).

[43] S. Heinze, J. Tersoff, R. Martel, V. Derycke, J. Appenzeller, and P. Avouris, Phys. Rev. Lett. **89**, 106801 (2002).

[44] S. De Franceschi, S. Sasaki, J. M. Elzerman, W. G. van der Wiel, S. Tarucha, and L. P. Kouwenhoven, Phys. Rev. Lett. **86**, 878 (2001).

[45] J. V. Holm, H. I. Jørgensen, K. Grove-Rasmussen, J. Paaske, K. Flensberg, and P. E. Lindelof, Phys. Rev. B **77**, 161406 (2008).

[46] K. Grove-Rasmussen, S. Grap, J. Paaske, K. Flensberg, S. Andergassen, V. Meden, H. I. Jørgensen, K. Muraki, and T. Fujisawa, Phys. Rev. Lett. **108**, 176802 (2012).

[47] R. Schleser, T. Ihn, E. Ruh, K. Ensslin, M. Tews, D. Pfannkuche, D. C. Driscoll, and A. C. Gossard, Phys. Rev. Lett. **94**, 206805 (2005).

[48] K. Goß, S. Smerat, M. Leijnse, M. R. Wegewijs, C. M. Schneider, and C. Meyer, Phys. Rev. B **83**, 201403 (2011).

[49] M. R. Gräber, W. A. Coish, C. Hoffmann, M. Weiss, J. Furer, S. Oberholzer, D. Loss, and C. Schönenberger, Phys. Rev. B **74**, 075427 (2006).

[50] M. R. Gräber, M. Weiss, S. Oberholzer, and C. Schönenberger, Semiconductor Science and Technology **21**, S64 (2006).

[51] M. Jung, J. Schindele, S. Nau, M. Weiss, A. Baumgartner, and C. Schönenberger, Nano Lett. **13**, 4522 (2013).

[52] K. Goß, *Interactions Between Parallel Carbon Nanotubes Quantum Dots* (Forschungszentrum Jülich GmbH, 2011).

[53] K. Goß, M. Leijnse, S. Smerat, M. R. Wegewijs, C. M. Schneider, and C. Meyer, Phys. Rev. B **87**, 035424 (2013).

[54] A. Eliasen, J. Paaske, K. Flensberg, S. Smerat, M. Leijnse, M. R. Wegewijs, H. I. Jørgensen, M. Monthioux, and J. Nygård, Phys. Rev. B **81**, 155431 (2010).

[55] M. Tinkham, *Introduction to Superconductivity* (Dover Publications, Inc., Mineola, New York, 2004).

[56] J. Bardeen, L. N. Cooper, and J. R. Schrieffer, Phys. Rev. **108**, 1175 (1957).

[57] L. N. Cooper, Phys. Rev. **104**, 1189 (1956).

[58] W. Belzig, A. Brataas, Y. V. Nazarov, and G. E. W. Bauer, Phys. Rev. B **62**, 9726 (2000).

[59] W. Meissner and R. Ochsenfeld, Naturwissenschaften **21**, 787 (1933).

[60] T. Dirks, Y.-F. Chen, N. O. Birge, and N. Mason, Appl. Phys. Lett. **95**, 192103 (2009).

[61] R. C. Dynes, V. Narayanamurti, and J. P. Garno, Phys. Rev. Lett. **41**, 1509 (1978).

[62] S. B. Kaplan, C. C. Chi, D. N. Langenberg, J. J. Chang, S. Jafarey, and D. J. Scalapino, Phys. Rev. B **14**, 4854 (1976).

[63] J. P. Pekola, V. F. Maisi, S. Kafanov, N. Chekurov, A. Kemppinen, Y. A. Pashkin, O.-P. Saira, M. Möttönen, and J. S. Tsai, Phys. Rev. Lett. **105**, 026803 (2010).

[64] H. Park, J. Park, A. K. L. Lim, E. H. Anderson, A. P. Alivisatos, and P. L. McEuen, Nature **407**, 57 (2000).

[65] A. K. Hüttel, H. B. Meerwaldt, G. A. Steele, M. Poot, B. Witkamp, L. P. Kouwenhoven, and H. S. J. van der Zant, phys. stat. sol. (b) **247**, 2974 (2010).

[66] A. Eichler, M. del Alamo Ruiz, J. A. Plaza, and A. Bachtold, Phys. Rev. Lett. **109**, 025503 (2012).

[67] V. Sazonova, Y. Yaish, H. Ustunel, D. Roundy, T. A. Arias, and P. L. McEuen, Nature **431**, 284 (2004).

[68] N. Anderson, A. Hartschuh, and L. Novotny, Nano Lett. **7**, 577 (2007).

[69] B. J. LeRoy, S. G. Lemay, J. Kong, and C. Dekker, Nature **432**, 371 (2004).

[70] S. Sapmaz, Y. M. Blanter, L. Gurevich, and H. S. J. van der Zant, Phys. Rev. B **67**, 235414 (2003).

[71] M. S. Dresselhaus and P. C. Eklund, *Advances in Physics*, Advances in Physics **49**, 705 (2000).

[72] L. Landau and E. Lifshitz, *Theory of Elasticity* (Pergamon, Oxford, 1986).

[73] J. Franck and E. G. Dymond, Trans. Faraday Soc. **21**, 536 (1926).

[74] E. Condon, Phys. Rev. **28**, 1182 (1926).

[75] H. Bruus and K. Flensberg, *Many-Body Quantum Theory in Condensed Matter Physics* (Oxford University Press Inc., New York, 2004).

[76] H. Haken and H. Wolf, *Molekülphysik und Quantenchemie* (Springer-Verlag, Berlin Heidelberg New York, 2006).

[77] J. Koch and F. von Oppen, Phys. Rev. Lett. **94**, 206804 (2005).

[78] J. Koch, F. von Oppen, and A. V. Andreev, Phys. Rev. B **74**, 205438 (2006).

[79] E. M. Weig, R. H. Blick, T. Brandes, J. Kirschbaum, W. Wegscheider, M. Bichler, and J. P. Kotthaus, Phys. Rev. Lett. **92**, 046804 (2004).

[80] E. Mariani and F. von Oppen, Phys. Rev. B **80**, 155411 (2009).

[81] J. Park, A. N. Pasupathy, J. I. Goldsmith, C. Chang, Y. Yaish, J. R. Petta, M. Rinkoski, J. P. Sethna, H. D. Abruna, P. L. McEuen, and D. C. Ralph, Nature **417**, 722 (2002).

[82] J. Koch, M. E. Raikh, and F. von Oppen, Phys. Rev. Lett. **95**, 056801 (2005).

[83] F. Cavaliere, E. Mariani, R. Leturcq, C. Stampfer, and M. Sassetti, Phys. Rev. B **81**, 201303 (2010).

[84] S. Andergassen, V. Meden, H. Schoeller, J. Splettstoesser, and M. R. Wegewijs, Nanotechnology **21**, 272001 (2010).

[85] M. G. Schultz, Phys. Rev. B **82**, 195322 (2010).

[86] A. Zazunov, D. Feinberg, and T. Martin, Phys. Rev. B **73**, 115405 (2006).

[87] X. Y. Shen, B. Dong, X. L. Lei, and N. J. M. Horing, Phys. Rev. B **76**, 115308 (2007).

[88] A. Yar, A. Donarini, S. Koller, and M. Grifoni, Phys. Rev. B **84**, 115432 (2011).

[89] F. Cavaliere, A. Braggio, J. T. Stockburger, M. Sassetti, and B. Kramer, Phys. Rev. Lett. **93**, 036803 (2004).

[90] R. Härtle and M. Thoss, Phys. Rev. B **83**, 115414 (2011).

[91] A. Donarini, A. Yar, and M. Grifoni, New Journal of Physics **14**, 023045 (2012).

[92] E. Perfetto and G. Stefanucci, arXiv: 1307.7527v1 (2013).

[93] M. Ciorga, M. Pioro-Ladriere, P. Zawadzki, P. Hawrylak, and A. S. Sachrajda, Appl. Phys. Lett. **80**, 2177 (2002).

[94] J. Svensson and E. E. B. Campbell, J. Appl. Phys. **110**, 111101 (2011).

[95] W. Schottky, Physikalische Zeitschrift **41**, 570 (1940).

[96] N. F. Mott, Proc. Cambridge Philos. Soc. **34**, 568 (1938).

[97] S. M. Sze, *Physics of Semiconductor Devices* (John Wiley & Sons, New York, 1969).

[98] A. Javey, J. Guo, Q. Wang, M. Lundstrom, and H. Dai, Nature **424**, 654 (2003).

[99] X. Cui, M. Freitag, R. Martel, L. Brus, and P. Avouris, Nano Lett. **3**, 783 (2003).

[100] Y. Nosho, Y. Ohno, S. Kishimoto, and T. Mizutani, Nanotechnology **17**, 3412 (2006).

[101] Z. Chen, J. Appenzeller, J. Knoch, Y.-m. Lin, and P. Avouris, Nano Lett. **5**, 1497 (2005).

[102] F. Léonard and J. Tersoff, Phys. Rev. Lett. **84**, 4693 (2000).

[103] F. Léonard and A. A. Talin, Phys. Rev. Lett. **97**, 026804 (2006).

[104] V. Vitale, A. Curioni, and W. Andreoni, Journal of the American Chemical Society **130**, 5848 (2008).

[105] S. Dag, O. Gulseren, S. Ciraci, and T. Yildirim, Appl. Phys. Lett. **83**, 3180 (2003).

[106] Y. Matsuda, W.-Q. Deng, and W. A. Goddard, *The Journal of Physical Chemistry C*, J. Phys. Chem. C **111**, 11113 (2007).

[107] Y. Zhang, N. W. Franklin, R. J. Chen, and H. Dai, Chemical Physics Letters **331**, 35 (2000).

[108] J. Furer, *Growth of Single-Wall Carbon Nanotubes by Chemical Vapor Deposition for Electrical Devices*, Ph.D. thesis, Universität Basel (2006).

[109] H. Dai, *Accounts of Chemical Research*, Acc. Chem. Res. **35**, 1035 (2002).

[110] J. A. Thornton, Journal of Vacuum Science and Technology **15**, 171 (1978).

[111] Z. Wang, Journal of Applied Physics **79**, 7837 (1996).

[112] S. Thakoor, J. L. Lamb, A. P. Thakoor, and S. K. Khanna, Journal of Applied Physics **58**, 4643 (1985).

[113] "`www.superconductors.org`," (2007).

[114] F. Ullmann, *Ullmann's encyclopedia of industrial chemistry* (Wiley-VCH, Weinheim, 2002).

[115] S. Oh, D. A. Hite, K. Cicak, K. D. Osborn, R. W. Simmonds, R. McDermott, K. B. Cooper, M. Steffen, J. M. Martinis, and D. P. Pappas, Thin Solid Films **496**, 389 (2006).

[116] J. K. Hulm and B. B. Goodman, Phys. Rev. **106**, 659 (1957).

[117] J. G. Daunt and T. S. Smith, Phys. Rev. **88**, 309 (1952).

[118] I. D. Baikie, U. Petermann, A. Speakman, B. Lägel, K. M. Dirscherl, and P. J. Estrup, Journal of Applied Physics **88**, 4371 (2000).

[119] S. I. Ochiai, M. L. A. MacVicar, and R. M. Rose, Solid State Communications **8**, 1031 (1970).

[120] S. I. Ochiai, M. L. A. MacVicar, and R. M. Rose, Phys. Rev. B **4**, 2988 (1971).

[121] C. J. H. Keijzers, *Josephson effects in carbon nanotube mechanical resonators and graphene*, Ph.D. thesis, Technische Universiteit Delft (2012).

[122] D. R. Schmid, C. S. P L Stiller, and A. K. Hüttel, Physical Review B **86**, (2012).

[123] B. H. Schneider, S. Etaki, H. S. J. van der Zant, and G. A. Steele, Sci. Rep. **2**, (2012).

[124] M.-S. Wang, D. Golberg, and Y. Bando, Adv. Mater. **22**, 5350 (2010).

[125] D. S. Easton, C. C. Koch, D. M. Kroeger, and J. W. Cable, *Philosophical Magazine*, Philosophical Magazine **30**, 1117 (1974).

[126] H. Raffy and R. B. Laibowitz, Phys. Rev. B **30**, 5541 (1984).

[127] K. Komatsu, C. Li, S. Autier-Laurent, H. Bouchiat, and S. Guéron, Phys. Rev. B **86**, 115412 (2012).

[128] J. R. Gavaler, D. W. Deis, J. K. Hulm, and C. K. Jones, Applied Physics Letters **15**, 329 (1969).

[129] A. Shoji, S. Kiryu, and S. Kohjiro, Appl. Phys. Lett. **60**, 1624 (1992).

[130] A. Shoji, Applied Physics Letters **46**, 1098 (1985).

[131] Y.-L. Zhong, T. Akazaki, K. Kanzaki, Y. Kobayashi, and H. Takayanagi, Science and Technology of Advanced Materials **7**, S78 (2006).

[132] G. Giovannetti, P. A. Khomyakov, G. Brocks, V. M. Karpan, J. van den Brink, and P. J. Kelly, Phys. Rev. Lett. **101**, 026803 (2008).

[133] C. Tonnoir, A. Kimouche, J. Coraux, L. Magaud, B. Delsol, B. Gilles, and C. Chapelier, Phys. Rev. Lett. **111**, 246805 (2013).

[134] S. Walter, B. Trauzettel, and T. L. Schmidt, Phys. Rev. B **88**, 195425 (2013).

[135] W. G. van der Wiel, S. De Franceschi, J. M. Elzerman, T. Fujisawa, S. Tarucha, and L. P. Kouwenhoven, Rev. Mod. Phys. **75**, 1 (2002).

[136] C. C. Wu, C. H. Liu, and Z. Zhong, Nano Letters **10**, 1032 (2010).

[137] F. Pei, E. A. Laird, G. A. Steele, and L. P. Kouwenhoven, Nat Nano **7**, 630–634 (2012).

[138] J. Waissman, M. Honig, S. Pecker, A. Benyamini, A. Hamo, and S. Ilani, Nat Nano **8**, 569 (2013).

Publication List

Articles

- *Ultraclean single, double and triple carbon nanotube quantum dots with recessed Re bottom gates*
  M. Jung, J. Schindele, S. Nau, M. Weiss, A. Baumgartner, and Ch. Schönenberger, Nano Lett. **13**, 4522 (2013)

- *Tuning the properties of magnetic thin films by interaction with periodic nanostructures*
  U. Wiedwald, F. Haering, S. Nau, C. Schulze, H. Schletter, D. Makarov, A. Plettl, K. Kuepper, M. Albrecht, J. Boneberg, and P. Ziemann, Beilstein J. Nanotechnol. **3**, 831 (2012)

Poster Contributions

- *Combining ultra-clean carbon nanotube quantum dots with superconducting contacts*
  S. Nau, M. Weiss, and Ch. Schönenberger
  Frontiers in Quantum Engineered Devices in Obergurgl, Austria, 08/2013

- *Ultra-clean carbon in one and two dimensions*
  F. Freitag, S. Nau, M. Weiss, R. Maurand and Ch. Schönenberger
  Swiss NanoConvention in Basel, Switzerland, 05/2013

- *Electronic transport in ultra-clean carbon nanotube quantum dots*
  S. Nau, M. Weiss, and Ch. Schönenberger
  SPS annual meeting in Zürich, Switzerland, 06/2012

- *Cooper pair splitting and electron transport in superconductor hybrid nanostructures*
  A. Baumgartner, S. d'Hollosy, G. Fabian, S. Nau, J. Samm, J. Schindele, M. Weiss, and Ch. Schönenberger
  NCCR QSIT General Meeting in Arosa, Switzerland, 02/2012

- *Electronic transport in ultra-clean carbon nanotube quantum dots*
  S. Nau, M. Weiss, and Ch. Schönenberger
  NCCR QSIT first Site Visit of the Review Panel in Zürich, 12/2011

- *Electronic transport in ultra-clean carbon nanotube quantum dots*
  S. Nau, M. Weiss, and Ch. Schönenberger
  ESF Q-Spice Workshop on Spintronics in Porto Ottiolu, Italy, 10/2011

- *Quantum transport in carbon nanotube and nanowire hybrid devices*
  H. Aurich, A. Baumgartner, L. Hofstetter, S. d'Hollosy, S. Nau, J. Samm, J. Schindele, Ch. Schönenberger, and M. Weiss
  NCCR QSIT General Meeting in Arosa, 01/2011

Oral Presentation

- *Electronic transport in ultra-clean carbon nanotube quantum dots*
  NCCR QSIT Junior Meeting in Passugg, Switzerland, 07/2012

Acknowledgments

At this point I would like to thank everybody who supported me and helped this work to succeed. It was a great experience to work at the Department of Physics where I had the possibility to learn so many things in a variety of fields in a friendly and constructive atmosphere.
First of all, I am very grateful to Christian Schönenberger for giving me the opportunity to do research in his group. He guided me through my project and, at the same time, allowed me great latitude to pursue my own ideas.
My very special thanks goes to Markus Weiss for his excellent mentoring, motivation and all his effort he invested in many discussions and explanations through my whole time in the Nanoelectronics Group.
I would like to thank Gary Steele for co-refereeing my thesis and joining the defense committee.
I am indebted to Laurent Marot who introduced me to the technique of magnetron sputtering at the *ESCA3* and assisted me in many technical and experimental issues.
Furthermore, I would like to thank Minkyung Jung for his cooperation and support in the work on the bottom-gate devices.
I would like to thank all the former and present members of the group: the LT postdocs Jelena Trbovic, Andreas Baumgartner, Romain Maurand, Péter Makk and also my colleagues and office mates Lukas Hofstetter, Hagen Aurich, Frank Freitag, Jens Schindele, Matthias Bräuninger, Julia Samm, Samuel d'Hollosy, Peter Rickhaus, Gábor Fábián, Jörg Gramich, Samuel Hess for many fruitful discussions and the nice atmosphere in our group. Of course, this also includes the people of the RT and RF projects: Michel Calame, Claire Barret, Wangyang Fu, Jon Agustsson, Oren Knopfmacher, Alexey Tarasov, Jan Brunner, Toni Fröhlich, Cornelia Nef, Mathias Wipf, Ralph Stoop, Thomas Hasler, Anton Vladyka, Vishal Ranjan, Clevin Handschin, Kishan Thodkar, Gulbostan Abulizi. I specially enjoyed the numerous group and ski excursions to various very nice places throughout Switzerland.
Many thanks to the people of the technical service teams, the mechanical workshop and the electronic workshop, in particular Dominik Sifrig, Patrick Stöcklin, Bernd Heimann, Michael Steinacher and Werner Erni for their constant helpfulness.
I would like to thank Barbara Kammermann and Astrid Kalt for their helpful support in all the administrative matters.
Finally, I am very thankful to my family for their continuous support throughout my whole education.